Three-Magnet Arrays for Unilateral Magnetic Resonance

by

Juan Carlos García Naranjo

Master in Biomedical Engineering,
Universidad Central de las Villas, Cuba

A Dissertation Submitted in Partial Fulfillment
of the Requirements for the Degree of

Doctor of Philosophy

in the Graduate Academic Unit of Electrical and Computer Engineering

Supervisors: Bruce Balcom, Ph.D, Physics
Bruce Colpitts, Ph.D, Electrical and Computer Engineering

Examining Board: Benedict Newling, Ph.D, Physics, Chair
Richard Tervo, Ph.D, Electrical and Computer Engineering
Brent Petersen, Ph.D, Electrical and Computer Engineering

External Examiner: Siegfried Stapf, Ph.D, Ilmenau University of Thecnology.

This dissertation is accepted by the
Dean of Graduate Studies

THE UNIVERSITY OF NEW BRUNSWICK

November, 2011

Library and Archives Canada

Published Heritage Branch

395 Wellington Street
Ottawa ON K1A 0N4
Canada

Bibliothèque et Archives Canada

Direction du Patrimoine de l'édition

395, rue Wellington
Ottawa ON K1A 0N4
Canada

Your file Votre référence
ISBN: 978-0-494-95404-1

Our file Notre référence
ISBN: 978-0-494-95404-1

Dedication

To my parents.

Abstract

Unilateral Magnetic Resonance (UMR) has become, in different research areas, a powerful tool to interrogate samples of arbitrary size. The three-magnet array developed by the MRI Centre of the University of New Brunswick has features that make it a simple and robust approach for UMR. This thesis introduces a group of solutions to broaden the range of application of this design. Practical applications for non-destructive testing and reservoir core plug characterization are presented. We have shown that it is also possible to monitor the curing process of an epoxy/polyamidoamine system by employing a three-magnet array. A new version of the three-magnet array which features extended constant magnetic field gradients is also introduced. Constant gradients of more than 3 cm extent can be achieved in a very simple, compact and safe design. The application of the three-magnet array in combination with a solenoid as the RF probe for analysis of long core plugs has been presented. Core plugs of different diameter can be analyzed by simply changing the diameter of the RF probe employed for the measurement. Results of an initial survey of selective excitation in UMR are presented. The low SNR and inhomogeneities in the selective spot reduce the effectiveness of selective excitation for UMR.

Acknowledgements

Four years working at the UNB MRI lab has been one of the greatest experiences of my life. If I have had any success it is the result of small contributions from a lot of people. For all of them, these lines are a token of my gratitude. Any omission is my fault and I apologize.

First of all I want to thank this beautiful country and its friendly people. Every day here was for me a confirmation that Canada was the right place to come. I want to thank my supervisor Dr. Bruce J. Balcom for his support and for being an excellent example as a researcher, head of a team and human being. This period working with him has been a continued learning process that I hope it will not stop with the end of this thesis. I also want to thank my supervisor Dr. Bruce G. Colpitts for his advice and quick response to my requests, and for giving me the independence that I needed. Special thanks for my supervisor on the Cuban side Dr. Manuel A. Lores Guevara for making everything easier for me and for supporting my family when I was away.

Four years away from home is a lot of time. Fortunately, I found here a group of very special people that have became my Canadian family. One life will not be enough to thank these amazing people: Joan Green, Garry Guild, Cristiane Paponnet Cantat, Yanepys Morales Castillo, Eduardo Castillo Guerra and Eduardo Castillo Morales.

I would also like to thank the great people of the UNB MRI Centre for giving me support and advice during this period: Ms. Jennie McPhail, Dr. Igor Mastikhin, Dr. Bryce MacMillan, Dr. Florin Marica, Dr. Ben Newling, Dr. Konstantin Romanenko and Mr. Rod MacGregor. Thanks also to the students of the MRI Centre that have been sharing with me problems and happiness during this period. Especial mention for my good friends Jesús Cano, Han Hui, Michael Li, Colleen Muir, Olusegun Adegbite, Dan Xiao, Fred Goora, Clevan Lamason, Pan Guo and Guangzhi Liao.

I also want to thank Ms. Kristel Desjardins and Dr. Edmund Biden for their support during this period. Thanks to Dr. Pablo Prado and Dr. Gabriel LaPlante for their advice. Thanks a lot to Brian Titus for his quick answers to my rushed requests.

Even when this thesis covers the last four years working with Magnetic Resonance, I want to acknowledge all the people that contributed to my first steps in this field. Special thanks for Dr. Carlos Cabal, Dr. Evelio González, Dr. Juan Miguel Parra, Dr. Alejandro Burdelois, Nibardo López M.Sc., and Dr. Rigoberto Pérez de Alejo.

To stay away from home for a long period has only been possible because of the support of a group of friends. They have been looking after my family and attending everything to make things easier for me. Thanks a lot for all of them especially Cuadra, Cecilia, Alberto, Sóñora, Denis, Acelis, Liliana and Walter. Also, I would like to thank my friends Carlos Diaz Novo and Pius Ariho for being like brothers for me during this period, supporting me and making me laugh when everything was dark and sad.

The last lines of these acknowledgments are for my family. Thanks a lot for pushing me to face new challenges and conquer new success, without their support

nothing would be possible. Thanks for my daughters Claudia Camila and Adriana, I hope in the future they will understand why dad went away from home for this long period. Hopefully, our separation will be a good example for them about how much one has to be willing to pay for conquering a dream.

The last person to be acknowledged deserves to be also an author of this work, my wife Haydeé Cruz Vadell. Only her strength has made possible for me to reach my goals. Thanks a lot for assuming alone our common responsibilities while I was doing just what I like to do, studying and learning.

Table of Contents

List of Tables

List of Figures

List of Abbreviations

1D	One Dimensional
2D	Two Dimensional
CP	Carr-Purcell
CPMG	Carr-Purcell-Meiboom-Gill
CPS	Composite core plug sample
DC	Direct Current
FID	Free Induction Decay
FPGA	Field Programmable Gate Array
GA	Gradient Amplifier
MR	Magnetic Resonance
MRI	Magnetic Resonance Imaging
NMR	Nuclear Magnetic Resonance
MOUSE	Mobile Universal Surface Explorer
PA	Power Amplifier
PC	Personal Computer
ppm	part per million
PreA	Preamplifier
RF	Radio Frequency
SGSTE	Static Gradient Stimulated Echo
SLR	Shinnar-Le Roux
SNR	Signal-to-Noise-Ratio

UNB	University of New Bruswick
UMR	Unilateral Magnetic Resonance
VBF	Variable Bandwidth Filter

List of Symbols

Acq.	Acquisition
Att	Attenuation
B_0	Static magnetic field
B_1	Radio frequency magnetic field
B_{eff}	Effective magnetic field
θ	Flip angle
ΔB_0	Variation of the static magnetic field
ΔE	Difference in energy
Δf	Bandwidth in Hz
$\Delta\omega_0$	Bandwidth in radians
Δz	Resolution along the z axis
D	Self diffusion coefficient
DT	Dead time
F	Noise figure
γ	Gyromagnetic ratio
G	Gradient intensity
η	Filling factor
HP1	Non selective pulse
$\hbar$	Planck's constant divided by 2π

I	Echo amplitude
K	Inhomogeneity factor
k	Boltzmann's constant
K_p	Proportionality constant
L_D	Length of diffusion
l	Length of the magnet along the x direction
λ	Wavelength
μ_0	Permeability of free space
M	Net magnetization
M_0	Equilibrium net magnetization
N	Spin population
n	Rotation axis
ξ	Induced voltage
Q	Quality factor
R	Radius of the probe
R_{opt}	Optimum radius
SP	Suppression pulse
S_o	Oil saturation
S_w	Water saturation
τ	MR pulse sequence delay
τ_r	Ringing time constant
T	Sample temperature

T_c	Coil temperature
T_1	Longitudinal relaxation time
T_2	Spin-spin relaxation time
T_2^*	Effective Transverse relaxation time
T_{2eff}	Effective Spin-spin relaxation time
t	Time
t_{acq}	Acquisition time
t_{rf}	RF pulse duration
TE	Echo time
S/V	Surface to volume ratio
V_s	Sample volume
ψ	Signal to noise ratio in a NMR experiment
ω_o	Resonance frequency
ω_1	Nutation frequency
W	Width of the magnet blocks along the z axis
$\hat{x}, \hat{y}, \hat{z}$	Unit vectors in Cartesian coordinates
y_{ss}	Position of the sensitive spot along the z axis

Chapter 1

Introduction

In just a few decades Magnetic Resonance (MR) has become an important tool in almost all areas of human development. Medicine, materials science, non-destructive testing and the petroleum industry are examples of areas where MR is an indispensable tool today. This spread has pushed the technique out of the laboratory, creating opportunities for new applications and new challenges. In this context, Unilateral Magnetic Resonance (UMR) has emerged in recent years as a powerful technique to explore samples of arbitrarily large size.

Traditionally, MR has been performed in the bore of a closed magnet. In UMR the magnetic field is generated in a remote volume. New magnet designs have been developed and applied in diverse fields such as down-hole oil well logging, characterization of food products, medical applications, material analysis, artwork preservation and investigation of plants and soils. Nevertheless, because of the advantages and capabilities of this method, new applications are continually being developed.

As a part of this development the MRI laboratory at the University of New Brunswick has introduced three general classes of magnets for UMR. One, known as the three-magnet array, has shown great potential for further development because of its simplicity and robustness. This thesis proposes a group of solutions that overcome current limitations of the three-magnet array and broaden the range of its applications. The proposed solutions preserve the simplicity of the original design and make this approach suitable for many applications in UMR.

This thesis is organized as follows:

Chapter 2 includes a background discussion of MR in order to facilitate a better understanding of this thesis. The physical basis of the MR phenomenon, description of techniques and the hardware commonly employed is included. The unusual features of the MR experiment in inhomogeneous fields, and more specifically in UMR, are also analyzed in this chapter.

Chapter 3 details the building process of the three-magnet array focused on the homogeneous spot design. The criteria for building RF probes for this type of magnet is included in this chapter, as well as a description of the limitations of the original three-magnet array design and the proposed solutions. A handheld design employing the three-magnet array approach is also presented.

Chapter 4 describes an application of the three-magnet array for real-time monitoring of the cure process of an epoxy/polyamidoamine system. This chapter has been published as a paper in the journal NDT&E International.

Chapter 5 describes a new class of UMR magnets with an extended constant gradient employing the three-magnet array. A description of previous work in this area and measurements employing the constant gradient for diffusion measurements in rock core plugs and profiling is included. This chapter has been published as a paper in the Journal of Magnetic Resonance.

Chapter 6 presents the application of the three-magnet array, both uniform spot and constant gradient spots, for rock core plug analysis.

Chapter 7 deals with the application of selective excitation employing the three-magnet array. Practical implementations and measurements are discussed.

Chapter 8 presents the conclusions of this thesis and its contributions.

An additional work related to the design of a variable bandwidth filter for pure phase encoding MRI has been included as an appendix of this thesis. While it is not directly related to UMR, the work was undertaken during the development of this PhD project. It has been published as a paper in the Journal of Magnetic Resonance.

The measurements of the B_1 field presented in this thesis in Chapter 3, Fig. 3.10, were undertaken by Dr. Manuel Lores Guevara as a part of his research project at the UNB MRI Centre.

The measurements presented in Chapter 4 were undertaken in collaboration with Dr. Gabriel LaPlante of the University of Moncton. The idea of the application and all the knowledge related to the curing process of the resins were contributed by Dr. LaPlante.

The design of the experimental set up, implementation of the pulse sequences and all aspects related to UMR were developed by the author of this thesis.

For the experiments described in Chapter 6, the measurements of porosity profiles and T_2 mapping in homogeneous fields, utilized to confirm the results obtained by UMR, were undertaken by Dr. Florin Marica of the UNB MRI Centre. The flooding experiments employed to confirm the results obtained by UMR were undertaken in a 2 MHz homogeneous field NMR instrument by Dr. Guangzhi Liao of the UNB MRI Centre. Dr. Liao was also in charge of the sample manipulation for this experiment.

Chapter 2

Background

Nuclear Magnetic Resonance (NMR) as a physical phenomenon has been described in many commonly available, high quality, texts [1, 2, 3, 4]. This chapter presents a brief background description.

2.1 Magnetic Resonance

The magnetic resonance experiment can be undertaken only with specific atomic nuclei. Those with odd atomic weights and/or odd atomic numbers have a nonzero angular momentum, often called spin, and associated with it a magnetic moment [4]. Nuclei like ^{1}H, ^{31}P, ^{23}Na, exhibit this property and therefore can be studied with NMR experiments. Nevertheless, only the hydrogen nucleus will be considered hereafter since it is the most sensitive nucleus and ^{1}H is ubiquitous in nature.

In the absence of a static magnetic field, the orientation of the nuclear magnetic moments is random due to thermal motion. Therefore, at thermal equilibrium, no net magnetization exists for the macroscopic object [4]. When an external magnetic field is

applied, because of quantum mechanical considerations, the spins are oriented in only two possible directions, partially parallel or partially antiparallel with the magnetic field. The fact that the atomic nucleus has angular momentum precludes a perfect alignment; instead the spins will precess around the direction of the static magnetic field.

The frequency of precession ω_0 is known as the Larmor frequency (Eq. 2.1),

$$\omega_0 = \gamma B_0 \tag{2.1}$$

where B_0 is the magnitude of the static magnetic field, by convention oriented along the z axis with $\overrightarrow{B_0} = B_0\hat{z}$. The gyromagnetic ratio γ describes the relation between the angular momentum and magnetic moment of the nucleus. For hydrogen the gyromagnetic ratio is 2.675×10^8 rad/s /T.

The difference of population between the two possible orientations creates the net magnetization necessary for the NMR experiment. The difference of energy between the levels is determined by $\Delta E = \gamma\hbar B_0$ where $\hbar$ is Planck's constant divided by 2π. The ratio of populations, parallel $(N_\uparrow)$ and antiparallel $(N_\downarrow)$ related to B_0, can be calculated from the Boltzmann distribution:

$$\frac{N_\downarrow}{N_\uparrow} = e^{-\frac{\Delta E}{kT}} \tag{2.2}$$

Where k is Boltzmann's constant, ΔE is the difference in energy of the two states and T is the temperature. For a magnetic field of 1 T and a temperature of 300 K, the ratio of the populations helps explain the low sensitivity of the NMR experiment:

$$\frac{N_{\downarrow}}{N_{\uparrow}} = 0.9999932 \tag{2.3}$$

The individual magnetic moments almost entirely cancel due to the near equivalence of populations, leading to a small macroscopic net magnetic moment.

The equilibrium net magnetisation M_0, calculated as the vector sum of N microscopic magnetic moments is,

$$M_0 = \frac{N\gamma^2\hbar^2 B_0}{4kT} \tag{2.4}$$

The evolution of the sample magnetization, displaced from equilibrium, is described by the Bloch equation,

$$\frac{d\vec{M}}{dt} = \gamma\vec{M} \times \vec{B} \tag{2.5}$$

2.1.1 Excitation

Detection of the sample magnetization requires it be displaced from its equilibrium position (z axis). This is achieved with a RF excitation pulse, applied at the Larmor frequency. The excitation RF magnetic field, $\vec{B}_1 = \hat{x}B_1 \cos\omega_0 t$, produced by a

RF coil with its principal axis along the x axis in the transverse plane can be decomposed into two circularly polarized components [5]:

$$\vec{B}_{1\circlearrowleft}(t) = \frac{1}{2}B_1[\hat{x}\cos\omega_0 t + \hat{y}\sin\omega_0 t] \tag{2.6}$$

$$\vec{B}_{1\circlearrowright}(t) = \frac{1}{2}B_1[\hat{x}\cos\omega_0 t - \hat{y}\sin\omega_0 t] \tag{2.7}$$

Only one of them rotates in the same direction as the net magnetization and produces a torque pushing the net magnetization onto the transverse plane. Hereafter, only this component will be referred to as B_1. The duration t_{rf} and amplitude of the RF pulse determines the rotation angle θ.

$$\theta = \gamma B_1 t_{rf} \tag{2.8}$$

Figure 2.1 shows the effect of the RF pulse on the magnetization in the laboratory frame (a) and in a coordinate system rotating at the Larmor frequency (b).

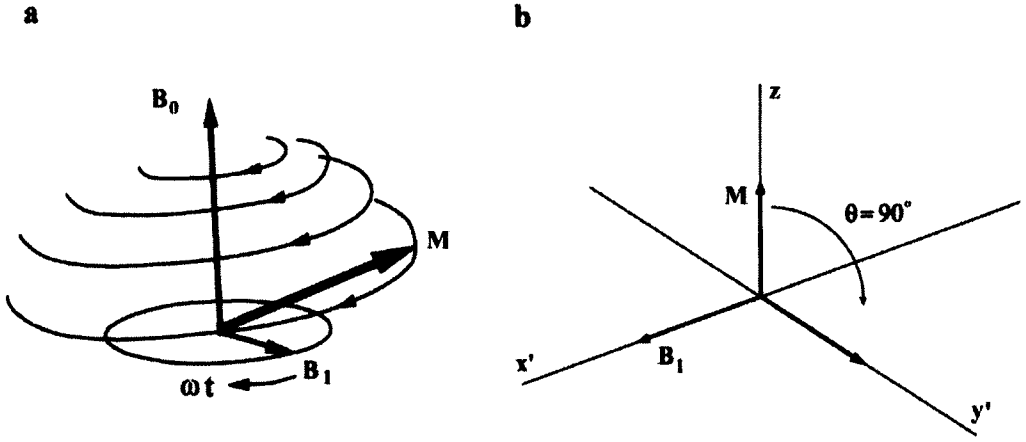

Figure 2.1. Evolution of the magnetization in the laboratory (a) [6], and rotating frame (b) under the effect of the magnetic field B_1 produced by the RF pulse.

2.1.2 Relaxation

Once the RF pulse has ceased, the magnetization, now in the transverse plane, starts returning to equilibrium. This process, known as relaxation, is governed by three time constants; T_1 controls the regrowth of the z component of the magnetization along the longitudinal axis because of the interaction between the spins and the lattice. T_2 and T_2^* govern the signal decay because of the loss of coherence in the transverse plane.

$$M_z(t) = M_0(1 - e^{\frac{-t}{T_1}}) \tag{2.9}$$

$$M_{xy}(t) = M_0 e^{\frac{-t}{T_2}} \tag{2.10}$$

The loss of phase coherence associated with T_2^* decay includes the effect of magnetic field inhomogeneities which can be removed by inverting the phase of the spin ensemble. For T_2 decay the dephasing is caused by the interchange of energy among spins and is irreversible. T_2 and T_2^* are related via Eq. 2.11.

$$\frac{1}{T_2^*} = \frac{1}{T_2} + \frac{\gamma \Delta B_0}{2\pi} \tag{2.11}$$

Figure 2.2 shows the recovery of the net magnetization along the z axis (a) because of the spin-lattice interaction and the decay in the transverse plane (b) produced by the spin-spin relaxation.

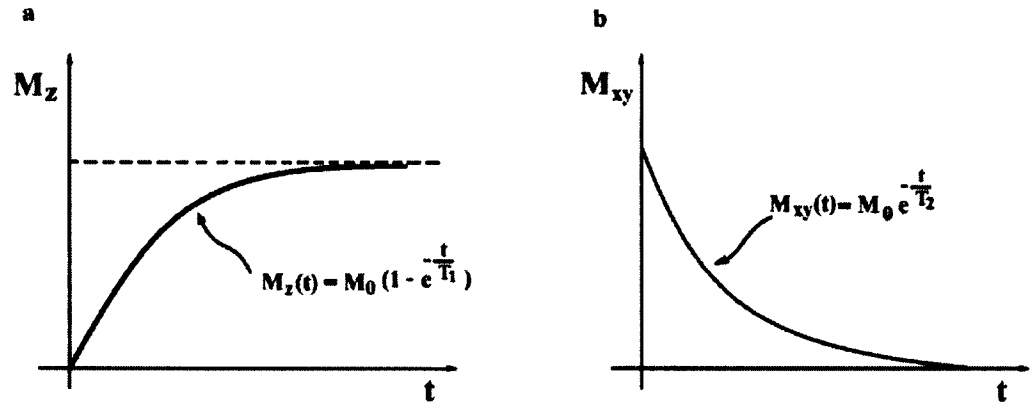

Figure 2.2. Sample magnetization returning to equilibrium along the longitudinal axis (a) and decaying in the transversal plane (b) during the relaxation process after a 90° pulse in absence of magnetic field inhomogeneities.

2.1.3 The signal

In order to receive the signal following RF excitation a pick up coil is placed in the transverse plane. The rotating magnetization induces a voltage in the coil. The voltage can be calculated, employing the reciprocity principle [7], through the following equation:

$$\xi = -\int_{sample} \left(\frac{\partial}{\partial t}\right)\{\vec{B}_0 \cdot \vec{M}_0\} dV_s \tag{2.12}$$

Equation 2.12 can be expressed in a simpler way (see Eq. 2.13) by considering a homogeneous distribution of B_1 over the sample space.

$$\xi = K\omega_0 (B_1)_{xy} M_0 V_s \cos \omega_0 t \tag{2.13}$$

where K is an inhomogeneity factor which may, if necessary, be calculated [7].

In practice the pick up coil is the same tuned circuit employed for the RF excitation.

2.1.4 Pulse sequences

The magnetic resonance experiment involves different events that must run in a synchronized way. The various events as a function of time during the experiment are known as the NMR sequence. Different sequences have been developed for diverse

applications [8]. The scope of this thesis principally involves only three sequences: spin-echo, CPMG and static gradient stimulated echo.

2.1.4.1 Spin-echo

The spin-echo sequence involves two RF pulses (see Fig.2.3). The first pulse, usually a 90° pulse, rotates the net magnetization to the transverse plane while the second, usually a 180° pulse, inverts the phase of the spins.

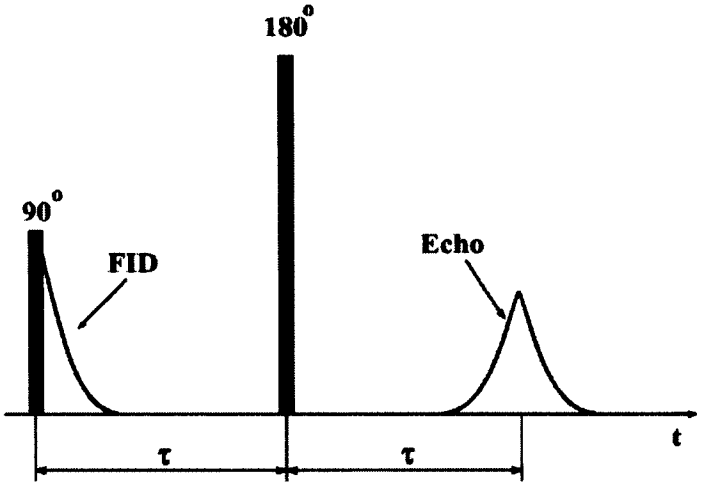

Figure 2.3. FID and echo signals obtained during a spin-echo experiment.

Once the net magnetization is displaced away from equilibrium by the first RF pulse, the spins begin dephasing because of magnetic field inhomogeneities and spin-spin relaxation. This dephasing process yields an exponential decay in the signal received by the coil in the transverse plane. This signal is known as the free induction decay (FID) and is governed by the time constant T_2^*.

The phase inversion produced by the second RF pulse, applied a time τ after the 90° pulse, initiates a rephasing process and therefore an increase of the signal in the

receiving coil. A time τ after the second pulse, the coherence of the spin system is recovered producing a maximum signal. Further dephasing after the echo maximum yields the signal decay again. The signal generated during this refocusing process is called an echo (see Fig.2.3) and the time 2τ, twice the time from the 90° to 180° pulse, is known as the echo time.

2.1.4.2 Carr Purcell Meiboom Gill

The Carr Purcell Meiboom Gill sequence [9], better known as CPMG (see Fig. 2.4), introduces a series of 180° pulses after the first echo obtained from a spin-echo sequence. The 180° pulses are separated 2τ from one other, creating a new echo at time τ after each 180° pulse. Assuming that the 90° pulse is applied along the x' direction, the 180° pulses should be applied along y'. This change, introduced by Meiboom and Gill [9] to the original Carr Purcell (CP) sequence [10], makes the sequence more robust to imperfections in the 180° pulses.

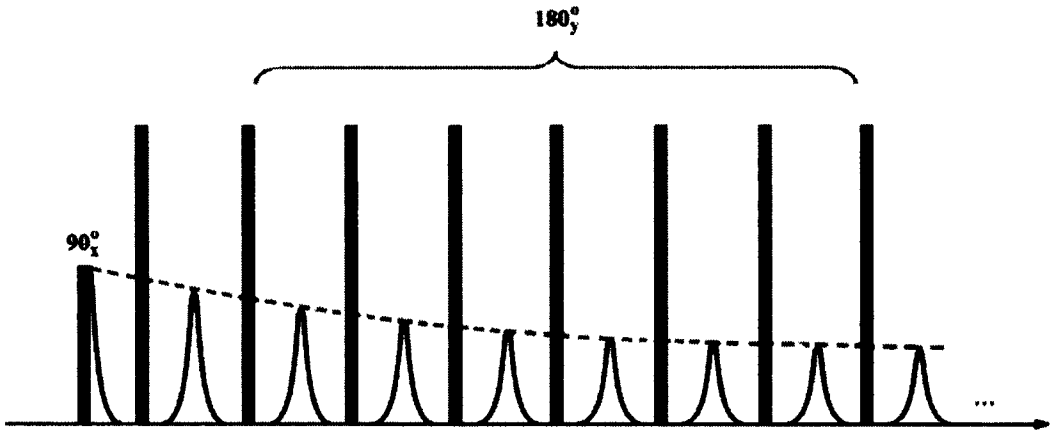

Figure 2.4. CPMG sequence. Multiple echoes can be generated employing multiple 180° pulses.

The consecutive refocusing process in CPMG removes the effect of magnetic field inhomogeneities. Nevertheless, the loss of coherence produced by the spin-spin relaxation cannot be recovered in the same way; therefore, the echo train decay is governed by the sample T_2. This means that by collecting the peak of the echoes and their time of occurrence, it is possible to fit Eq. 2.10 and measure T_2. Similar fitting could be done employing simple spin-echoes with different echo times, but the process would take more time. In addition, effects such as diffusion through underlying magnetic field gradients, can produce misleading results.

For T_2 measurement using CPMG the echo time should be kept as short as possible. As can be observed in Eqs. 2.14 and 2.15, in the presence of static magnetic field gradients through the sample, the measured effective T_2 (T_{2eff}) depends strongly on τ.

$$M(t) = M_0 e^{-\frac{\gamma^2 G^2 D \tau^2 t}{3}} \tag{2.14}$$

$$T_{2eff} = \frac{3}{\gamma^2 G^2 D \tau^2} \tag{2.15}$$

This effect can be employed for diffusion measurements [11], which provides an important insight into the study of molecular transport and dynamics inside the sample. The diffusion coefficient (D) can be calculated, for a magnetic field gradient (G), by

measuring T_{2eff} for different τ values and fitting the results to a straight line according to Eq. 2.16.

$$\ln\left(\frac{M(t)}{M_0}\right) = -\frac{\gamma^2 G^2 D \tau^2 t}{3} \tag{2.16}$$

The attenuation of observable signal by molecular diffusion through magnetic field gradients is very important for unilateral magnets since the magnetic field is inhomogeneous in the measurement volume, with a distribution of local gradients.

2.1.4.3 Static gradient stimulated echo

The static gradient stimulated echo sequence (SGSTE) is another option for measuring diffusion in the presence of static gradients, in this case employing three 90° pulses (Fig. 2.5).

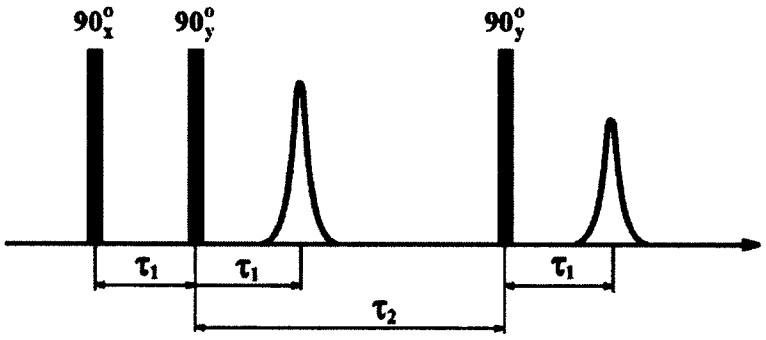

Figure 2.5. Static gradient stimulated echo sequence.

The first RF pulse rotates the sample magnetization into the transverse plane. After a time τ_1 a second 90° pulse rotates half of the dephased magnetization back to the z axis. The other half of the dephased magnetization creates an echo at time $2\tau_1$. The third RF pulse is applied at time $\tau_1+ \tau_2$ producing a stimulated echo at time $2\tau_1+ \tau_2$. During time τ_2 the magnetization aligned along the z axis does not suffer from spin-spin relaxation but only the indirect effect of diffusion and spin-lattice relaxation. The amplitude of the stimulated echo can be calculated with Eq. 2.17 [12].

$$M = \frac{M_0}{2} e^{\left[\frac{-\tau_2}{T_1} - \frac{2\tau_1}{T_2} - \gamma^2 D G^2 \tau_1^3 \left(\frac{2}{3} + \frac{\tau_2}{\tau_1}\right)\right]} \tag{2.17}$$

The first echo in SGSTE can be employed as a reference neglecting the effect of diffusion during the short time τ_1. Because τ_1 is the same after the first and the last RF pulses, the ratio of the echo amplitudes does not include the effect of the spin-spin relaxation; it is T_2 compensated. In fact this ratio, for different τ_1 values in a semilogarithmic scale, can be fit to a straight line to determine the diffusion coefficient. With this procedure there is no influence of T_1 on the measurement, therefore it could be said that the SGSTE measurement is relaxation compensated. Neglecting the effect of T_1, which is usually much longer than τ_2, the ratio of the amplitudes of the stimulated I and direct echo I_0 can be expressed as,

$$\ln\left(\frac{I}{I_0}\right) \approx -\gamma^2 G^2 \tau_1^2 \left(\tau_2 + \frac{2}{3}\tau_1\right) D \tag{2.18}$$

As a variation of the Laicher approach [13] for pulsed field gradients, Hurlimann [14] combined SGSTE and CPMG (Fig. 2.6) with a 16 step phase cycling to select only the contribution of the stimulated echo in order to obtain diffusion-T_2 distributions. The same sequence was employed by Rata [15] for measuring diffusion with a reference acquisition at very short τ_2. It was assumed that no diffusive attenuation occurred during the reference acquisition. In this case the SNR of the measurement was increased by adding all the echoes in the CPMG protion of the sequence as described in [16].

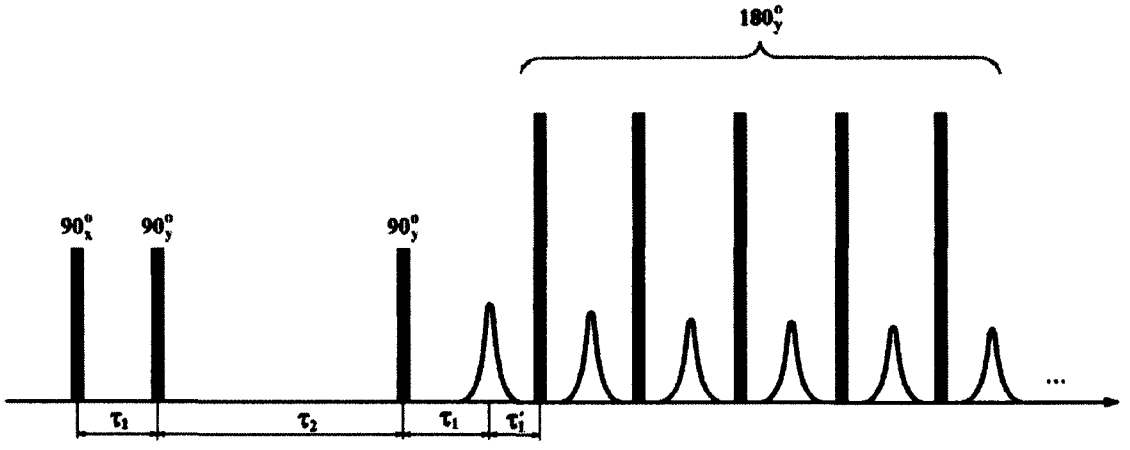

Figure 2.6. SGSTE sequence combined with CPMG.

2.1.5 Phase cycling

It is a common practice in NMR to change the phase of excitation pulses and acquisition in such a way that some undesirable effects can be cancelled without altering the signal [17, 18]. The simplest example is the two step phase cycling for removing DC components in the baseband electronics of the receiver. In this case the phase of two

successive excitations is shifted 180° producing the same signal 180° phase shifted from one acquisition to another. The signal from both acquisitions can be subtracted producing twice the signal of interest. Because the DC value does not depend on the signal phase, it remains the same during both acquisitions and therefore it is removed during the subtraction. More complex phase cycling of four, eight, sixteen or even more steps can be employed for cancelling other undesirable effects.

2.1.6 The NMR hardware

The NMR hardware involves almost all the areas of electrical engineering. Figure 2.7 shows a simplified schematic of an NMR system. It can be subdivided in different ways depending on the criteria for grouping the components. This description of each part is intended to provide only a general idea about each subsystem to understand their functions and their interactions during the NMR experiment.

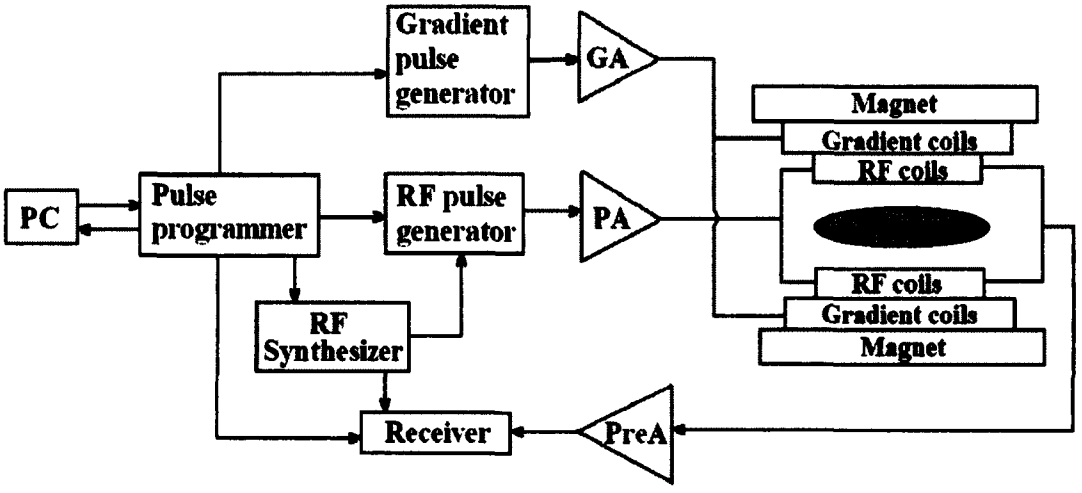

Figure 2.7. Block diagram of an NMR system where GA represents the gradient amplifier, PA the RF power amplifier and PreA the preamplifier.

2.1.6.1 Magnetic system

The magnetic system includes the elements around the sample related to the generation and reception of magnetic fields. The main part of the system is the static field magnet which should produce a homogeneous magnetic field over the volume of interest. For example, in clinical imaging a few parts per million (ppm) over a spherical volume 50 cm in diameter is typically required [5]. The magnet can be a permanent, resistive or a superconducting magnet.

A permanent magnet has the advantage of lower cost but it can be complicated to shape the pole faces to meet the requirements of homogeneity. Temperature drift is another non-trivial problem for this type magnet. Current permanent magnets made of rare earth elements can reach 1.3 T of remanence. Resistive magnets have the advantage of low cost of production and the fact that they can be easily turned off. Nevertheless, they consume power and the strength of the magnetic field is usually low. Superconducting magnets can generate very strong magnetic fields with very good homogeneity and stability. They do not need an external source of energy after the first activation but the cost of maintenance is usually high because they must be frequently recharged with liquid nitrogen and helium for their cooling system. In general, all magnets need additional shimming coils for improving the homogeneity of the magnetic field. Modern superconductive magnets for NMR experiments can reach magnetic field intensities of more than 20 T.

The magnetic system also includes the coils employed to generate the magnetic field gradients necessary for spatial encoding. They should produce a linear distribution

of magnetic field over the sample, usually along the three spatial dimensions. The fact that the magnetic field gradients should be applied in a pulsed manner makes more complex the design process for the gradient coils. Switching time, eddy current, intensity and linearity of the generated magnetic field are important elements during the design process. Different coil designs, from simple double-saddle coils to more complex "finger print" types, are employed.

The RF coils, also part of the magnetic system, generate a homogeneous B_1 field for exciting the sample and receive the signal during the reception process. In most cases, the same coil is employed for both excitation and reception. Homogeneity and quality factor (Q) are the main concerns during the RF coil design process. Solenoids, saddle coils, surface coils, and birdcage coils are the most popular types of RF probes. More modern designs include complex arrays of coils to obtain better performance during the excitation and reception of the signal.

2.1.6.2 Excitation system

The excitation system includes the RF pulse generator, in charge of the generation and translation in frequency from baseband to the Larmor frequency of the RF pulse, and the power amplifier (PA in Fig. 2.7) which guarantees an adequate level of power during the excitation. Current power amplifiers are designed by combining the output of two or more high efficiency stages of lower power. In modern NMR systems, the pulse generator is almost completely digital, frequently employing FPGA circuits, and the power amplifier is sometimes substituted by an array of amplifiers coupled to an array of independent RF coils.

2.1.6.3 Receiver

The receiver controls amplification and processing of the NMR signal. It is probably the most sensitive part of the NMR scanner. Special care should be taken during the design process to avoid distortion of the signal ensuring maximum SNR and immunity to interference. It includes a preamplifier (PreA in Fig. 2.7), which is placed close to the receiving coil and must guarantee a very low noise figure for the receiver. The NMR receiver should have synchronous quadrature detection. Most modern NMR receivers are completely digital after the RF amplifier. Modern MRI systems employ parallel reception with arrays of digital receivers coupled to arrays of receiving coils.

2.1.6.4 Synthesizer

In any NMR system it is necessary to generate signals at different frequencies to produce the change of frequency from baseband to the Larmor frequency in the pulse generator, or vice versa in the receiver. Sometimes translation in frequency requires more than one stage and therefore more than one frequency. All these signals at different frequencies are generated by the synthesizer. Nevertheless, modern systems, with increasing digitization do not require analog signals and numerical generators are employed instead.

2.1.6.5 Gradient system

The gradient system, formed by the gradient pulse generator and the gradient amplifier (GA in Fig. 2.7), should generate pulses to produce the desired magnetic field gradient. The requirements of high power output and fast switching time employing an

inductive load can make the process of design and adjustment very challenging. Contemporary gradient amplifiers are based on switching transistors.

2.1.6.6 Digital control system

All the electronics of the NMR system should work in a synchronous manner. The pulse programmer is the main part of the control system and generates all the time slots and the activation signals for each subsystem during the experiment. Additional components for communication and control, for example temperature control, are also included in this system. In modern MRI systems the control system is based on FPGAs with the addition, in some cases, of microcontrollers.

In general, the operation of a NMR system starts from setting all the parameters for the measurement in the computer of the system. Some signals will go directly to change parameters in the electronics through the control system and others will go to the pulse programmer for implementing the pulse sequence. Once the experiment commences, the pulse programmer generates the pulses for gradient encoding and RF excitation. Those pulses are amplified to the appropriate level and sent to the magnetic system. During the relaxation process the signal is received, preamplified, processed in the receiver according to the parameters of the experiment, and sent to the computer for further processing and display.

2.2 Magnetic resonance in inhomogeneous fields

In the previous sections it was assumed, as a necessary condition for the magnetic resonance experiment, that the static magnetic field was homogeneous. Nevertheless, in

some applications it is impossible to achieve this condition. For example, for imaging solid samples, which usually have a short T_2, the gradient must be switched very rapidly. Therefore, in order to maintain a good resolution (Δz) its intensity (G) should be increased (see Eq. 2.19). Switching high intensity gradients at high speed is very demanding for the gradient amplifiers. In some cases static gradients are a much better solution.

$$\Delta z = \frac{1}{\gamma G t_{acq}} \tag{2.19}$$

In some cases the sample size is larger than the bore of the magnet and therefore the experiment must be run outside the magnet, where the homogeneity of the magnetic field is greatly reduced.

To run the NMR experiment in inhomogeneous fields means that some of the spins do not rotate at the frequency of the excitation. In this case those spins precess in the rotating frame with a frequency ($\Delta\omega_0$) that could be interpreted as a magnetic field in the z direction (see Fig. 2.8 from [4]).

$$\Delta B_0 = \frac{\Delta\omega_0}{\gamma} \tag{2.20}$$

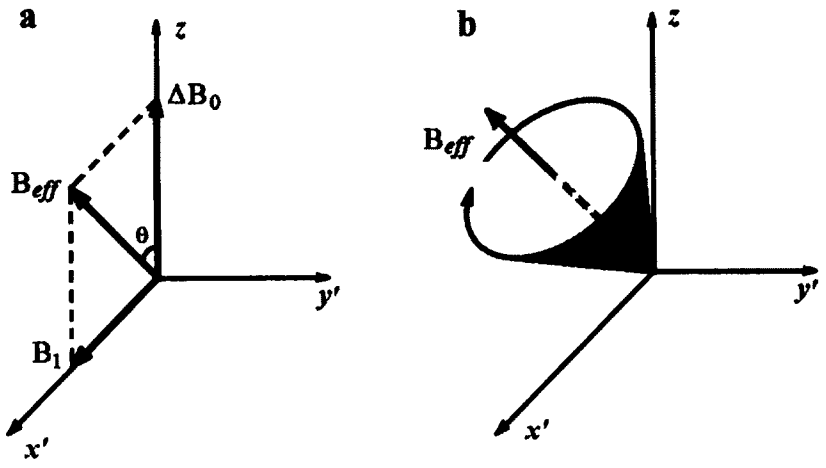

Figure 2.8. Off-resonance excitation in the rotating frame, adapted from [4]. Effective magnetic field in the rotating frame (a) and rotation of the magnetization around the effective field (b).

This effective magnetic field ΔB_0 associated with the off-resonance condition combines with B_1 producing an effective magnetic field B_{eff}. Therefore, during the excitation, the magnetization rotates around B_{eff} instead of B_1. The frequency of rotation and the angle of B_{eff} can be determined with Eq. (2.21) and Eq. 2.22 respectively.

$$\omega_{eff} = \sqrt{\Delta\omega_0^2 + \omega_1^2} \tag{2.21}$$

$$\theta = \arctan\left(\frac{\omega_1}{\Delta\omega_0}\right) \tag{2.22}$$

This behavior leads to the fact that part of the magnetization remains in the z axis after a 90° pulse creating additional complications for multipulse sequences such as CPMG.

2.2.1 CPMG in inhomogeneous fields

As outlined above, the excitation with a 90° pulse in inhomogeneous fields will move only part of the magnetization into the transverse plane. This magnetization can be refocused employing an 180° pulse producing what is known as a direct echo. This refocusing pulse also affects the remaining magnetization along the z axis, rotating part of it to the transverse plane. In multipulse sequences, a third RF pulse again produces a refocusing of the magnetization moved onto the transverse plane by the first 90° pulse, which produces a new echo. Nevertheless, the part of the magnetization moved onto the transverse plane by the first 180° pulse will also be refocused, producing what is called an indirect echo. Therefore, after the second 180° pulse, all the echoes will have contributions from direct and indirect echoes.

Figure 2.9 adapted from [19] shows the spectrum of the first four echoes in a CPMG sequence and the spectrum of the echoes that contribute in an experiment with inhomogeneous B_0. The position of the net magnetization after the excitation is represented for each echo by a combination of symbols. Positions in the transverse plane are represented by "+" and "-" while "0" correspond to positions along the z axis. The whole trajectory of the magnetization before creating an echo is known as a pathway. Only the first echo is determined by an individual pathway. By convention "+" was

assumed as the position of the net magnetization during the acquisition. It can be observed that after the first echo all the echoes are the summation of contributions from different trajectories of the net magnetization. For each pathway the magnetization stays for different time periods in the transverse plane and along the z axis.

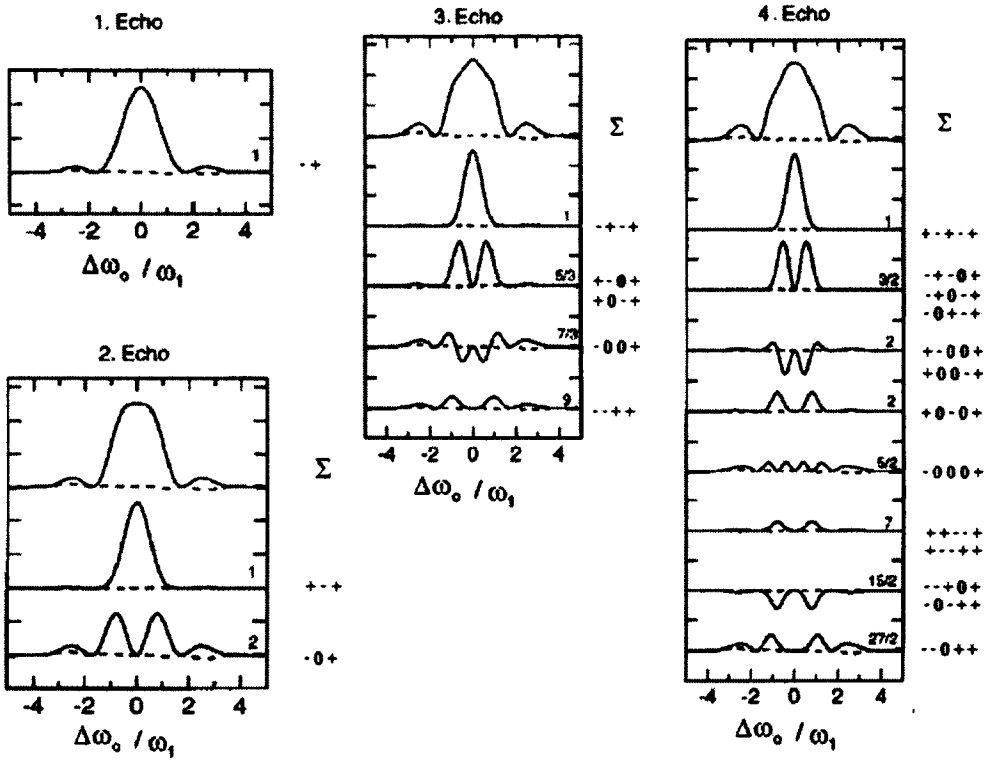

Figure 2.9. Spectrum of the first four echoes of a CPMG sequence adapted from [19]. The trajectory of the magnetization is represented beside each echo. The spectrum of each echo, top line in each sub figure, includes the contribution of different coherence pathways.

Because the magnetization in all the indirect echoes remains for a period of time along the z axis, this will add a T_1 component to the T_2 measurement during the CPMG acquisition [20]. It can be shown mathematically that the T_2 value obtained with a CPMG measurement (T_{2eff}) in inhomogeneous fields is a mixture of the true sample T_2 and the

sample T_1 [21]. The amount of the T_1 contribution depends on the average of the square of the projection of the effective rotation axis (n), which coincides with B_{eff} in Fig. 2.9, onto the z axis (see Eq. 2.23).

$$\frac{1}{T_{2eff}} = \frac{1}{T_2} + \langle n_z^2 \rangle \left(\frac{1}{T_2} - \frac{1}{T_1} \right) \tag{2.23}$$

The process of echo formation in inhomogeneous fields leads to an oscillation at the beginning of the CPMG decay [21]. The second echo is larger than the first echo, which is very different behavior than observed in homogeneous field experiments. After the first echoes the contribution of different pathways average out and the decay follows an asymptotic behavior governed by T_{2eff}.

Taking into account the particularities of the NMR experiment in inhomogeneous fields, Hurlimann [22] has suggested a reduction of the time τ between the 90° and the first 180° pulse as an effective way to increase the SNR during a CPMG measurement in inhomogeneous fields. The reduction in time can be calculated employing Eq. 2.24. The negative sign means that τ_{opt} should be deducted from the desired τ value.

$$\tau_{opt} = -2\frac{t_{90}}{\pi} \tag{2.24}$$

2.2.2 Adjusting the excitation power

MR in homogeneous fields permits simple procedures for setting the proper amplitude or duration for the 90° pulse, for example simply maximizing the echo signal. These ideas do not work well in the presence of strong inhomogeneities. As shown by Benson and McDonald [23] the maximum signal in inhomogeneous fields is obtained for an excitation pulse of 130°. Hence, they suggest to multiply by $\frac{10}{13}$ the amplitude of the pulse which produces the maximum amplitude as a method for setting the 90° pulse.

Bain and Randall [24] have shown that a series of 90° pulses produces a pattern of amplitudes that can be used to set the correct value for the RF pulse. For a sequence $90^{\circ}_{x} - [\tau - 90^{\circ}_{x} - echo]_{n}$, the amplitude of the echoes should be 1; $\frac{1}{2}$; $-\frac{1}{2}$; $-\frac{3}{8}$; ···; and for a sequence $90^{\circ}_{x} - [\tau - 90^{\circ}_{y} - echo]_{n}$ the pattern should be 1; $\frac{3}{2}$; $\frac{3}{2}$; $\frac{11}{8}$; ···. Randall et al. [16] have also shown that for pulses narrower than 5 μs the maximum of the echo coincides with the 90° pulse.

For experiments employing the three-magnet array the power is maximized in order to keep the RF pulse as narrow as possible. This allows employing the maximization of the first echo as the criterion for setting the pulse length for the pulses. Both pulses are maintained at the same duration with full power for the 180° pulse and half the voltage for 90°.

2.2.3 Diffusion measurement in inhomogeneous fields

From section 2.2.1 it can be observed that the different pathways the magnetization follows during a pulse sequence results in different times spent in the transverse and longitudinal directions. This yields different relaxation behavior for different pathways and also means that diffusion attenuation is different for the direct and indirect echoes [12]. Equation 2.25 shows the mathematical expression for the echo attenuation during a spin-echo experiment (direct echo). A similar expression for stimulated (indirect) echoes was previously stated in Eq. 2.17 from Section 2.1.4.3.

$$M = M_0 e^{-\frac{2\tau_1}{T_2} - \frac{2}{3}\gamma^2 D G^2 \tau_1^3} \tag{2.25}$$

The fact that the resultant echoes are the sum of direct and indirect echoes, all of them with different sensitivities to diffusion, introduces another complication for measuring diffusion in inhomogeneous fields. Hurlimann [19] has shown that phase cycling is the best method for isolating specific pathways and improving the quality of the measurement. Hurlimann [25] has also shown that this effect can be employed for fast diffusion measurements. By properly setting the time for the RF pulses, it is possible to encode diffusion and T_1 in the shape of the echo produced by the addition of the individual echoes of the CPMG decay. This allows the measurement of these parameters in a single scan.

2.3 Unilateral Magnetic Resonance

In many NMR measurements it is desirable to measure samples whose sizes are larger than the magnet bore. In other cases it is not possible to make the measurement of interest in the laboratory. The best solution in this case is to carry out the experiment on one side of a portable magnet that can be easily positioned close to the sample. This technique is known as Unilateral Magnetic Resonance (UMR).

UMR has become a powerful tool to explore samples of arbitrary size; permitting magnetic resonance experiments on more complex and challenging samples. A wide range of applications have been developed in different areas such as down-hole oil well logging [26], biomedicine [27], concrete materials analysis [28] and characterization of food products [29]. The first area of application is now ubiquitous in the oil industry.

The main element in the UMR experiment is the magnet employed to create the static magnetic field. Unfortunately, as described by Maxwell's equations, the divergence of the magnetic field is equal to zero, therefore it is not possible to obtain a homogeneous field on one side of a single magnet.

Different magnet designs have been proposed to create an MR compatible static magnetic field. Three main classes can be easily differentiated taking into account the distribution of the static magnetic field. In the first class both B_0 and B_1 are inhomogeneous. The second class includes those magnets designed to produce a relatively homogeneous B_0 field in a defined region of space. The third class of unilateral magnets features a linear magnetic field distribution (constant gradient) in a region of

interest which is suitable for profiling and diffusion measurements. We consider these three classes of design systematically in the sections that follow.

A good review related to the origin and development of UMR systems can be found in [30].

2.3.1 Working with inhomogeneous B_0 and B_1

For the first class of unilateral magnets the orientation of the magnets and RF coil are arranged in such a way that the grossly inhomogeneous B_0 and B_1 remain perpendicular in specific regions which, in conjunction with the RF excitation bandwidth, defines a sensitive spot for the measurement. This approach can produce much higher intensities of the static magnetic field which compensates for the small size of the sensitive spot that can be achieved. Because of the highly inhomogeneous static magnetic field, the diffusion attenuation effect is very strong in this configuration.

The best example for this type of magnet is the MOUSE (MObile Universal Surface Explorer) [31, 32]. As shown in Fig. 2.10 the MOUSE combines the inhomogeneous field produced by two magnet bars joined by a ferromagnetic material, with the B_1 magnetic field produced outside a solenoid. Even when both fields are inhomogeneous, there is a region of space where they remain perpendicular creating a small spot for the NMR measurement.

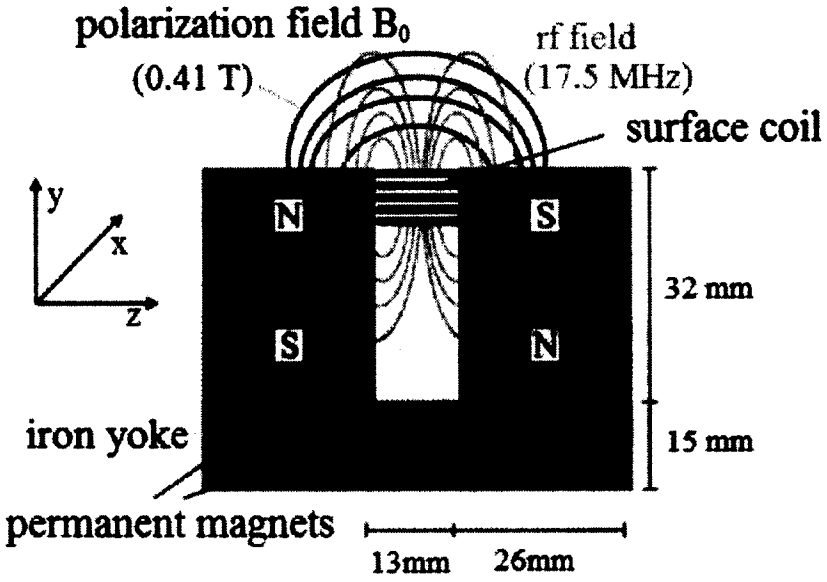

Figure 2.10. NMR MOUSE reproduced from [32]. The sensitive spot is created by combining the B_0 and B_1 inhomogeneities in a constructive way.

Chang et al. [33] have proposed another approach to the same idea but employing a Halbach [34] magnet built employing 8 cylindrical magnets of NdFeB. In this case the stray field of the magnet is combined with the field produced by a double-sided planar spiral coil.

2.3.2 Homogeneous spots

In this approach, different magnet blocks are combined in order to create a region where the magnetic field is somewhat homogeneous. It should be noted that even in this case the homogeneity in the sensitive spot is greatly reduced in comparison with closed magnets. This variant yields large spots for RF excitation and reduces diffusive attenuation by molecular motion through underlying magnetic field gradients.

Jackson et al. [35] proposed a combination of two cylindrical magnets, with the magnetic fields oriented longitudinally, placed in opposition along the same axis with a gap in between, as presented in Fig. 2.11. This design produces a toroidal homogeneous region with the magnetic field oriented in the radial direction. The excitation and reception coil in this case could be a simple solenoid placed between both magnets, in such a way that its stray field B_1 remains perpendicular to B_0 in the toroidal region. The stray field will always be weak which limits SNR by the principle of reciprocity.

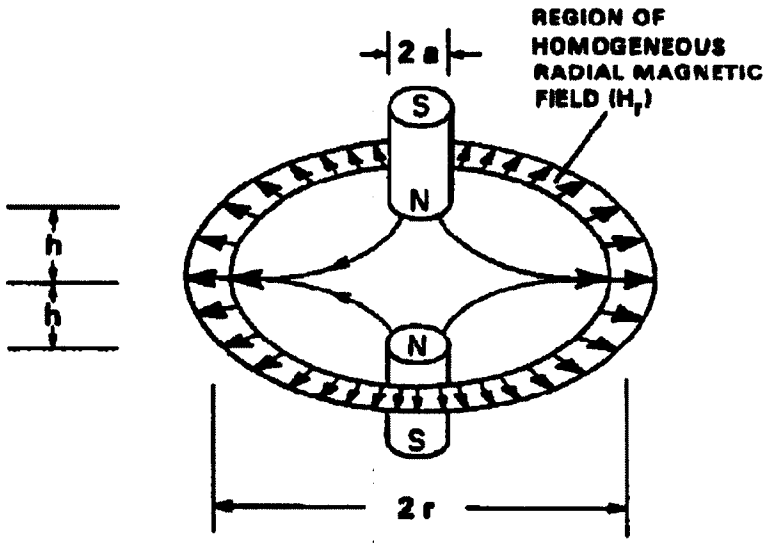

Figure 2.11. Toroidal homogeneous spot created with two cylindrical magnets, reproduced from [35].

Kleinberg et al. [36] proposed another configuration combining three-magnet blocks in the configuration shown in Fig. 2.12. In this way, a homogeneous spot was created on one side of the array. The static magnetic field is oriented perpendicular to the

surface of the array, which complicates the design of the RF probe. In this case a ferrite-loaded half-coaxial antenna was employed.

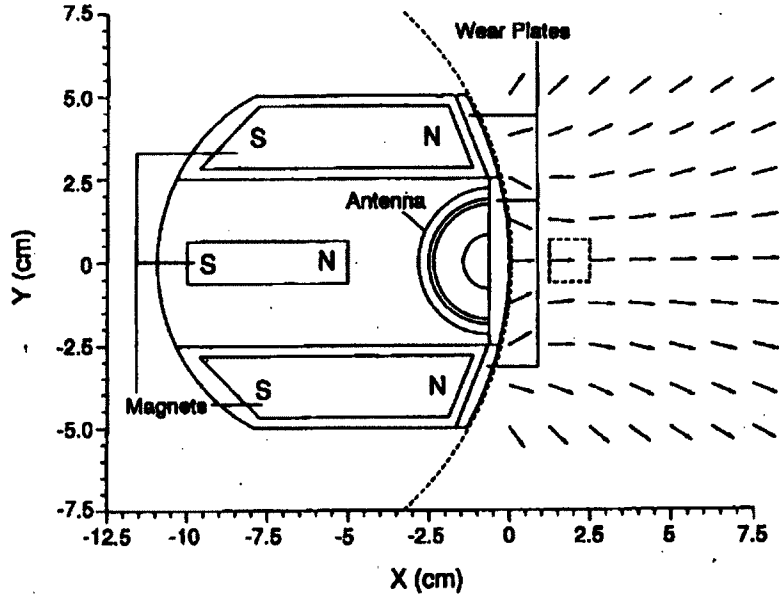

Figure 2.12. Cross section of the apparatus proposed by Kleinberg et al, reproduced from [36]. The homogeneous spot has been marked with a dashed square.

A similar approach was introduced by Fukushima and Jackson [37]. A smaller but more homogeneous spot was obtained (see Fig. 2.13) by rotating the Kleinberg et al. design to make it radially symmetric about the longitudinal axis (x in Fig. 2.12). As in the previous case, the static field is perpendicular to the transverse section of the cylinder, therefore B_1 should be oriented parallel to the surface which leads to less sensitive RF probe designs. Nevertheless, the more homogeneous spot with stronger B_0 reduces these signal losses, to some extent, because of the size of the spot and the type of probe.

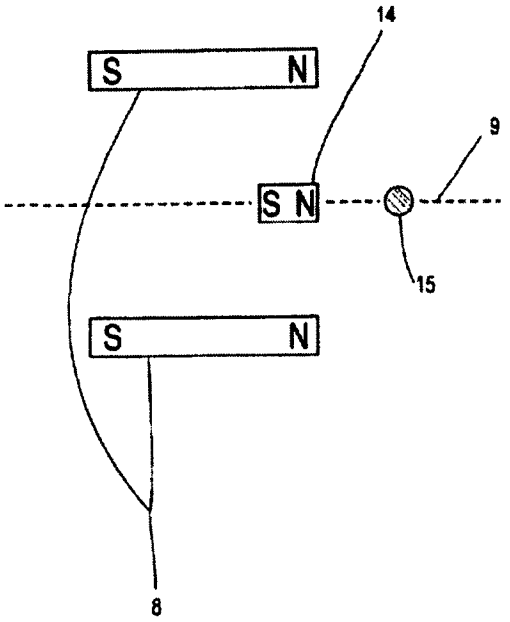

Figure 2.13. Longitudinal section of the Fukushima and Jackson design reproduced from [37].

A different approach was introduced by Marble et al. In this case, a shaped pole piece placed on top of an array [38, 39] or a single magnet block [39] produces the desired magnetic field distribution. The contour of the ferromagnetic pole piece is obtained from an analytically derived expression for the magnetic scalar potential [40].

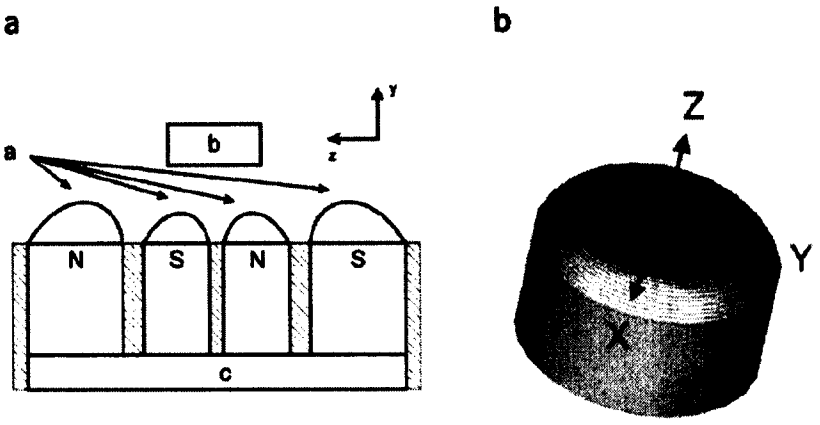

Figure 2.14. Designs employing Marble et al. approach employing a) a magnet array, reproduced from [38] and b) single cylindrical magnet, reproduced from [39].

Marble et al. [41] also introduced a three-magnet array to produce a homogeneous spot. This approach is very simple and compact. The magnetic field is parallel to the surface which allows the utilization of more sensitive RF probes. The three-magnet array is the basic magnet configuration employed in this thesis. More details about this idea are discussed in Chapter 3.

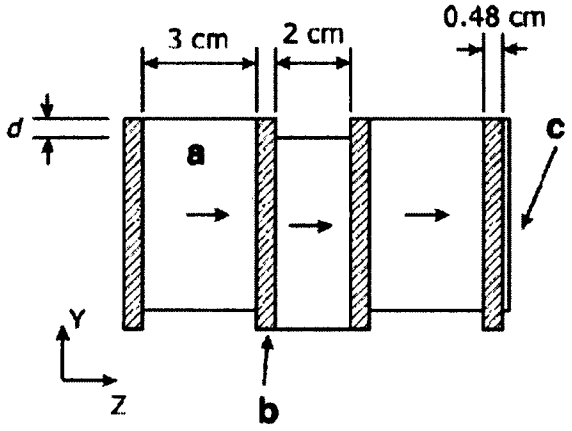

Figure 2.15. Three-magnet array introduced by Marble et al., reproduced from [41]. The simplicity of the approach makes the design very robust and suitable for diverse applications.

A more complex design, based on the original idea of the NMR MOUSE, has been presented by Perlo et al. [42]. In this case, a complex set of magnet blocks produces the desired homogeneous spot (Fig. 2.16). The B_0 magnetic field can be very homogeneous allowing spectroscopy measurements in some cases. Nevertheless, the fact that several different magnet blocks must be adjusted to achieve the desired field homogeneity, makes the approach complex and difficult to reproduce.

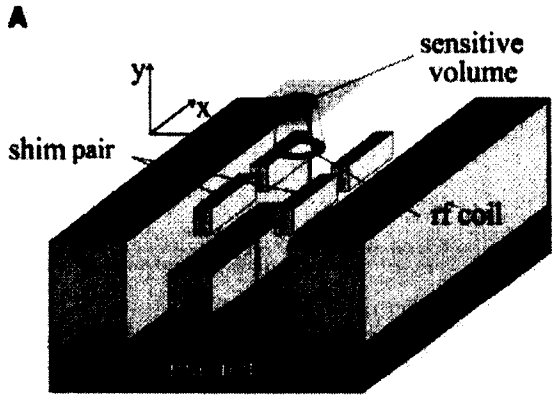

Figure 2.16. Magnet design proposed by Perlo et al. reproduced from [42]. Improved homogeneity can be obtained but the number of magnet components makes the array very complex.

More recently Chang et al. [43] have proposed a variation of their original single block design [44] by adding a small shimming block above with the magnetic field oriented in the opposed direction.

2.3.3 Constant gradient

The third class of unilateral magnets features a linear magnetic field distribution (constant gradient) in a region of interest which is suitable for profiling (Fig. 2.17) and

diffusion measurements. In a sense these are magnets of the first class where the inhomogeneity of B_0 is controlled to yield a linear variation of field. The profile measurement [1] yields a 1D representation of the effective spin density of an object as a function of position (see Eq. 2.1). The diffusion measurement, as previously mentioned, allows measuring the diffusion coefficient or the effect of the molecular motion on the NMR signal, which provides important information about the dynamics inside the sample.

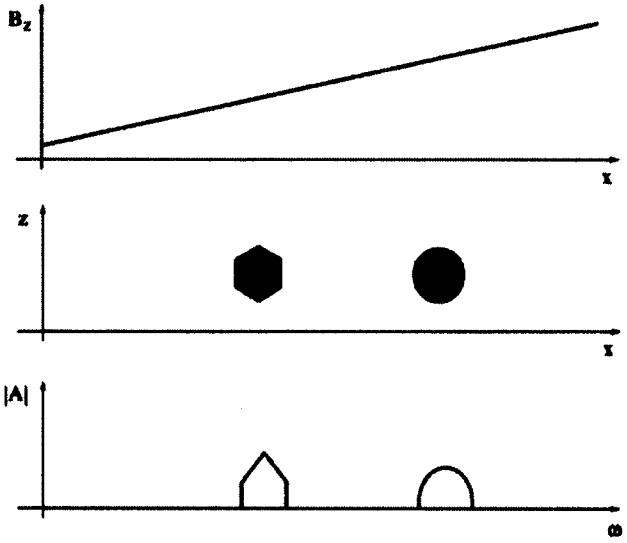

Figure 2.17. Effect of a constant gradient on the sample. The Fourier transform and the dependence between magnetic field and frequency described by the Larmor equation allow a representation of the sample profile.

A more detailed discussion of unilateral magnets with a constant magnetic field gradient can be found in Chapter 5 of this thesis.

References

[1] E. M. Haacke, R. W. Brown, M. R. Thompson, and R. Venkatesan, Magnetic Resonance Imaging, Physical Principles and Sequence Design. New York: John Wiley and Sons, 1999.

[2] E. Fukushima and S. B. W. Roeder, Experimental NMR. A Nuts and Bolts Approach. Reading, Boulder: West View Press, 1981.

[3] C. N. Chen and D. I. Hoult, Biomedical Magnetic Resonance Technology. Bristol: Adam Hilger, 1989.

[4] Z. P. Liang, P. C. Lauterbur, Principles of magnetic resonance imaging. New York: IEEE Press, 2000.

[5] J. Jin, Electromagnetic analysis and design in Magnetic Resonance Imaging, CRC Press, NY, 1999.

[6] P. T. Callaghan, Principles of Nuclear Magnetic Resonance Microscopy, Clarendon Press, New York, 1991.

[7] D. I. Hoult, R. E. Richards, The signal to noise ratio of the nuclear magnetic resonance experiments, J. Mag. Reson. 24, 71-85, 1976.

[8] M. A. Bernstein, K. F King, X. J. Zhou, Handbook of MRI pulse sequences, Elsevier Academic Press, Burlington, 2004.

[9] Meiboom S, Gill D. Modified spin-echo method for measuring nuclear relaxation times. Rev. Sci.. Instrum., 29, 688–91,1958.

[10] H. Y. Carr and E. M. Purcell, Effects of diffusion on free precession in nuclear magnetic resonance experiments, Phys. Rev., 94, 630–638, 1954.

[11] R. Kimmich, NMR Tomography, Diffusometry, Relaxometry, Berlin, Springer, 1997.

[12] R. Kimmich, W. Unrath, G . Schnur, E. Rommel, NMR measurement of small self-diffusion coefficients in the fringe field of superconducting magnets, J. Magn. Reson. 91, 136-140, 1991.

[13] G. Laicher, D. C. Ailion, A. G. Cutillo, Water Self-diffusion measurement in excised rat lungs, J. Magn. Reson. Series B 111, 243-253, 1996.

[14] M. D. Hurlimann, L. Venkataramanan, Quantitative measurement of two-dimensional distribution functions of diffusion and relaxation in grossly inhomogeneous fields. J. Magn. Reson. 157, 31-42, 2002.

[15] D. G. Rata. F. Casanova, J. Perlo, D. E. Demco, B. Blumich, Self-diffusion measurement by a mobile single-side NMR sensor with improved magnetic field gradient. J. Magn. Reson. 180, 229-235, 2006.

[16] E.W. Randall, T.G. Nunes, G Guillot, P. R. Bodart. T_1-weighting of echo-trains in the stray-field for deuterium: prospects for imaging using long echo-train summation. Solid State Nucl. Magn. Reson. 14, 165-172, 1999.

[17] D. Hoult, The NMR receiver: A description and analysis of design. Prog. NMR Spect. 12, 41-47, 1978.

[18] D. D. Traficante, Phase-Sensitive Detection. Part II: Quadrature Phase Detection, Concepts Magn. Reson. 2, 181-195, 1990.

[19] M. D. Hurlimann, Diffusion and relaxation effects in general stray field NMR experiments, J. Mag. Res. 148, 367–378, 2001.

[20] G. Goelman, M. G. Prammer, The CPMG pulse sequence in strong magnetic field gradients with applications to oil-well logging, J. Magn. Reson. Series A 113, 11-18, 1995.

[21] M. D. Hurlimann, D. D. Griffin, Spin dynamics of Carr–Purcell–Meiboom–Gill-like sequences in grossly inhomogeneous B_0 and B_1 fields and application to NMR well logging, J. Magn. Reson. 143, 120–135, 2000.

[22] M.D. Hurlimann, Optimization of timing in the Carr-Purcell-Meiboom-Gill sequence, Magn. Reson. Imaging 19, 375–378, 2001.

[23] T. B. Benson and P. J. McDonald, Profile amplitude modulation in stray-field magnetic-resonance imaging, J. Magn. Res. A, 112, 17–23, 1995.

[24] A. D. Bain and E. W. Randall, Hahn spin echoes in large static gradients following a series of 90◦ pulses, J. Magn. Res. A, 123, 49–55, 1996.

[25] M. D. Hurlimann, Encoding of diffusion and T_1 in the CPMG echo shape: Single-shot D and T_1 measurements in grossly inhomogeneous fields. J. Magn. Reson. 184, 114–129, 2007.

[26] R. L. Kleinberg, A. Sezginer, D. D. Griffin, M. Fukuhara, Novel NMR apparatus for investigating an external sample, J. Magn. Reson. 97, 466–485, 1992.

[27] R. Haken, B. Blumich, Anisotropy in Tendon Investigated in Vivo by a Portable NMR Scanner, the NMR-MOUSE, J. Magn. Reson. 144(2), 195-199, 2000.

[28] P. F. de J. Cano-Barrita, A. E. Marble, B. J. Balcom, J. C. García, I. V. Masthikin, M. D. A. Thomas, T. W. Bremner, Embedded NMR sensors to monitor evaporable water loss caused by hydration and drying in Portland cement mortar, Cem. Concr. Res. 39, 324–328, 2009.

[29] S. Rahmatallah, Y. Li, H. C. Seton, I.S. Gregory, R. M. Aspden, Measurement of relaxation times in foodstuffs using a one-sided portable magnetic resonance probe, Eur. Food Res. Technol. 222, 298–301, 2006.

[30] B. Blümich, J. Perlo, F. Casanova, Mobile single-sided NMR. Prog. Nucl. Mag. Res. Sp. 52, 197–269, 2008.

[31] G. Eidmann, R. Savelsberg, P. Blumler, B. Blumich, The NMR MOUSE, a mobile universal surface explorer, J. Magn. Reson. A 122, 104–109, 1996.

[32] B. Blümich, P. Blumler, G. Eidmann, A. Guthausen, R. Haken, U. Schmitz, K. Saito, G. Zimmer, The NMR-MOUSE: Construction, excitation, and applications, Magn. Reson. Imaging, 16, 479–484, 1998.

[33] W. H. Chang, J. H. Chen, L. P. Hwang, Single-sided mobile NMR with a Halbach magnet, Magn. Reson. Imaging 24, 1095–1102, 2006.

[34] K. Halbach, Design of permanent multipole magnets with oriented rare earth cobalt material. Nucl Instrum Methods,169, 1– 10, 1980.

[35] J. A. Jackson, L.J. Burnett, J. F. Harmon, Remote (inside-out) NMR. III. Detection of nuclear magnetic resonance in a remotely produced region of homogeneous magnetic, J. Magn. Reson. 41, 411–421, 1980.

[36] R. L. Kleinberg, A. Sezginer, D. D. Griffin, M. Fukuhara, Novel NMR apparatus for investigating an external sample, J. Magn. Reson. 97, 466–485, 1992.

[37] E. Fukushima, J.A. Jackson, Unilateral Magnet having a remote uniform field region for Nuclear Magnetic Resonance, US Patent 6489872, 2002.

[38] A. E. Marble, I. V. Mastikhin, B. G. Colpitts, B. J. Balcom, An analytical methodology for magnetic field control in unilateral NMR. J. Magn. Reson. 174 78–87, 2005.

[39] A. E. Marble, I. V. Mastikhin, B. G. Colpitts, B. J. Balcom, Designing static fields for Unilateral Magnetic Resonance by a scalar potential approach, IEEE Trans. Magn., 43,5, 1903-1911, 2007.

[40] P.M. Glover, P.S. Aptaker, J.R. Bowler, E. Ciampi, P.J. McDonald, A novel high-gradient permanent magnet for the profiling of planar films and coatings, J. Magn. Res. 139, 90–97, 1999.

[41] E. Marble, I. V. Mastikhin, B. G. Colpitts, B. J. Balcom, A compact permanent magnet array with a remote homogeneous field. J. Magn. Reson. 186, 100–104, 2007.

[42] J. Perlo, F. Casanova, B. Blumich, Ex situ NMR in Highly homogeneous fields: ^{1}H spectroscopy. Science, 315, 1110-1112, 2007.

[43] W. H. Chang, C. Y. Chung, J. H. Chen, D. W. Hwang, C. H. Hsu, C. Yao, L. P. Hwang, Simple mobile single-sided NMR apparatus with a relatively homogeneous B_0 distribution, Mag. Reson. Imaging, 29, 869–876, 2011.

[44] W. H. Chang, J. H. Chen, L. P. Hwang, Single-sided mobile NMR apparatus using the transverse flux of a single permanent magnet, Mag. Reson. Imaging, 28, 129–138, 2010.

Chapter 3

Three-magnet array with homogeneous spot

The three-magnet array is one of the promising approaches to UMR developed by the UNB MRI Centre. In this design, the magnet blocks are arranged along the same axis, with the same magnetic field orientation, in a very safe (no repulsive forces) low energy configuration. The natural field orientation, B_0 parallel to the surface, permits the employment of more sensitive surface coils, for RF excitation and detection, than those employed when B_0 is perpendicular to the surface. The relatively simple mathematical expressions required for calculating the field distribution make this approach very easy to simulate.

The present chapter summarises the building process of the three-magnet array and outlines specific design improvements that solve limitations of the original design. A version of the three-magnet array for portable systems is also described.

3.1 Building process of the three-magnet array

The building process for the three-magnet array can be divided into different systematic stages. In this section we summarize the stages of design, simulation,

fabrication and characterization. We do so because the merits of this design give us confidence it will form the basis of many future studies in years to come.

3.1.1 Mathematical equations for the three-magnet array

The mathematical expressions for the magnetic field distribution can be obtained by considering each magnet block as the combination of two infinite current sheets of width W separated at a distance t (see Fig. 3.1) with currents in opposite directions [1]. In this way the magnetic field distribution can be readily calculated employing the Biot-Savart law [2]. Figure 3.1 taken from [1] illustrates this idea.

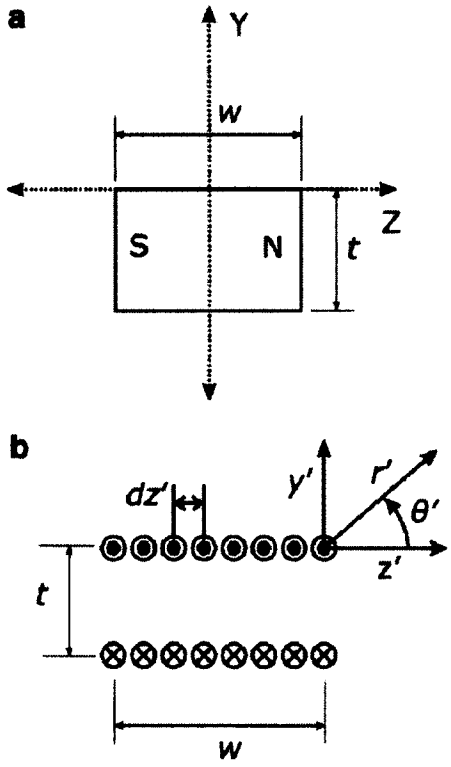

Figure 3.1. Magnet block (a) and its representation as two parallel sheets of current (b) reproduced from [1].

Equation 3.1 [1] corresponds to the magnetic field distribution of a single block. A mathematical equation for the magnetic field over the three-magnet array can be obtained by superposing the magnetic field B produced for the three-magnet blocks taking into account their dimensions and positions.

$$\vec{B}(z,y) = K_p\left[-tan^{-1}\left(\frac{z-\frac{w}{2}}{y}\right) + tan^{-1}\left(\frac{z+\frac{w}{2}}{y}\right) + tan^{-1}\left(\frac{z-\frac{w}{2}}{y+t}\right) - tan^{-1}\left(\frac{z+\frac{w}{2}}{y+t}\right)\right]\hat{z} + \frac{K}{2}\left[\log\left(\frac{y^2+\left(z+\frac{w}{2}\right)^2}{y^2+\left(z-\frac{w}{2}\right)^2}\right) - \log\left(\frac{(y+t)^2+\left(z+\frac{w}{2}\right)^2}{(y+t)^2+\left(z-\frac{w}{2}\right)^2}\right)\right]\hat{y} \quad (3.1)$$

Figure 3.2 shows the magnetic field distribution, obtained from the mathematical equation (solid line), along the vertical central line of the array. This distribution is the combination of the magnetic field produced by the central (dashed line) and the external blocks (dotted line) independently.

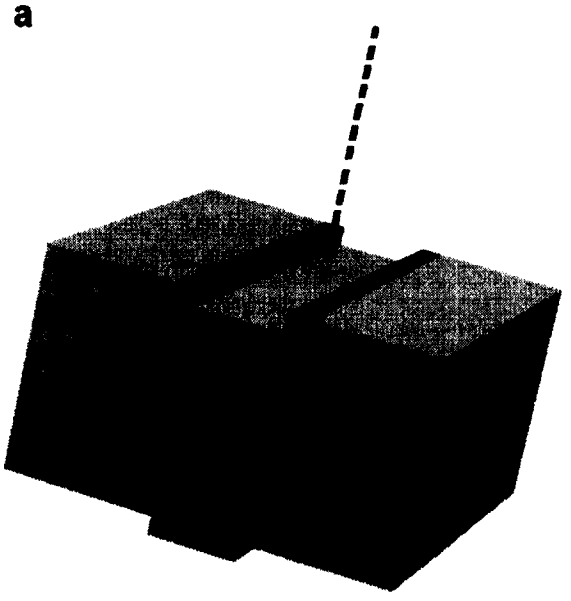

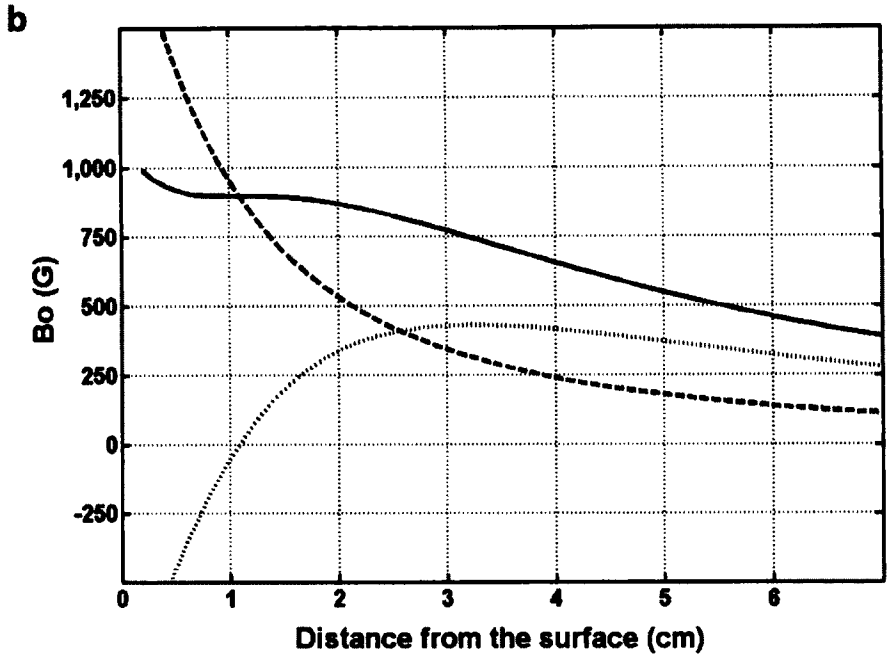

Figure 3.2 Vertical central line (dashed line) of the three-magnet array (a). Magnetic field distribution along the vertical central line (b). The desired field distribution (solid) is the combination of the field produced by the external blocks (dotted) and the central block (dashed).

By moving the central block of the array vertically, its magnetic field distribution along the vertical central line (dashed line in Fig. 3.2) is displaced in order to produce the desired homogeneous spot in the resultant curve (solid line in Fig. 3.2). The position of the spot is closely associated with the zero crossing in the dotted curve. This is principally determined by the separation between the external blocks.

3.1.2 Simulation

Even though the mathematical equation for the magnetic field distribution over the three-magnet array is relatively easy to obtain, it is more complicated to express one

desired design parameter as a function of the physical dimensions and position of the magnet blocks or vice versa. In this case, a numerical evaluation of Eq. 3.1 is preferred.

The professional software Vector Fields [3] is a powerful tool for magnetic field simulations. Nevertheless, its complexity makes it less suitable for the design process. MATLAB is a more flexible tool and therefore more appropriate for the design process.

The MATLAB function MagnetArrays, developed in a previous work [4], simulates the magnetic field produced by the three-magnet array by combining Eq. 3.1 for the three magnet blocks taking into account their relative positions and dimensions. Figure 3.3 shows the graphical interface of this function. Positions and dimensions of the magnet blocks can be introduced and changed in order to obtain the desired field distribution. Plotting and exporting the magnetic field distribution along horizontal and vertical lines are options included in this function.

The parameters set in Fig. 3.3 correspond to an array similar to the one described in [1]. It includes three magnet blocks of 10 cm length and thickness t of 5 cm. The width w is 3 cm for the external blocks and 2 cm for the central block. A non magnetic spacer of 4.76 mm is employed to separate the blocks.

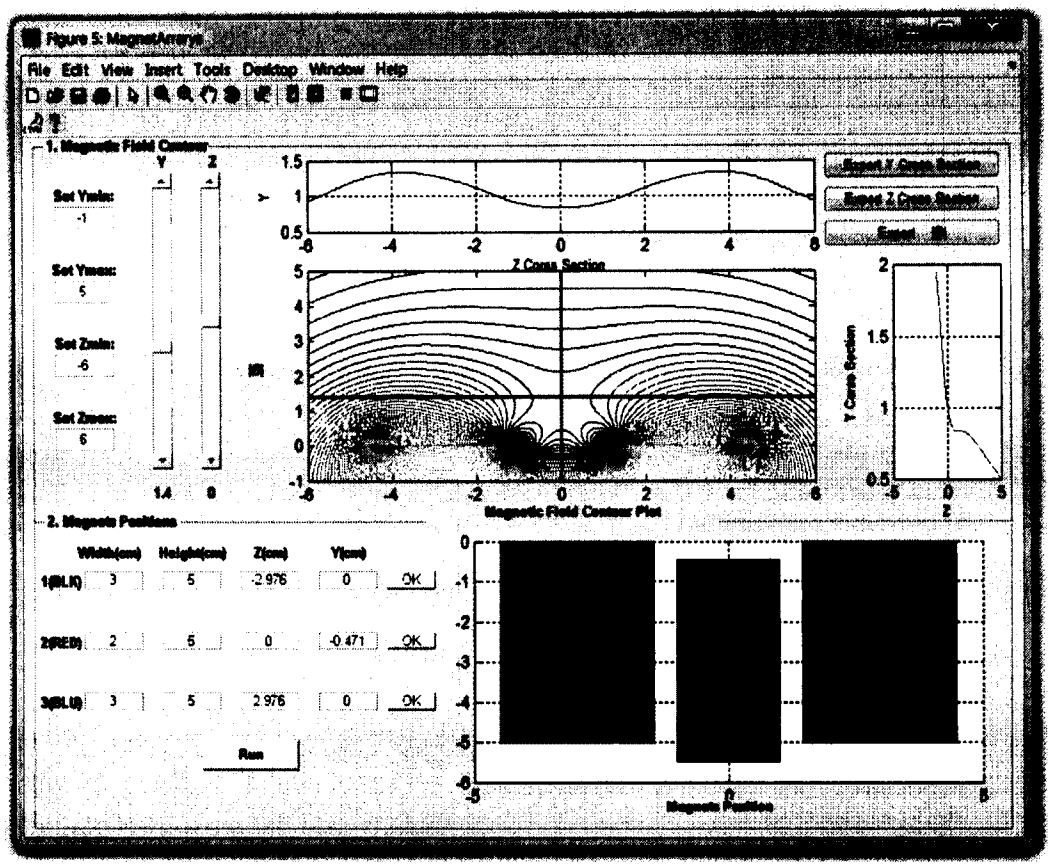

Figure 3.3. Graphical interface of the MATLAB function MagnetArrays.

The flexibility of MATLAB is even more important when blocks of different sizes are utilized. Purchasing component magnet blocks is difficult and time consuming. Therefore one usually purchases an inventory of magnet blocks from vendors in China for use over an extended time. The MATLAB function ArrayMaker, developed as a part of this thesis, calculates the distribution of magnetic field employing Eq. 3.1, for all of the possible combinations of the available blocks. It produces the best configuration for the desired result. Figure 3.4 shows the results of a simulation to produce arrays with the strongest possible static field from a set of magnet blocks. In this example two central blocks with widths of 2 and 4 cm and four sets of 2, 3, 4 and 5 cm for the external blocks

are available. All the blocks were considered of the same thickness t = 5 cm and the same length l = 10 cm. The result shows the 8 possible arrays with maximum B_o. Other parameters like position or width of the sensitive spot, weight and size of each array can also be evaluated. Additionally, the natural gradient (see Chapter 5) of the array is included, which is important for extended constant gradient designs. Any of these parameters can be set as a design goal during the simulation.

a

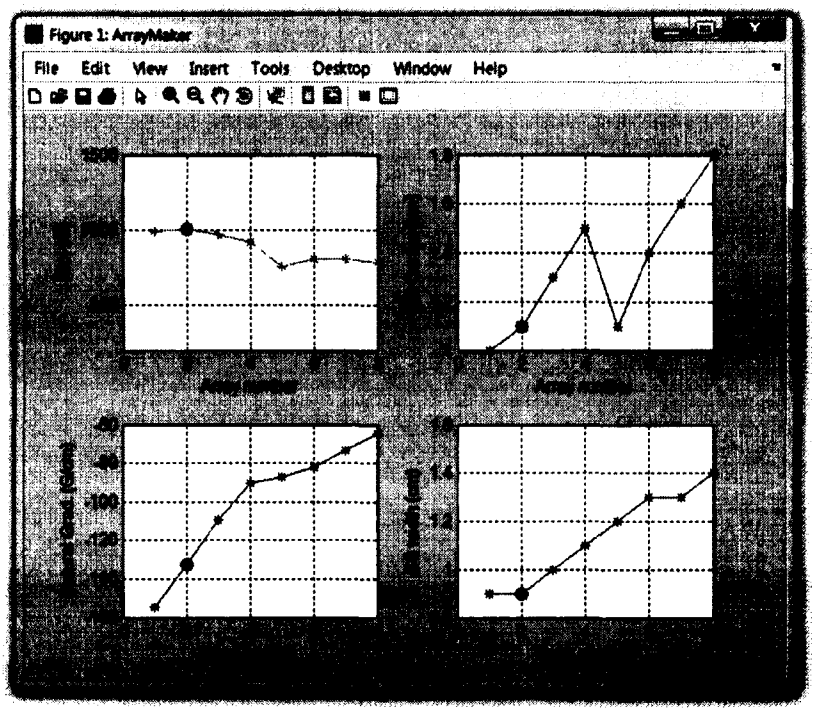

b

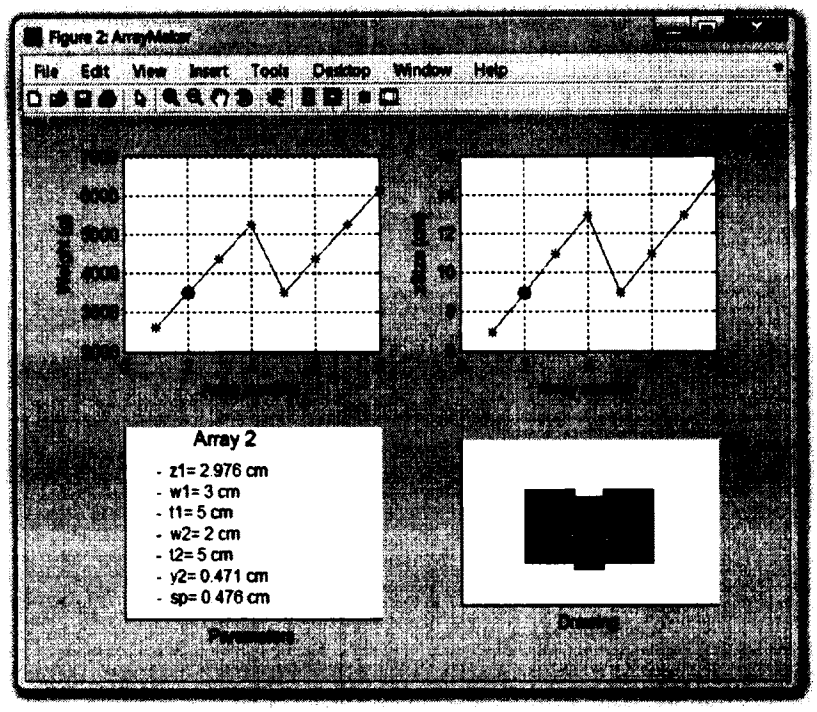

Figure 3.4. Result windows obtained from the MATLAB function Arraymaker. Each value in the abscissa of the graphics represent a different set of blocks while the ordinates are the characteristic (static field, position of the spot, etc.) for the optimum array. By clicking on each point of the curve, the spatial parameters of the optimum array are shown at the bottom left in (b). In this example the maximization of the static field was chosen as a selection criterion. Array number two, similar to the one presented in [1] was chosen to be built.

It should be noted that, because the MATLAB simulation is based on a 2D mathematical expression, the value of the magnetic field may be different than the one produced by the actual array. A more realistic value of the magnetic field can be obtained with a 3D simulation tool like Vector Fields.

As a general procedure, the basic design is undertaken employing MATLAB. Once the spatial parameters of the array are determined, Vector Fields software is employed for verification and fine adjustments. Usually, the magnetic field along the

central line is plotted to verify that the designed array produces the desired characteristics. Figure 3.5 shows a Vector Fields simulation of the three-magnet array with the blocks and parameters obtained from the MATLAB simulation.

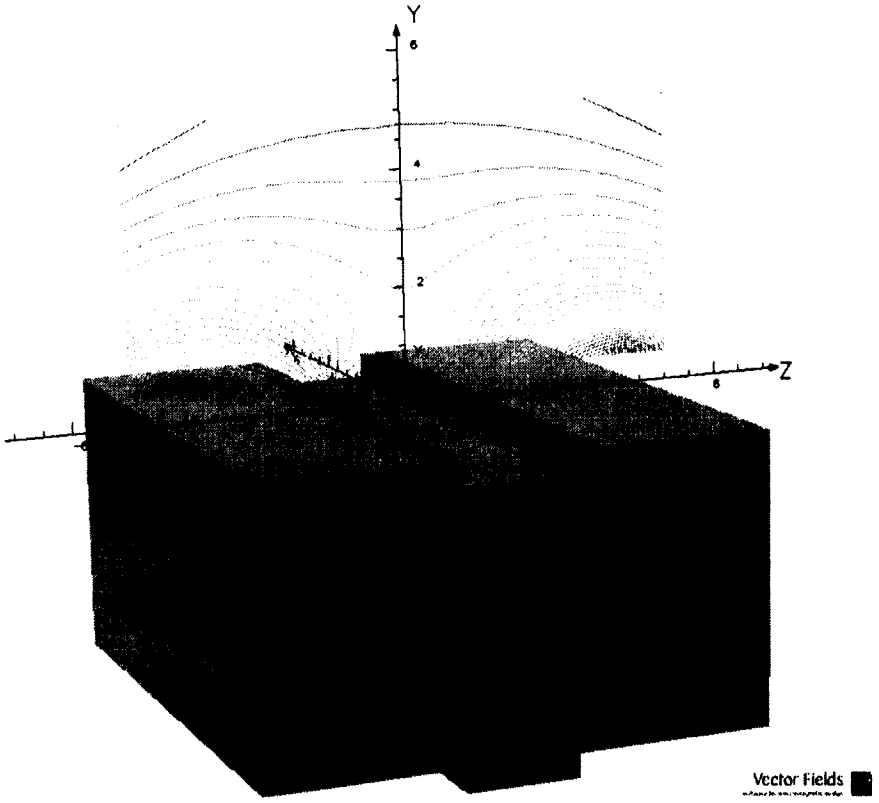

Figure 3.5. Three dimensional representation of the three-magnet array employing the professional software Vector Fields.

3.1.3 Construction of the array

The building process of the array can be subdivided into three stages. Special safety measures should be taken because of the strong force of attraction of the magnet blocks. These arrays are "safe" to construct because their construction does not involve magnet orientations with significant repulsive forces. This does not mean the process is "absolutely safe".

As a first stage, the magnetic field of each block is characterized independently. The magnet blocks were N48 NdFeB magnets supplied by Yuxiang Magnetic Materials Inc. Co. Ltd., Xiamen, China. All of the available blocks with the appropriate dimensions should be characterized by employing a three axis magnetic field probe (Lake Shore Cryotronics Inc., Westerville, USA) on a three axis plotter (Velmex Inc., Bloomfield, USA). The measurement should be taken 0.5 cm away from the surface of the blocks along their longitudinal axis. Figure 3.6 shows the result of this measurement for 5 different magnet blocks. All the blocks were placed with the magnetic field oriented in the same direction. Measurements were taken for two orientations of each block (bottom up and down) by rotating the magnet around its magnetic axis. We have found in practice the magnetic field distribution about the two faces will usually differ as shown below.

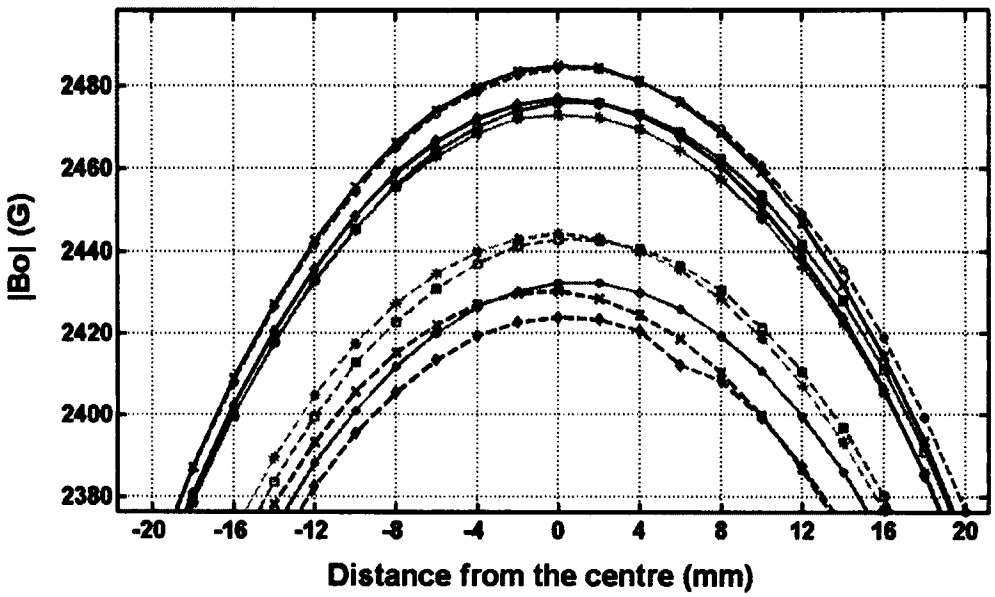

Figure 3.6. Magnetic field measured longitudinally above 5 magnet blocks. The magnetic field for each block is represented with a different marker and solid or dashed lines for the two possible positions. Solid × (magnet 4 bottom down) and dashed ○ (magnet 1 bottom up) are well matched and can be employed as external blocks.

Secondly, the blocks to be employed for the external blocks should be selected among those with a similar distribution of magnetic field. Practical measurements have shown a magnetic field variation of around 5% among blocks. Finally, for putting together the blocks, some special tools should be employed in order to avoid accidents. These tools should be made of a non-magnetic material, especially wood.

Figure 3.7 presents a photo of the array built employing the parameters previously mentioned and those obtained from the simulation in MATLAB and Vector Fields. In this case it was not necessary to introduce any ferromagnetic element for magnetic field correction, as described in [1], because of a better selection of the external blocks. The new three-magnet array is 11 cm long (along x in Fig. 3.7) and 10 cm wide with a height of 6.5 cm and mass of 3.5 kg.

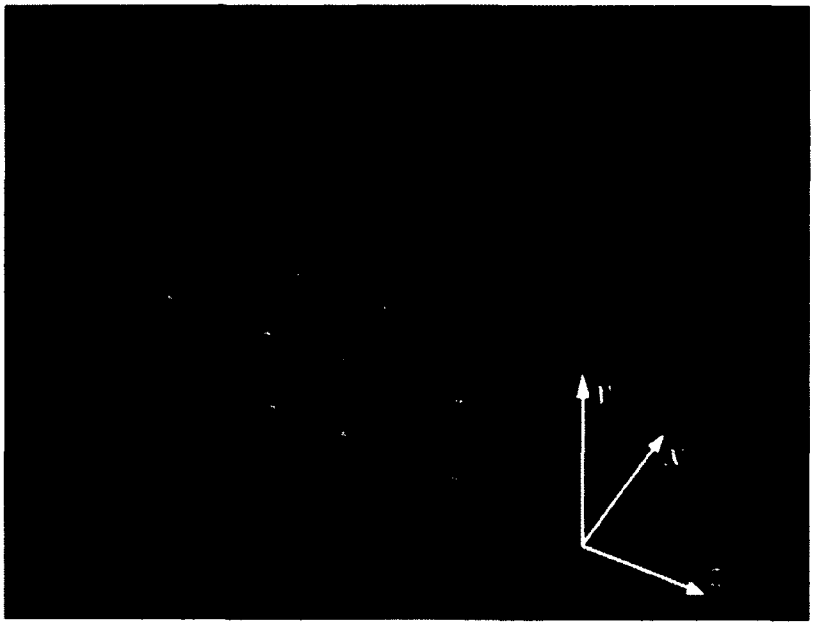

Figure 3.7. Three-magnet array designed with the parameters obtained from simulation.

3.1.4 Characterization

Once the array is built, it is characterized employing the same three axis magnetic field plotter mentioned in Section 3.1.3. This characterization involves the measurement of the magnetic field magnitude along the vertical central line (Fig. 3.8), for adjusting the position of the central block, and 2D magnetic field mapping (Fig. 3.9) of the central planes of the spot.

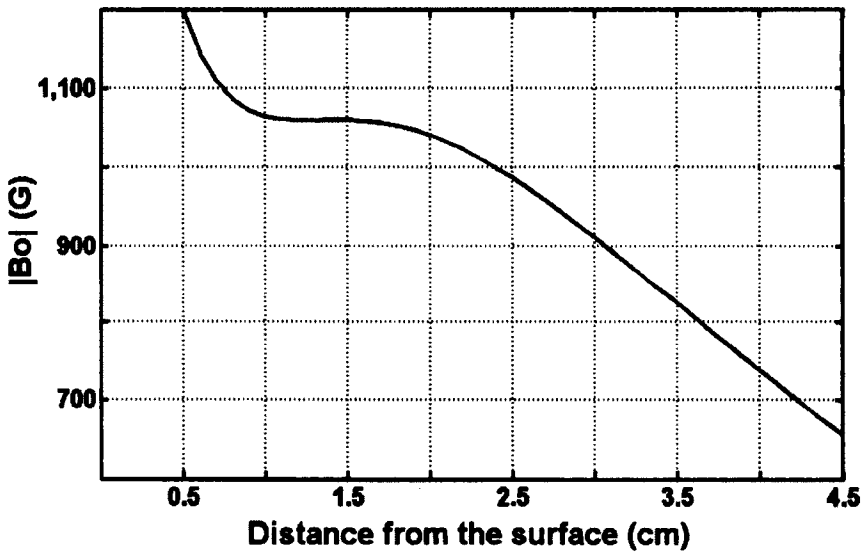

Figure 3.8. Magnetic field along the central vertical line of the array. The centre of the homogeneous spot is 1.3 cm from the surface of the magnet ($y = 0$).

a

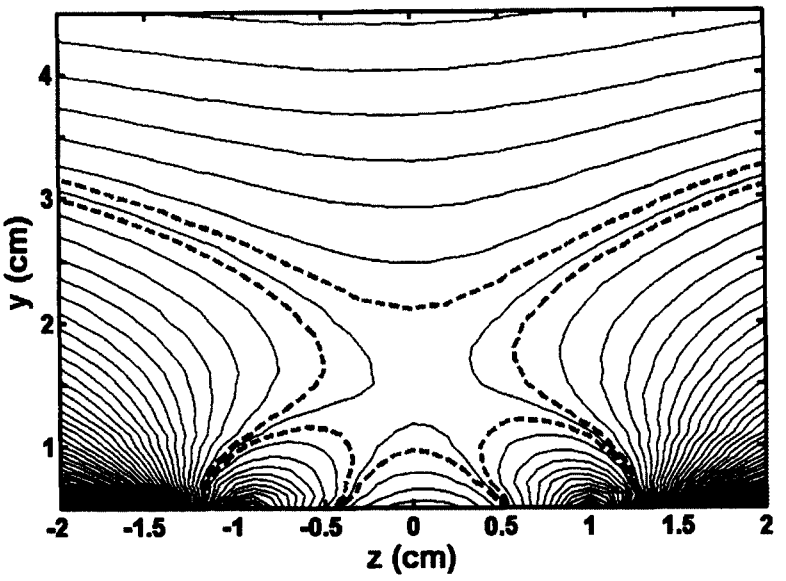

b

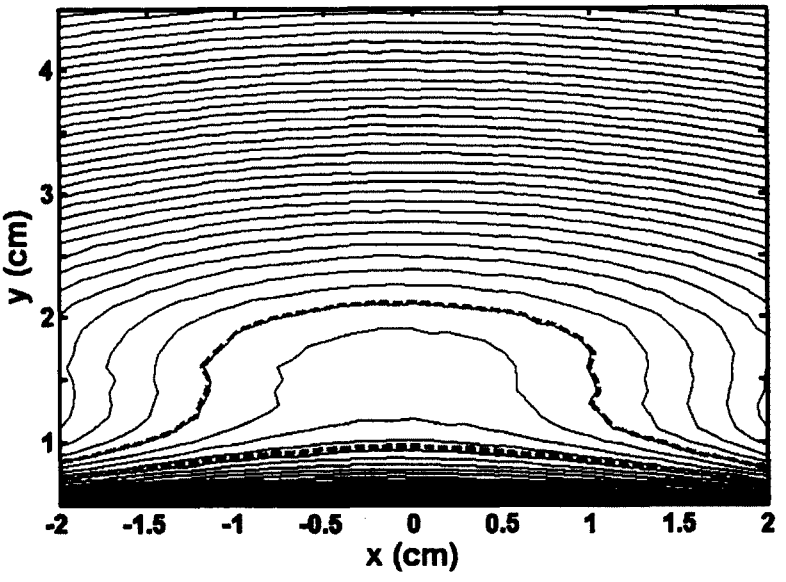

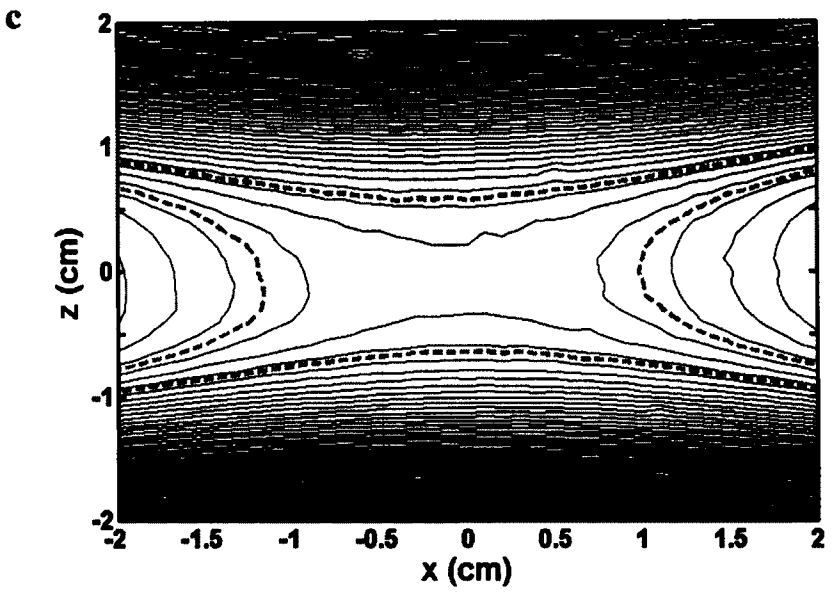

Figure 3.9. 2D map of the magnetic field over the three-magnet array. The axis system is illustrated in Fig. 3.7. Planes *yz* (a) and *xy* (b) are located at the centre of the magnet ($x = 0$ and $z = 0$ respectively). The *xz* plane (c) is located at the centre of the homogeneous spot (y = 1.3 cm). The dashed line represents the limits of the excitation bandwidth for a RF pulse of 5 μs.

For the extended constant gradient configuration (see Chapter 5) additional measurements should be taken in order to check the lateral homogeneity of the magnetic field distribution. In that case, measurements along horizontal lines in the x and z directions at different y positions are necessary. Additionally, measurements of the magnetic field along vertical lines spaced 0.5 cm from the centre in the x and z direction can be superposed with the measurement along the vertical central line in order to complete the representation.

Once the array is built and characterized, it is appropriate to run simple NMR measurements to set all the parameters required for more complex experiments. A simple spin-echo sequence can be employed to set the operation frequency and the RF power.

For designs employing a constant gradient a stimulated echo sequence combined with CPMG or CPMG with variable τ, and a sample with known coefficient diffusion D, can be employed to verify the value of the gradient.

3.2 Probes for the three-magnet array

The horizontal orientation of the magnetic field above the three-magnet array permits more sensitive probes for excitation and reception than those employed in magnets with vertical field. A simple loop (surface coil) can be employed as a probe in this case. For specific applications like core plug analysis, where the sample has a cylindrical shape, a solenoid can also be employed.

3.2.1 A solenoid as the probe for the three-magnet array

Even though the solenoid is uncommon in UMR, its employment could be beneficial taking into account the shape of the sample. In this case, in addition to the higher sensitivity, the B_1 homogeneity is also greatly improved. Two RF probe orientations are possible for the three-magnet array. The longitudinal axis of the solenoid can be oriented perpendicular to the magnet surface or parallel (x oriented in Fig. 3.7). This allows, in combination with an extended constant gradient, selection of transversal or longitudinal planes of the sample. For extended cylindrical samples the longitudinal axis of the probe is oriented along x (see Fig. 3.7), parallel to the magnet surface.

Even when the solenoid is encompassing the sample, it can be readily changed if required for different sample diameters. A set of solenoids can be more easily designed

for different diameters than a set of magnets with different bore sizes. It is also easy in practice to change the RF probe. Our prototypical samples for UMR with solenoidal RF probes are fluid saturated rock core plugs.

Parameter selection for designing a solenoid is straightforward. The diameter is determined by the diameter of the core plug (in our case 1.5", 2.5" and 3.5") and the length by the size of the sensitive spot in the x direction. The wire should not be longer than $\lambda/20$ and it is recommended to keep the coil impedance between 20 and 200 Ω [5].

Choosing the Q of the probe is more troublesome and therefore requires additional analysis. According to [6] the signal to noise ratio ψ in a NMR experiment is proportional to $\sqrt{Q}$ (see Eq. 3.2 from [6] and Eq. 3.3).

$$\psi_{rms} = KM_0\left[\left(\frac{\omega_0 L}{R}\right)\frac{\eta\mu_0 V_s}{8kT_c F\Delta f}\right]^{\frac{1}{2}} \tag{3.2}$$

$$Q = \frac{\omega_0 L}{R} \tag{3.3}$$

In UMR, the effective volume of the sample V_s is generally limited by the size of the homogeneous spot, which is determined by the field distribution and the excitation bandwidth. Increasing the Q of the probe produces a reduction in the size of the sensitive spot, and therefore, a decrease in $\sqrt{V_s}$. Even though it should be possible to find the Q value that maximizes ψ_{rms}, this is troublesome and time consuming. A simple comparison of the same coil with two different Q values is the best practical strategy as illustrated here.

The Q value is also important because it controls the probe dead time (DT). By increasing the Q, the dead time will increase in proportion (see Eq. 3.4 and Eq. 3.5 from [7]). This means that the minimum echo time will be longer and therefore the NMR signal will be more attenuated by T_2 and diffusion effects. It should also be noted that, even when the excitation bandwidth is narrowed, the effective magnetic field gradient through the sensitive spot remains the same.

$$\tau_r = 2\frac{Q}{\omega_0} \tag{3.4}$$

$$DT = 20\tau_r \tag{3.5}$$

It is not very useful to apply short duration RF pulses (broadband) when the Q of the probe is high. The pulse width should be set according to the Q. A higher Q means longer RF pulses and more relaxation during the excitation is possible. Longer pulses also make it more difficult to set the amplitude for the excitation [8].

Table 3.1 shows a comparison of the RF power applied and the signal obtained for the same probe with two different Q values. The fourth column contains the values of the attenuation for the 180° RF pulse, higher attenuation results in lower applied power. The signal intensity was measured at the peak of the 500 μs TE echo for the magnitude signal. The probe for this measurement was a solenoid of 1.5" diameter.

Table 3.1. Signal for the same probe with different Q values

Q value	DT (μs)	Pulse [illegible]	Attenuation (dB)	Signal [illegible]
21	60	10	14.5	203
70	200	30	29	188

Even when the echo time was maintained at 500μs for both measurements, the signal is higher for the lower Q probe. Therefore, the lower Q configuration (around 20) is usually the better choice in this magnet array for maximum signal.

3.2.2 A simple loop as a probe for the three-magnet array

The previous analysis for choosing the Q of the probe is also applicable for the surface coil. As for the solenoid, the impedance will be kept between 20 and 200 Ω. In this case the radius of the coil is the parameter to be analyzed. The details of excitation and reception in UMR should be analyzed in order to choose the optimum radius.

The majority of studies in the literature consider the sensitive region of a circular loop, along the axis perpendicular to the coil plane, to be limited to one radius [9, 10, 11]. This criterion does not seem to be applicable when the sensitive spot is limited to a small volume at a fixed distance from the surface of the magnet.

From a RF excitation point of view, the optimal radius of the RF probe can be found by finding the maximum of B_1 [2] with respect to the radius according to the position of the sensitive spot which is determined by the magnet array. For a loop in

open space, the optimum RF probe radius R_{opt} can be expressed as a function of the position of the centre of the sensitive spot y_{ss} employing Eq. 3.6 [12].

$$R_{opt} = \sqrt{2}\, y_{ss} \tag{3.6}$$

For the three-magnet array, the presence of a conductive surface underneath the coil introduces another complexity to the analysis. Image theory [13], which employs a virtual RF source to account for the reflections taking into account the boundary conditions, can be employed in a MATLAB simulation in order to calculate the magnetic field at different positions over the loop. Nevertheless, the irregular shape of the top surface of the three-magnet array makes the problem complex and more suitable for specialised simulation tools.

A practical measurement of B_1 over the coil can be undertaken by displacing the RF probe with respect to the measurement spot. Once the optimum RF pulse length for each position is found, Eq. 2.8 can be applied to calculate B_1.

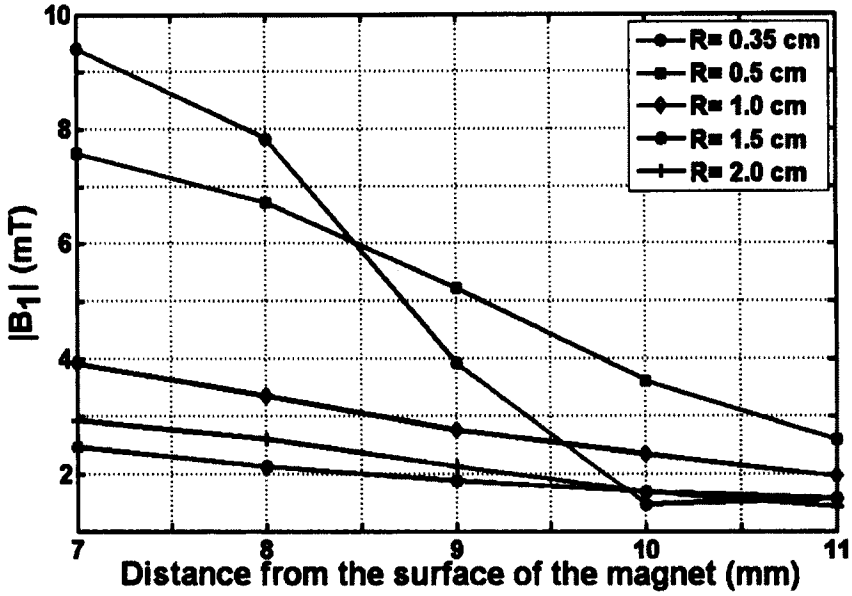

Figure 3.10. B_1 field for the 180° RF pulse, measured at different positions over surface coils of different radii (R).

For reception, the problem is even more complex and other factors should be taken into account. According to Eq. 3.7 from [6] the signal intensity is proportional to the intensity of B_1 (reciprocity principle) and V_s. Even though this formula is based on considering a reasonably homogeneous B_1 it should be good enough for our case.

$$\xi = K\omega_0(B_1)_{xy}M_0V_s\cos(\omega_0 t) \tag{3.7}$$

In UMR the effective volume of the sample V_s is generally limited by the size of the homogeneous spot, which is determined by the B_0 field distribution, the RF pulse excitation bandwidth and the Q of the probe. Nevertheless, if the radius of the coil is

smaller than the spot, it will determine the effective volume. For a circular loop, the sensitive region in planes parallel to the loop is defined by its diameter [5].

Because of the influence of the excitation bandwidth on the size of the spot, the maximum available RF power should be also included in the analysis. Low power requires longer RF pulses and therefore produces smaller spots. For our case, where the power limit is 250 W, pulses between 5 and 10 μs will be employed.

Figure 3.11 shows the variation of the product $B_1 V_s$ for different coil radii as a function of height above the magnet array. The results in Fig. 3.10 have been employed for this calculation. The sensitive spot was considered to be a square based prism with base in the yz plane and sides of 1 cm. The longitudinal axis of the prism is oriented along the x axis and is 2 cm long. This volume occupies most of the sensitive spot produced by a 10 μs RF pulse in the typical homogeneous spot three-magnet array considered here.

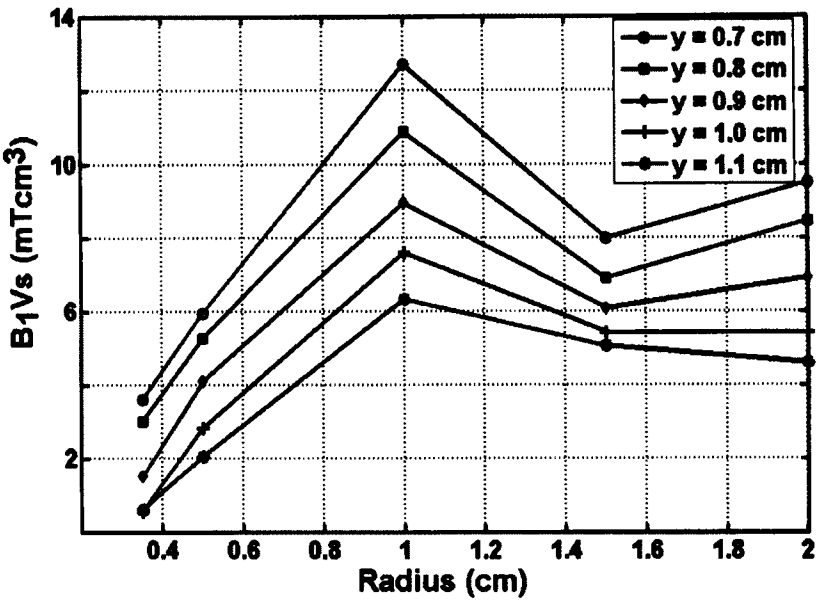

Figure 3.11. Variation of the product B_1V_s, which is proportional to the NMR signal. As a rule of thumb, to maximize the signal, the diameter of the coil should be similar to the larger dimension of the sensitive spot.

When the diameter of the coil exceeds the lateral extension of the sensitive spot the behavior of the curve produced by the product B_1V_s is dominated by B_1 but for small RF coils the amount of signal is more dependent on the volume that can be excited.

Table 3.2 summarizes the results of measuring the signal with four surface coils of different diameters employing the array BA11-4 (f_0=4.466 MHz, sensitive spot at 1.3 cm from the surface). The Q value was the same for all three probes (Q = 23). A simple spin-echo sequence was employed for the experiment. The echo time was maintained at 400 μs for all measurements. As stated before, attenuation values correspond to the 180° pulse. The 90° pulse was set at one half the voltage of the 180° pulse.

Table 3.2. Signal for loops of different radii

[illegible]	[illegible]	[illegible]
0.5	16.5	180
1	13.5	266
1.5	10.5	288
2	<10.5	-

The power required for the 180° pulse for the coils are consistent with the results of Fig. 3.10. For a distance of 1.1 cm from the surface, which is near the centre of the sensitive spot, the surface coil of 0.5 cm radius produces the stronger B_1 and therefore requires less power for the 90° and 180° RF pulses.

For reception, the best result was obtained with the 1.5 cm radius probe, which is larger than the optimum coil (r = 1 cm) from Fig. 3.11. Several factors explain the discrepancy. First of all, the size of the sensitive spot assumed for the simulation in Fig. 3.11 does not cover completely the real sensitive spot. As can be observed in Fig. 3.9, there are some regions of the spot that, because of their shape, were not included in the region covered by the prism employed to simulate the spot. The signal from these regions is received by the 1.5 cm radius probe but not by the 1 cm radius probe.

Another factor could be related to the homogeneity of the B_1 excitation along the *y* axis, which is homogenous over a larger region for probes with larger radii. The distribution of the B_0 magnetic field along the *y* direction in the sensitive spot could be an

additional factor affecting this result. As can be observed in Fig. 3.8, B_0 is not symmetric around the centre of the spot, where the first derivative is zeroed. The first part is smaller because of the stronger gradient. This means that, because the RF pulse has a symmetric spectrum, the geometric centre of the spot that can be excited is a bit further than 1.3 cm from the array surface, which benefits the 1.5 cm radius probe. It was impossible to find the maximum signal for the 2 cm radius coil because the RF power available was not sufficient. As a rule of thumb we believe that, because the coil is the same for excitation and reception, the diameter of the coil should be generally similar to the largest dimension of the spot. While this is a common sense rule, to the best of our knowledge no systematic analysis has been presented in the literature.

3.3 Limitations of the original design

The three-magnet array, as presented in [1], has many desirable features that make it well suited to UMR. Nevertheless, it has limitations that make its employment difficult in some applications. Four main problems must be solved in order to broaden the scope of applications:

1. The presence of electromagnetic waves, produced by the interaction between the RF field and the magnet, interferes with the signal acquisition when the probe is oriented along the x axis (see Fig. 3. 7). This problem makes difficult the utilization of more sensitive probes, like the solenoid, for rock core plug analysis or flow measurements.

2. The sensitive spot of the original design is centered 1 cm away from the magnet surface. For applications like rock core plug analysis it is critical to explore deeper layers inside the sample.
3. The finite length of the magnet in the x direction (see Fig. 3. 7) introduces a variation of magnetic field over the array along this axis. This effect reduces the size of the sensitive spot for homogeneous spot designs and affects the lateral homogeneity for the constant gradient design.
4. The absence of a constant gradient in its magnetic field distribution makes this approach inappropriate for diffusion or profile measurements, which are very important in magnetic resonance.

The fourth point and the design solution are discussed in depth in Chapter 5.

3.3.1 Acoustic ringing in the three-magnet array

Even though the solenoid RF probe is a natural solution for cylindrical core plugs with UMR, it is not very useful with the original design of [1]. Undesirable signals, produced by the interaction of the RF and static magnetic fields with the metallic structure of the magnet, interfere with the NMR signal. Figure 3.12 shows the result of a spin-echo measurement employing the original three-magnet array design. In this case, even when a shielding layer was placed on top of the magnet, the interference is clearly observed.

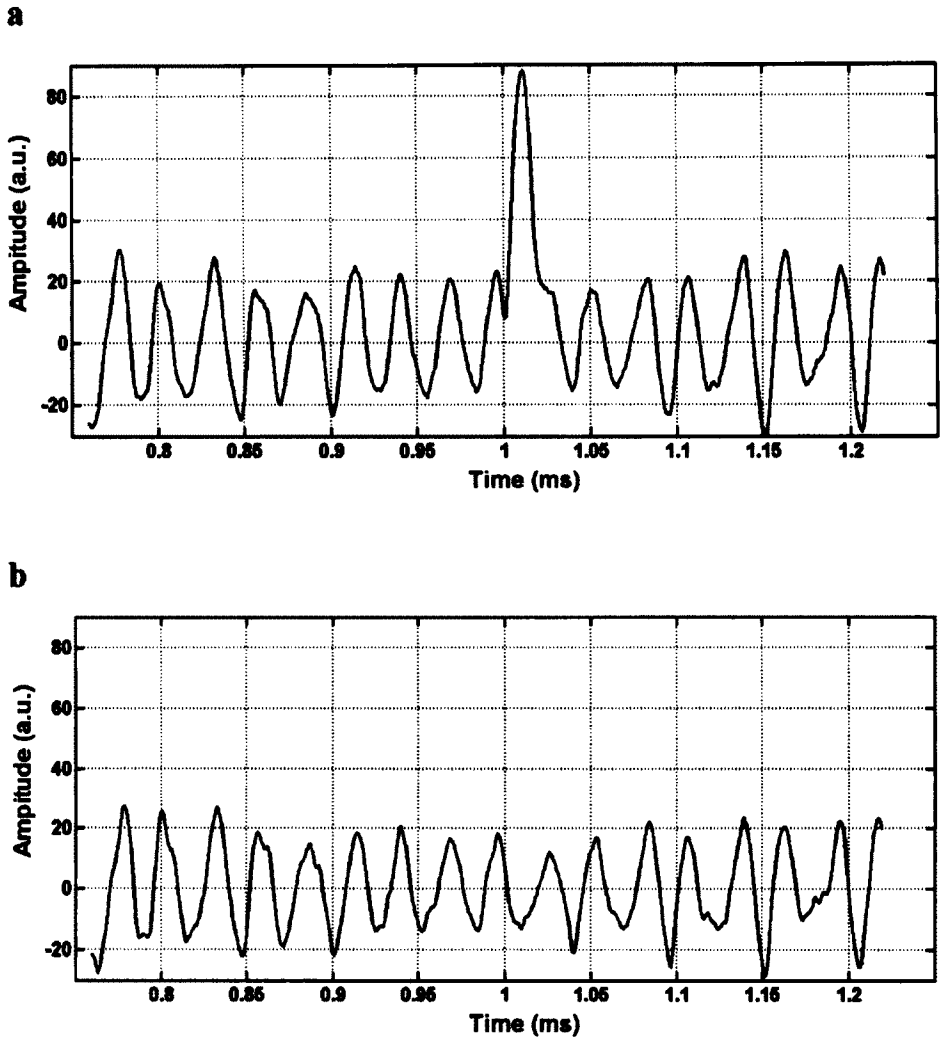

Figure 3.12. Acquisition during a spin-echo experiment employing a solenoid and the original design of the three-magnet array. The interference is superimposed with the NMR signal when the sample is present (a). In absence of the sample, the interference is clearly observed (b).

This effect, known as acoustic ringing, has been known for many years but a complete explanation was not presented until 1978 by Buess and Petersen [14] and Fukushima and Roeder [15]. The magnetic field of a RF wave can generate, in the presence of a static magnetic field, mechanical waves in any metallic surface which can then be converted to electromagnetic waves. In Fig. 3.13 the magnetic field (x directed)

of the RF excitation penetrates into the metal decaying significantly over one skin depth (δ). This magnetic field produces eddy currents (*j*) inside the metal with a *y* component perpendicular to B_0. Electrons, moving in the *y* direction, experience a Lorentz force in the *x* direction which results in creation of a mechanical wave along the direction of propagation of the electromagnetic wave.

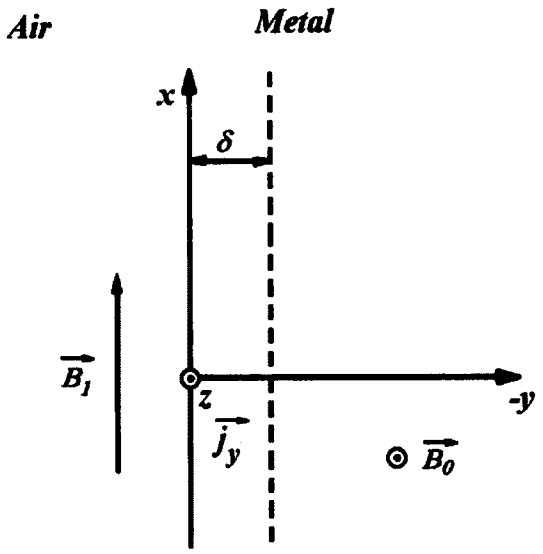

Figure 3.13. The interface between air and a metallic surface in the presence of static and RF fields yields acoustic ringing.

The inverse process is also known; the oscillatory movement of electrons in the *x* direction produced by the mechanical wave has an associated oscillatory electric field tangential to the surface, which means that it does not change when passing from the metal to the air. This wave is picked up again by the coil and added to the NMR signal as interference. A good review regarding this topic can be found in [16].

Different solutions to the acoustic ringing problem have been proposed in the literature [16]. Some involve the application of signal processing tools in the time and

frequency domains, others are focused on the pulse sequences while a third approach is oriented to technical aspects of the device. For the three-magnet array the solution has been focused on identifying the source of the interference and changing materials in the magnet array to make it less prone to acoustic ringing.

In order to find the source of the interference, all the parts of the metallic box of the magnet were disassembled and removed independently. The spacers, employed to separate the magnet blocks were found to be the main source of acoustic ringing. New spacers of fibreglass were employed. Figure 3.14 shows the signal acquisition with the new spacers. The interference problem is eliminated. This new version of the three-magnet array has been employed in combination with a solenoid for rock core plug analysis as discussed in Chapter 5 and Chapter 6.

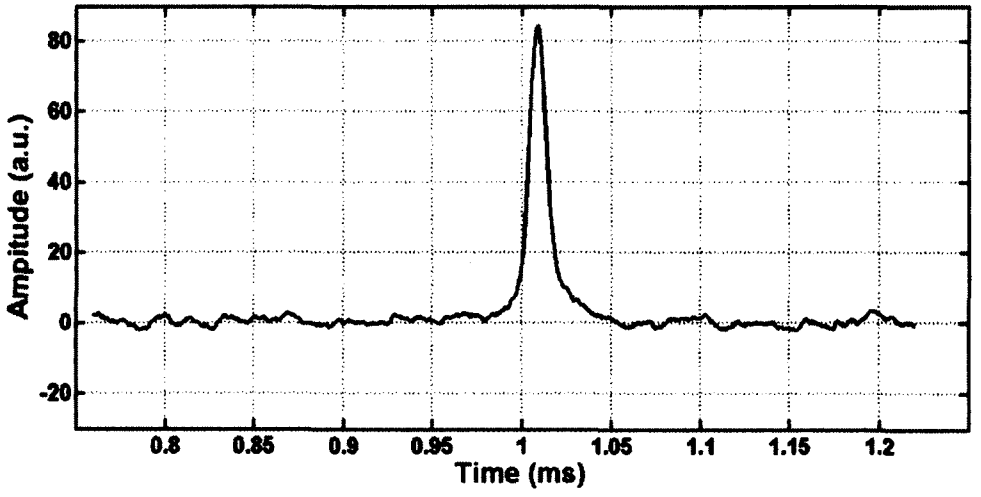

Figure 3.14. Spin-echo acquisition employing the new version of the three-magnet array with fibreglass spacers.

3.3.2 Three-magnet array with sensitive spot further away from the surface

The original three-magnet array described in [1] has the centre of the sensitive spot displaced 1 cm from its surface. With the addition of the probe; which includes the surface coil, the tuning circuit and the holder plate, 6 mm remains as the useful vertical displacement for the measurement. For experiments, such as core plug analysis, the surface of the sample can be damaged by the cutting tools. Therefore, it is recommended to carry out the measurement between 1.0 cm and 2.5 cm inside the sample. This means that it is necessary to produce sensitive spots farther than 1.5 cm from the surface of the three-magnet array in order to obtain reliable measurements.

For the three-magnet array, the depth of the homogeneous spot principally depends on the separation between the external blocks. Increasing this separation displaces the spot away from the surface but also decreases the magnetic field strength in the sensitive spot. This reduction can be somewhat compensated by increasing the width of the blocks. Figure 3.15 shows the magnetic field distribution of a three-magnet array designed for rock core plug analysis employing this idea.

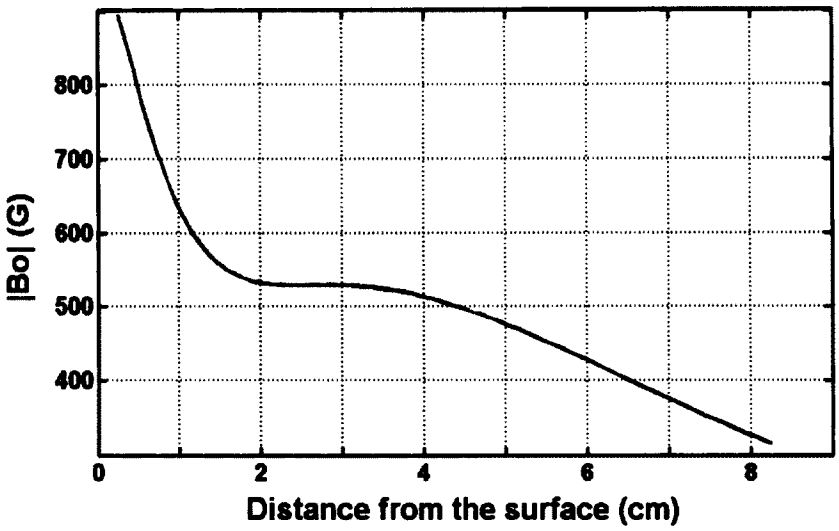

Figure 3.15. Magnetic field measured along the vertical line at the centre of the magnet array. The Larmor frequency at the centre of the spot is 2.25 MHz.

The centre of the homogeneous spot is 26.5 mm from the surface. The magnetic field at the centre of the spot is 530 G which corresponds to a Larmor frequency of 2.25 MHz. In this case the array was built by doubling the number of blocks of the original array. For each block of the new array two magnet blocks of the same size as the design described in Section 3.1 were employed. The new array is 18 x 11 x 6.5 cm. Figure 3.16 shows a photo of this version of the array.

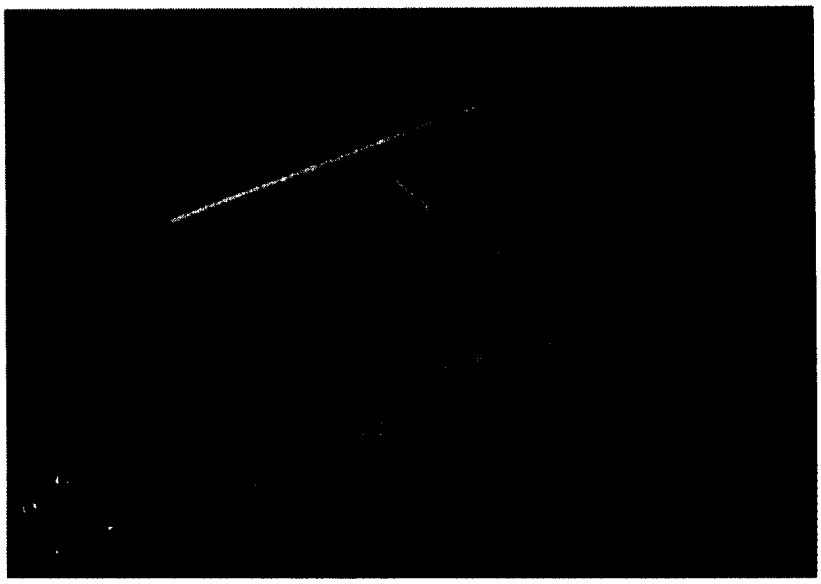

Figure 3.16. Three-magnet array designed for core plug analysis.

3.3.3 End effect in the three-magnet array

The finite length of the three-magnet array in the x direction (see Fig. 3.7) introduces a variation of the magnetic field along this axis. This phenomenon is known as an end effect. Figure 3.17 shows this variation along the x axis for different heights over the magnet. The first curve was measured at 0.4 cm from the surface and the last one at 3 cm. The separation, along the y axis (see Fig. 3.7), between successive measurement lines is 0.2 cm. The concentration of lines around the centre is caused by the presence of the homogeneous spot in that region. The typical bandwidth of the excitation for a homogeneous spot three-magnet array configuration is around 150 kHz, which corresponds to a variation of magnetic field of 35 G. This means that the end effect limits the homogeneous spot to a distance of 2.6 cm in the x direction (see Fig. 3.16).

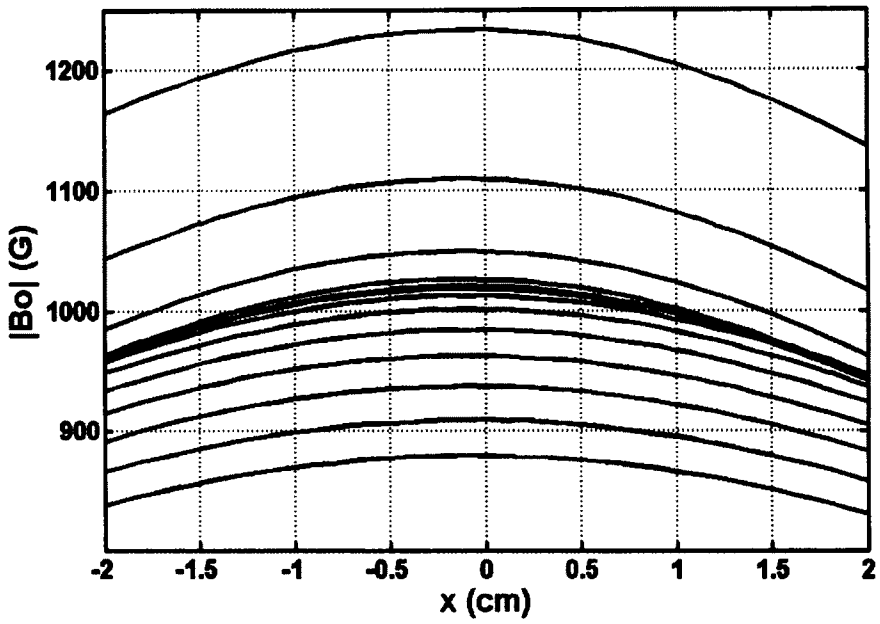

Figure 3.17. Magnetic field measured along the *x* axis. Each curve corresponds to a different height in the *y* direction. The first curve was measured at 0.4 cm from the surface and the last one at 3 cm. The separation between successive measurement lines is 0.2 cm. The curvature of the plots is a result of the end effect in the *x* direction.

A simple solution for this problem was presented by Perlo et al. [17]. By splitting the magnet and separating the new blocks by a proper distance, it was possible to compensate for the end effect. This solution allows creation of a flat plane of magnetic field, parallel to the surface that is suitable for high resolution profiles.

For the three-magnet array it is complicated to apply the solution of Perlo [17]. The adjusting process of the split array would be troublesome because of the central block, which should be displaced for creating the desired magnetic field distribution. Nevertheless, a similar solution could be implemented by changing the material of the spacers employed to separate the magnets. The current spacers are made of non magnetic materials and therefore have no influence on the field distribution. Using a ferromagnetic

material for this function would increase the overall field produced by the array. Because the spacers are fixed in the structure of the box, they can be split in order to obtain a similar effect to that of Perlo [17].

Figure 3.18 shows a drawing of this idea obtained from Vector Fields simulation. The dimensions of the spacers for the desired field distribution (flat at the center of spot), were found by simulation. Each part of the split spacer has a length of 1.5 cm with a gap of 7 cm between them. The width (4.76 mm) and thickness (5 cm) are the same as in the previous design. With these dimensions, the Vector Fields simulation shows that it is possible to obtain a flat magnetic field distribution in the x direction around the center of the array. The flat region is 4 cm long and is located at 1.3 cm from the surface of the magnet according to simulation, which coincides with the center of the homogeneous spot.

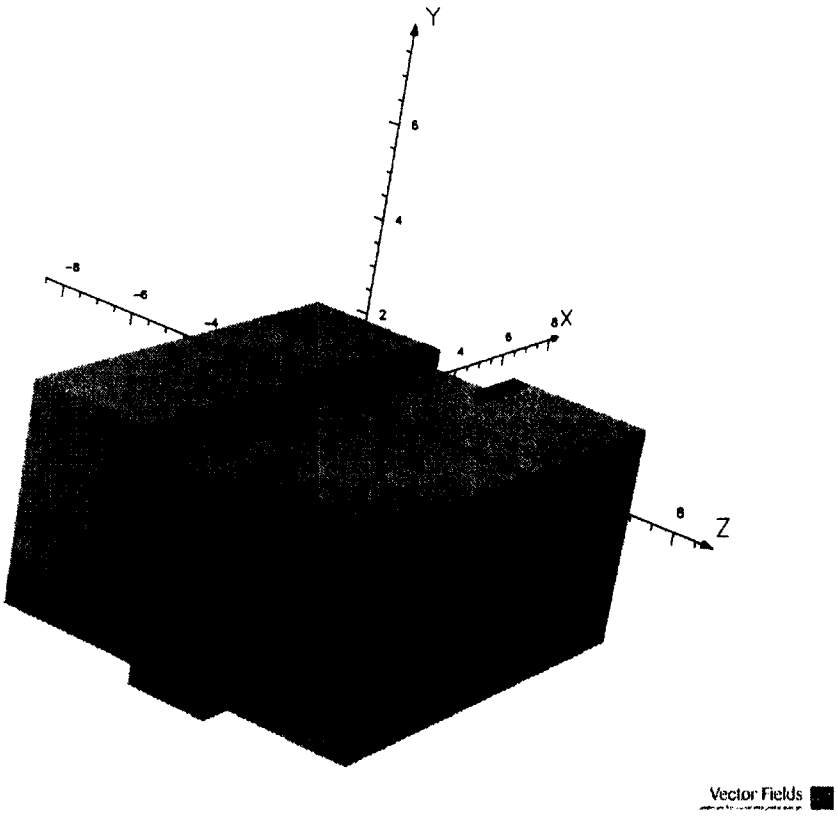

Figure 3.18. Three-magnet array with split ferromagnetic spacers. The spacers, placed between the external and the central block, have been represented by a different gray tone. Each part of the new spacers has a width in x of 1.5 cm with a gap of 7 cm between them.

Spacers were fabricated from regular ASTM A36 steel strips. Figure 3.19 presents the result of a magnetic field measurement over the array with the new spacers. As in the previous measurement with non magnetic spacers, the magnetic field was measured along horizontal lines in the x direction (see Fig. 3.7) as a function of height. Fourteen measurements were carried out at different heights over the magnet. The first measurement was taken at 0.4 cm and the last one at 3 cm. The separation between horizontal lines was 0.2 cm.

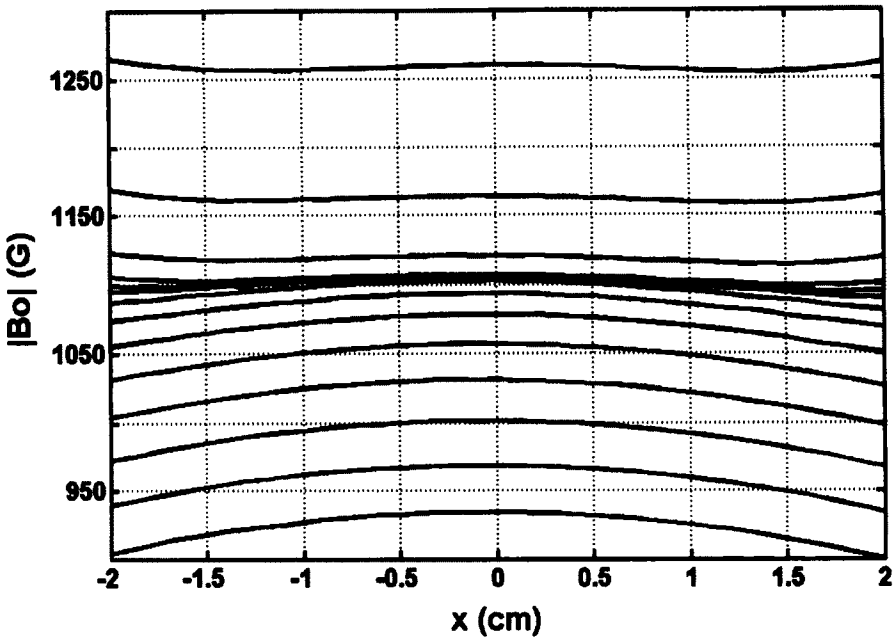

Figure 3.19. Magnetic field measured along horizontal lines over the three-magnet array with ferromagnetic spacers. The first measurement was taken at 0.4 cm and the last one at 3 cm. The separation between horizontal lines was 0.2 cm. The concentration of lines around the center corresponds to the homogeneous spot.

The variation of the magnetic field from the center to the extremities is now close to 10 G, which correspond to a bandwidth narrower than 45 kHz. This means that the new sensitive spot is larger than 4 cm in the x direction which is a great improvement compared to the previous result with the previous spacers (2.6 cm for 150 kHz of bandwidth). As an additional benefit, the overall magnetic field has been increased approximately by 10 % from 1022 G to 1105 G with the ferromagnetic spacers.

Figure 3.20 shows the echo signals obtained during a spin-echo experiment employing the same array with fibreglass and ferromagnetic spacers. The parameters for both measurements were the same. It was necessary to retune the probe from 4.35 MHz with the fibreglass to 4.72 MHz with the ferromagnetic spacers. There is an appreciable

increase in signal for the ferromagnetic spacers because of the increase in size of the sensitive spot.

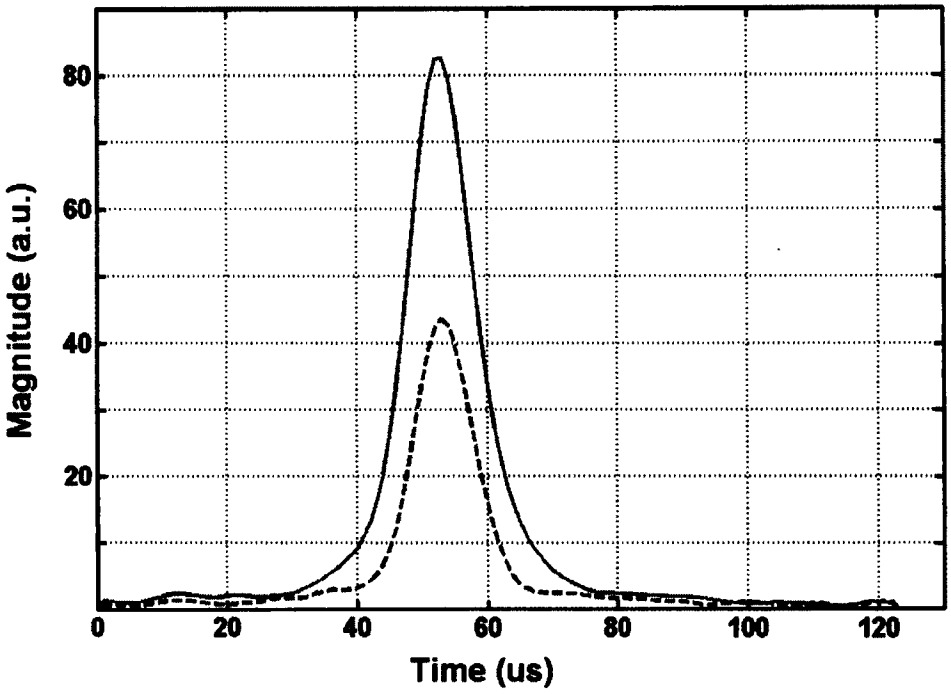

Figure 3.20. Echo signals acquired with the three-magnet array with fibreglass (dashed) and ferromagnetic (solid) spacers.

An important factor to be observed with the ferromagnetic spacers is the possible reintroduction of acoustic ringing. Characteristics of the metal like resistivity, density and skin depth have a strong influence on the amplitude of the acoustic wave. They are included in what is known as the conversion efficiency of a RF wave to acoustic ringing [16]. For steel the conversion efficiency is 14 times less than for aluminum [16]. Therefore, ferromagnetic spacers are not expected to reintroduce significant acoustic ringing. In addition, because of the presence of a gap between the split spacers, the conductive components are further away from the probe, which reduces the possibility of

producing acoustic ringing. As can be observed in Fig. 3.20 there is no visible interference during the acquisition.

While this chapter is strongly related to the homogeneous spot three-magnet array designs, it should be noted that the ferromagnetic spacer idea is also applicable to the extended gradient design (Chapter 5). In this case, a similar magnet design was employed with ferromagnetic spacers of different sizes. Each spacer was 3 cm in width with a gap of 4 cm between them. Figure 3.21 shows the field plot for this case. Measurements along 14 horizontal lines were carried out. The first line was 1.25 cm from the surface and the last one at 3.85 cm. The separation between lines was 0.2 cm.

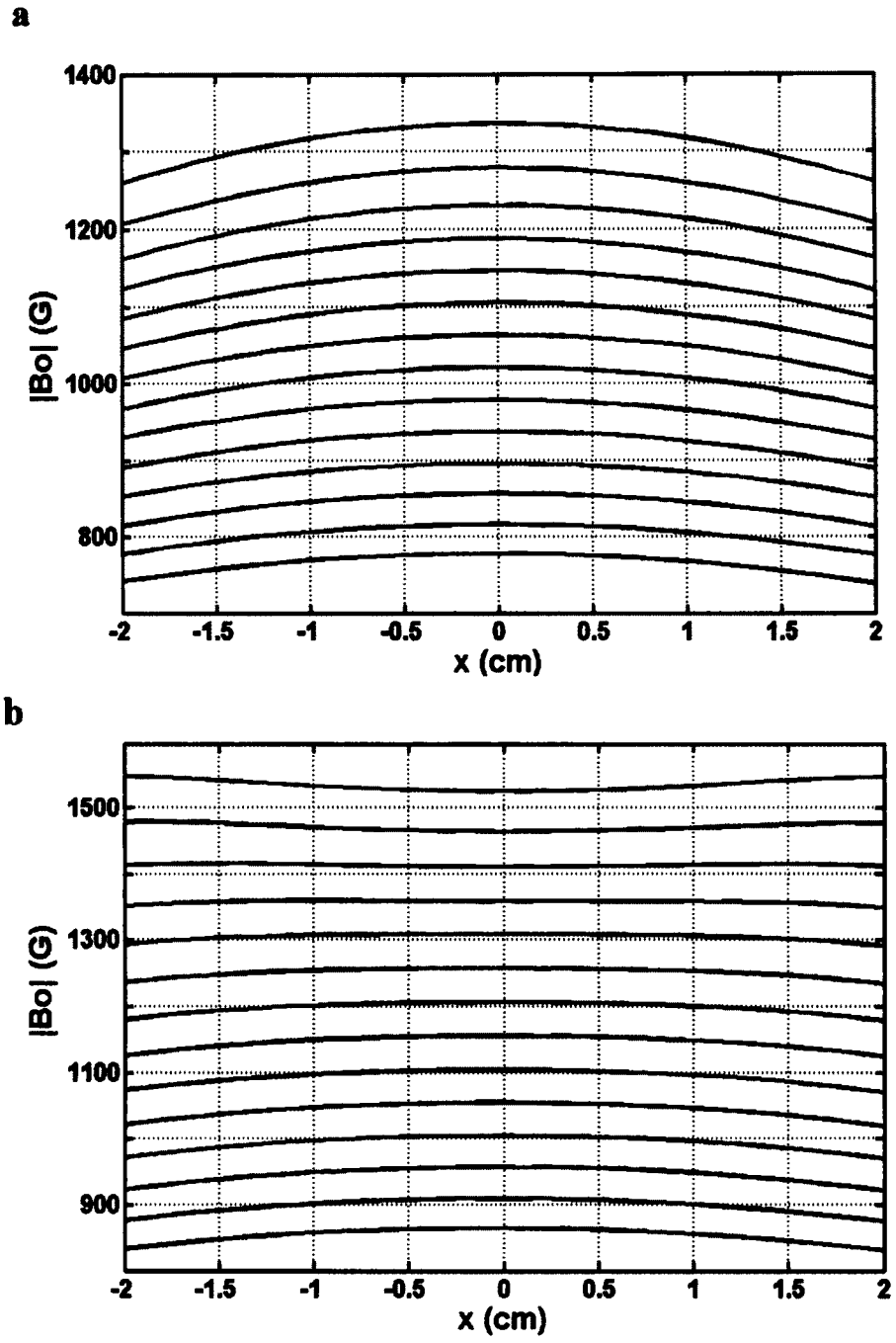

Figure 3.21. Magnetic field measured along horizontal lines over the three-magnet array for extended constant gradient configuration employing non magnetic (a) and ferromagnetic (b) spacers. The first line was at 1.25 cm from the surface (y) and the last one at 3.85 cm. The separation between lines was 0.2 cm. Each curve corresponds to a measurement along a horizontal line in the x direction.

As can be observed, the lateral homogeneity is greatly improved with the ferromagnetic spacers, especially in the region around x = 2 cm. The overall magnetic field has been increased from 1169 G to 1333 G (at x = 2 cm) and the constant gradient has increased from 209 G/cm to 254 G/cm.

3.4 Three-magnet array for handheld applications

Because the magnet blocks in a three-magnet array have the magnetic field orientated in the same direction, and no additional mechanical devices are required, it is possible to generate very compact designs employing this approach. This advantage makes it possible to build handheld systems. Figure 3.22 shows a photo of a handheld three-magnet array.

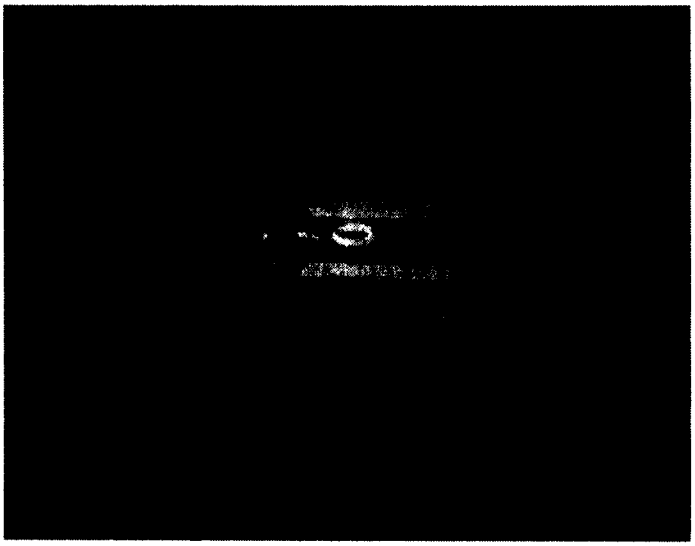

Figure 3.22. Three-magnet array designed for handheld systems.

Figure 3.23 shows the magnetic field distribution along the vertical central line of the array. The B_0 at the centre of the sensitive spot (1 cm away from the surface) is 763 G which correspond to a frequency of 3.25 MHz.

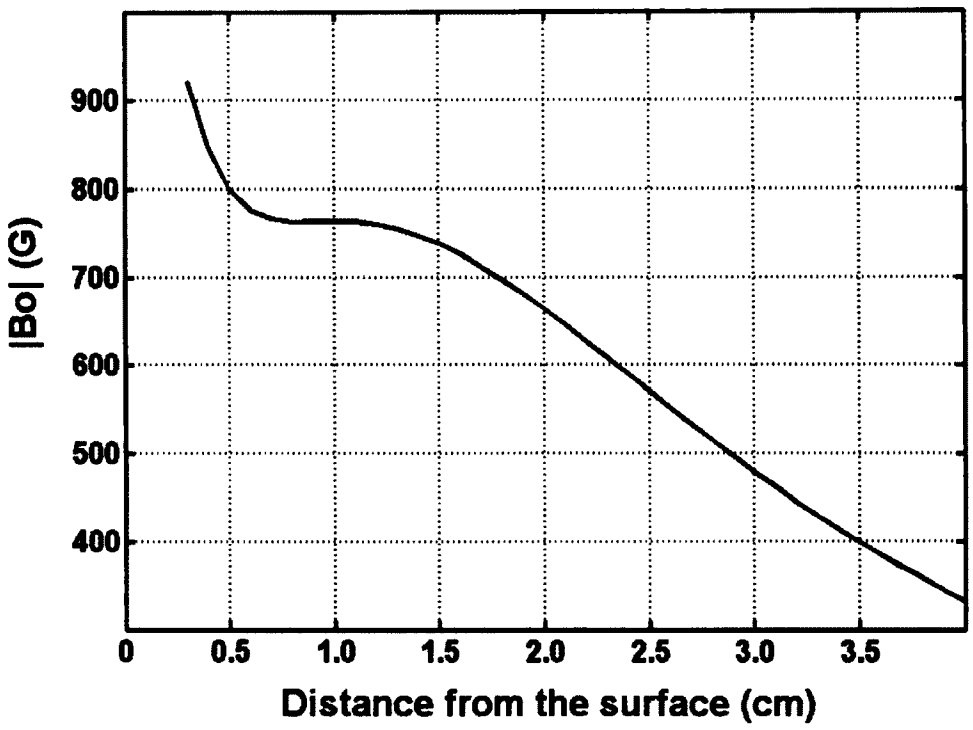

Figure 3.23. Static magnetic field distribution along the vertical central line of the handheld array SA1. The magnetic field is 763 G at the centre of the homogenous spot which is displaced 1 cm from the surface.

The handheld three-magnet array (SA1) has been built employing NdFeB magnets of 1.8 x 3 x 6 cm for the external blocks and 1.2 x 3 x 6 cm for the central block. Table 3.3 shows a summary of some features of this array in comparison with the original design proposed in [1].

Table 3.3. Features of the handheld array (SA1) and the original design (BA1)

Parameter	BA1	SA1
Static magnetic field (Bo)	1090 G	763 G
Resonance frequency (fo)	4.6 MHz	3.25 MHz
Sensitive spot (5% of Bo)	0.9 x 0.7 x 3.2 = 2 cm^3	0.7 x 0.7 x 1.6 = 0.784 cm^3
Signal amplitude in Minispec	100 %	60 %
Array size	10.2 x 8.3 x 10.7 cm	6.4 x 4.1 x 7 cm
Array weight	3.81 kg	0.96 kg
Position of the sensitive spot (from the surface)	1.3 cm	1 cm

The small array is 25% of the mass of the original design but still yields 60% of the signal. The nonlinear variation of the magnetic field with the size of the magnets proves that, even when the new blocks are smaller than those in the original design, the reduction in sensitivity is much less than the reduction in volume. The reduction in size of the sensitive spot is more critical in the x direction (see Fig. 3.7) because of the stronger end effect in this direction. Better results would be obtained by including ferromagnetic spacers in this design. The centre of the sensitive spot is closer to the surface in the handheld magnet because of the smaller separation between the external blocks.

References

[1] A. E. Marble, I. V. Mastikhin, B. G. Colpitts, B. J. Balcom, A compact permanent magnet array with a remote homogeneous field. J. Magn. Reson. 186, 100–104, 2007.

[2] U. S. Inan, A. S. Inan, Engineering electromagnetics, Addison-Wesley, California, USA, 1999.

[3] Vector Fields software for electromagnetic design, Opera version 10.511,Vector Fields Ltd. Oxford, UK.

[4] C. Wang, Magnet Array User's Manual, MRI Centre, University of New Brunswick, 2007.

[5] J. Mispelter, M. Lupu, A. Briguet, NMR probeheads for biophysical and biomedical experiment, Imperial College Press, London, 2006.

[6] D.I. Hoult, R.E. Richards, The signal to noise ratio of the nuclear magnetic resonance experiment, J. Mag. Reson. 24, 71-85, 1976.

[7] E. R. Andrew, K. Jurga, NMR probe with short recovery time. J. Mag. Reson. 73, 268-276, 1986.

[8] E. W Randall, T. G. Nunes, G. Guillot, P. R. Bodart, T_1-weighting of echo-trains in the stray-field for deuterium: prospects for imaging using long echo-train summation, Solid State Nucl. Magn. Reson. 14, 165-72,1999.

[9] A. Haase, F. Odoj, M. V. Kienlin, J. Warnking, F. Fidler, A. Weisser, M. Nittka, E. Rommel, T. Lanz, B. Kalusche, M. Griswold, NMR Probeheads for in Vivo Applications, Concepts Magn. Reson. Vol. 12(6), 361-388, 2000.

[10] B. Blumich, NMR imaging of materials, Oxford University Press, Oxford, 2000.

[11] M. Dias, J. Hadgraft, P. M. Glover and P. J. Mcdonald, Stray field magnetic resonance imaging: a preliminary study of skin hydration. J. Phys. D: Appl. Phys. 36, 364-368, 2003.

[12] C. N. Chen, D. I. Hoult, Biomedical magnetic resonance technology, Adam Hilger, Bristol and NY, 1989.

[13] C. A. Balanis, Antenna theory, analysis and design, Wiley-Interscience, New Jersey, USA, 2005.

[14] M. L. Buess, G. L. Petersen, Acoustic ringing effects in pulsed nuclear magnetic resonance probes, Rev. Sci. Instrum. 49. 1151-1155, 1978.

[15] E. Fukushima, S. B. W. Roeder, Spurious ringing in pulsed NMR, J. Magn. Reson. 33, 199, 1979.

[16] I. P. Gerothanassis, Methods of avoiding the effects of acoustic ringing in pulsed Fourier transform nuclear magnetic resonance spectroscopy. Prog. Nucl. Mag. Res. 19, 267-329, 1987.

[17] J. Perlo, F. Casanova, B. Blumich, Profiles with microscopic resolution by single-sided NMR, J. Magn. Reson. 176, 64-70, 2005.

Chapter 4

Real-time cure monitoring of an epoxy/ polyamidoamine system with unilateral magnetic resonance

This chapter is largely based on the paper "Real-time cure monitoring of an epoxy/polyamidoamine system with unilateral magnetic resonance", published in NDT&E International vol. 44, 2011, 329 - 34 [1]. It describes a practical application of the homogeneous spot three-magnet array for monitoring the curing process of an epoxy/ polyamidoamine system. The three-magnet array with uniform spot employed in this work does not feature ferromagnetic spacers.

The format of references in this chapter follows that of the original paper.

4.1 Introduction

Epoxy resins are frequently employed as the matrix holding and protecting the fibers in structural composite materials, which are utilized in an increasing number of applications in high technology industries (aerospace, automobile, wind

turbines, etc.). The manufacturing of structural components with composites is complex because there are a number of process variables involved that have the potential to adversely affect the end product quality. In typical structural component fabrication, the fibers are impregnated with the resin/curing agent mix and the fabricated part is placed in an autoclave/oven for curing. During the cure, the epoxy goes through various stages and the process variables (temperature, pressure, vacuum) must be controlled in order to achieve the best component quality. Since the mechanical properties of the end product depend on precise control of the process variables, there is benefit in developing a technique for real-time cure monitoring that will function in a real industrial environment. Such a technique could also serve as a quality control tool to verify that a fabricated component has cured uniformly over its entire surface.

Several methods have been investigated for cure monitoring of epoxy resins, i.e. dielectric permittivity measurements [2, 3], ultrasonic wave propagation [3, 4, 5], differential scanning calorimetry [6], dynamic mechanical analysis [4], and conventional pulsed magnetic resonance [3, 5]. In particular, magnetic resonance (MR) techniques reveal valuable information on molecular chain mobility, which is directly related to cross-linking within a polymer [7, 8, 9]. Unfortunately, all of the above methods are either laboratory methods that require sophisticated equipment and specialized technicians and/or methods that apply to a sample rather than the real part, which makes them inadequate for nondestructive and nonintrusive monitoring in a manufacturing setting.

However, since the 1980s, MR systems have been adapted into transportable unilateral probes due, in large part, to pioneer work at the Southwest Research Institute (San Antonio, TX). An excellent review of the development of unilateral NMR is found in [10]. The main advantage of these probes is that they allow scans with access from one side only, removing size and shape limitations from the object under investigation. The notion of portability was reinforced with the design of the first truly portable instrument [11]. Since then, a multitude of applications have emerged in various fields such as food, biomedical, polymer, porous media, etc. [10].

The present paper demonstrates the potential of using unilateral MR to monitor in real-time the cure of a thermoset resin by following the signal from an epoxy resin/polyamidoamine curing agent system. In the present context, the main advantage of this method is that it provides quasi-instantaneous information on the part being cured non-intrusively and without disturbing the curing process. When in position for a measurement, the probe's sensitive volume extends a short distance below the surface of the interrogated object, which makes it ideal for composite (thin shell form) applications.

4.2 Magnetic Resonance

MR results from the polarization of nuclear magnetic moments by a static magnetic field (B_o), which creates a net magnetization M_o oriented in the B_o direction. When the magnetic moments are excited by a radio-frequency (RF) pulse

(B_1) applied at right angles to B_o and at the Larmor frequency (defined below), M_o rotates about B_1 through an angle θ given by [12]

$$\theta = \gamma B_1 t_{rf} \tag{4.1}$$

where γ is the gyromagnetic ratio of the nuclei and t_{rf} is the pulse duration. Usually, t_{rf} is selected to cause a 90° rotation in M_o in order to maximize the MR signal. When perturbed from equilibrium, M_o precesses about B_o at the Larmor frequency [12].

$$\omega_o = \gamma B_o \,. \tag{4.2}$$

Precession of the sample magnetization induces a signal in the RF probe functioning as a pick up coil.

The system returns to its equilibrium state exponentially at a rate characterized by the spin-lattice relaxation time constant T_1. The observable MR signal disappears at a faster rate, characterized by the spin-spin relaxation time constant T_2, due to a loss of phase coherence among the interacting magnetic moments. In a realistic MR experiment, the signal lifetime decay constant is shorter than T_2 due to inhomogeneities in B_o, which accelerate phase decohesion. The signal lifetime is characterized by time constant T_2^*.

In a free-induction decay (FID) experiment, the amplitude of the signal detected after application of a 90° RF pulse is [13]

$$S(t) = M_o \exp\left(\frac{-t}{T_2^*}\right) \tag{4.3}$$

where M_o is the magnitude of the magnetization vector, t is the time elapsed after the application of the 90° RF pulse and T_2^* is the effective spin-spin relaxation time constant.

In a highly inhomogeneous B_o, the MR signal may be too short-lived to be measured by a FID experiment because of the receiver dead time. This difficulty is overcome by a spin echo technique such as the Carr-Purcell-Meiboom-Gill (CPMG) echo train [14] in which the initial 90° B_1 pulse is followed by a series of 180° B_1 pulses that refocus the magnetic moments. In a CPMG experiment, the peak signal amplitude, detected at echo time intervals (TE), is given by [13]

$$S(n) = M_o \exp\left(\frac{-n \cdot TE}{T_2}\right) \tag{4.4}$$

where n is the echo number, TE is the echo time and T_2 is the spin-spin relaxation time constant. Fig. 4.1 shows the relationship between the signal amplitudes obtained from FID and CPMG experiments.

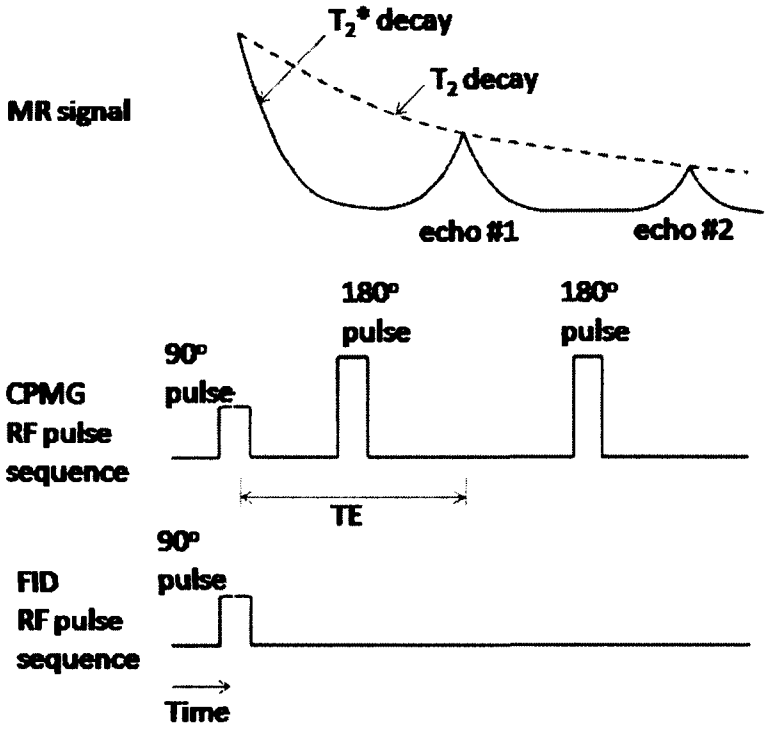

Figure 4.1. FID and CPMG RF pulse sequences with corresponding T_2* and T_2 decays.

MR techniques are applicable to all atomic nuclei having a net magnetic moment. However, MR is most sensitive to ^{1}H and this is the nucleus of importance in our studies. In this case, a gyromagnetic ratio (γ) of 2.675×10^8 rad/s /T is used in Eq. 4.2 to obtain the Larmor frequency. The value of T_2 is linked to the mobility of ^{1}H and reveals information on the viscosity of the bulk material being tested. Typically, T_2 is much longer for liquids than for solids [15]. This feature is utilized in the present work to follow the development of cross-links within the resin during the cure.

4.3 Unilateral magnetic resonance probe

The unilateral magnetic resonance probe employed in this study was based on a three-magnet array [16]. In the array configuration, the permanent magnet blocks (N48 NdFeB magnets supplied by Yuxiang Magnetic Materials Inc. Co. Ltd., Xiamen, China) were polarized in the same direction in a safe (no repulsive force) low energy configuration (Fig. 4.2). The dimensions of the external blocks were 10 x 5 x 3 cm and those of the central block were 10 x 5 x 2 cm. The blocks were enclosed in an aluminum box and separated by 4.76 mm thick fiberglass spacers. The central block was displaced down 4.8 mm from the measuring surface of the probe (top surface in Fig. 4.2) to produce the relatively homogeneous magnetic field required for measurement. The generated field, of approximately 0.11 T in magnitude, was parallel to the surface of the probe, which permitted the employment of a highly sensitive RF transmitter/receiver surface coil. In this purpose-built probe, the RF coil consisted of a four turn 2 cm circular loop placed above the central magnet block. The number of turns, which does not affect the sensitivity of the coil, was chosen to keep the impedance between 20 Ω and 200 Ω [17]. For lower impedances, the resistance of the soldering points can unnecessarily dominate the probe losses while for higher impedances, the magnitude of the probe's electric field can increase its dielectric losses. This type of MR probe is very sensitive and ideal for near surface measurements. The external dimensions of the assembled probe are 11 x 10 x 6 cm and it weighs 3.5 kg, which also makes it portable.

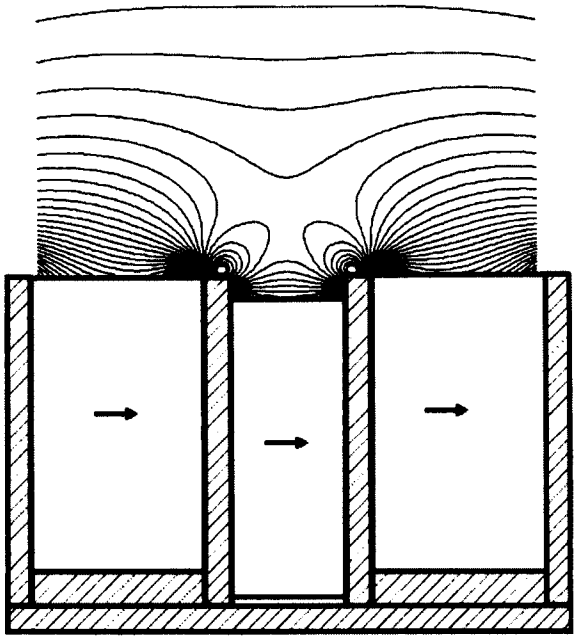

Figure 4.2. Schematic of the three-magnet array utilized in the probe design with the associated magnetic field lines.

4.4 Experimental setup and procedure

The experimental setup was aimed at simulating the oven cure of a thermosetting resin. The studied system was the combination of EPON 9504 epoxy resin with EPIKURE 9554 curing agent (Hexion Specialty Chemicals, Houston, TX), which is a mixture of polyamidoamine, polyethylepolyamine and alkyl amine. EPIKURE 9554 is a low viscosity curing agent designed for vacuum-assisted resin infusion molding (VARIM) of large composite parts used in advanced applications. For each test, small quantities of resin and curing agent were thoroughly mixed in

100/26 proportions, as measured with an electronic balance, to yield samples of approximately 12 g. This amount filled a 30 mL glass beaker to about ⅓ of its capacity. The beaker and sample sizes were selected to match the probe's coil dimensions in order to fill the sensitive volume of the probe.

During the cure, the beaker was heated by a band heating element wrapped with two loops around its circumference (Fig. 4.3). The current supplied to the heating band was controlled manually by a variable AC transformer. The system temperature was monitored with a thermocouple inserted between the heating band and the beaker surface. At the start of the test, the beaker was preheated to the desired cure temperature and stabilized. Then the "liquid" sample was prepared and immediately poured into the beaker. The beaker was held by a mechanical grip at the end of a horizontal arm whose other extremity was joined to a round upright section. This connection permitted free rotation of the arm around the upright axis, allowing rapid positioning and removal of the sample from the unilateral MR probe area (Fig. 4.3). A flexible exhaust duct, placed over the beaker and clipped to the revolving arm, ensured that any volatiles from the curing reaction were evacuated.

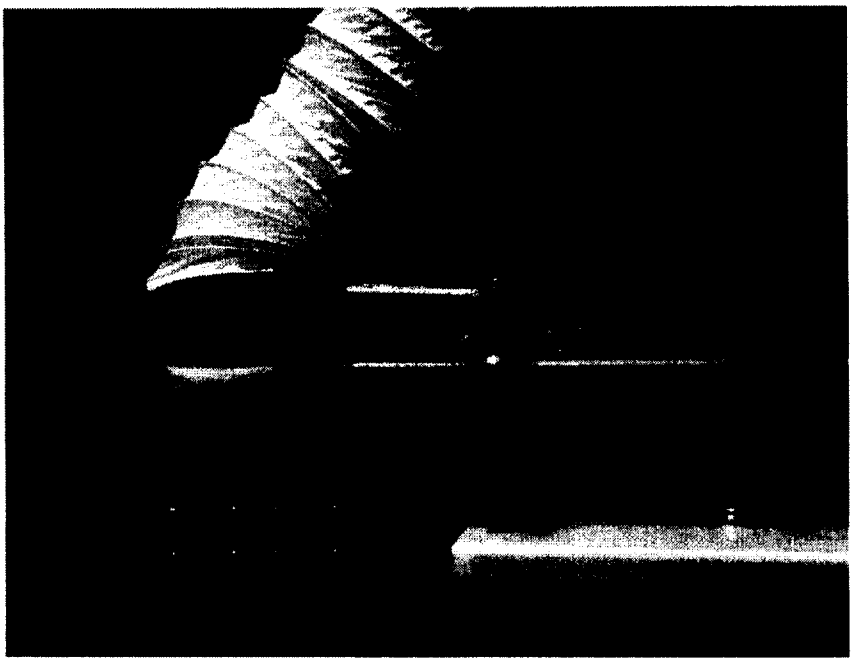

Figure 4.3. Experimental setup. The beaker containing the epoxy resin is heated by a band heating element and held above the NMR probe. The heater was shut off during the measurements because of its electromagnetic interference with the probe.

MR measurements were conducted periodically during the cure. During a measurement, the resin-filled beaker was positioned above the MR probe. The power supply to the heating band was shut off because of its electromagnetic interference with the probe and the measurement was performed. Immediately after the measurement, the heating band was turned back on. In between measurements, the sample was removed from the probe to eliminate the possibility of probe detuning due to a temperature change.

In a real manufacturing setting, the probe would have to be tuned at the oven temperature. In this case, the RF coil would be placed above the magnet inside the oven while the tuning and matching capacitors would lie outside the oven. Once the

oven temperature has stabilized, the circuit could be easily tuned. It should be noted that the magnet blocks (NdFeB grade 48) in the current probe design would be limited to approximately 80 °C as higher temperatures may result in demagnetization. Higher temperature applications may require the utilization of other types of magnets such as SmCo (T_{max} = 350 °C). Finally, it should also be noted that NMR cure monitoring of carbon-fiber composites may be limited due to the conductivity of these fibers (although this was not attempted here). However, composites with non-conductive reinforcements, such as glass and aramid fibers, would be exempt from these limitations.

4.5 Results

4.5.1 Room temperature cure

The operating frequency of the MR system was 4.7 MHz (0.11 T). The duration of the 90° pulse (4 μs) was determined as the pulse length that maximized the MR signal amplitude in the liquid resin. In the CPMG experiments, the 180° pulse was obtained by keeping the same pulse length and doubling the pulse amplitude compared to the 90° pulse. A preliminary investigation on the epoxy resin system revealed T_1 to be approximately 40 ms in the uncured state. The MR signals presented here are the sum of 32 scans from a CPMG train of 500 echoes, with an echo time of 0.1 ms and a recycle delay of 200 ms (to avoid signal loss due to incomplete recovery). The total measurement time was 8.0 s.

As a first experiment, MR measurements were performed at predetermined curing time intervals during a twelve hour period, on a sample that was prepared and let cure at room temperature. The resin temperature remained essentially constant during the course of the experiment. Representative T_2 decay data of this experiment for selected curing times are plotted in Fig. 4.4. For a given curing time, the detected MR signal intensity decreases exponentially with the measurement time. A comparison of the curves reveals that the initial signal amplitude (i.e., from the first echo) decreases with the curing time. The signal also decays faster at longer curing times. Both of these effects are attributable to the increase in cross-link density within the resin as it becomes progressively more solid like.

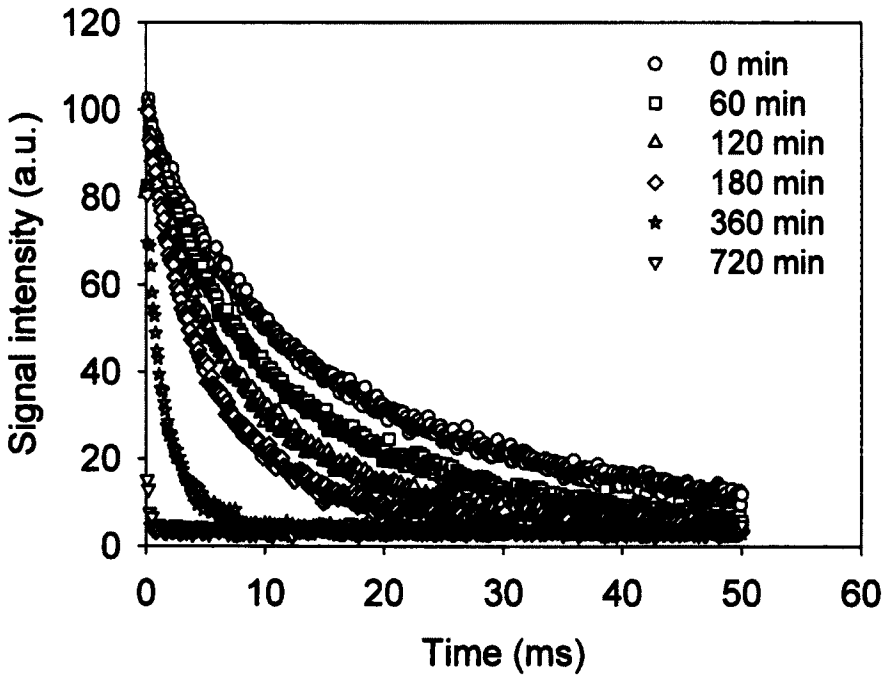

Figure 4.4. T_2 decay data from the curing experiment at room temperature.

In general, the complexity of the T_2 relaxation mechanisms may require a spectrum of exponential decay functions for accurate mathematical description. However, in common practice, the relaxation mechanisms are adequately represented by a Prony series with a finite number of decay constants. In the present case, as shown in Fig. 4.5, the T_2 decay is well described by a bi-exponential decay equation in the form

$$S(t) = M_S \exp\left(\frac{-t}{T_{2S}}\right) + M_L \exp\left(\frac{-t}{T_{2L}}\right) \tag{4.5}$$

where M is the signal amplitude backextrapolated to time 0, i.e. immediately after the 90° pulse, and T_2 is the spin-spin decay time constant associated with M. Indices S and L refer to the short and long components of the signal, respectively.

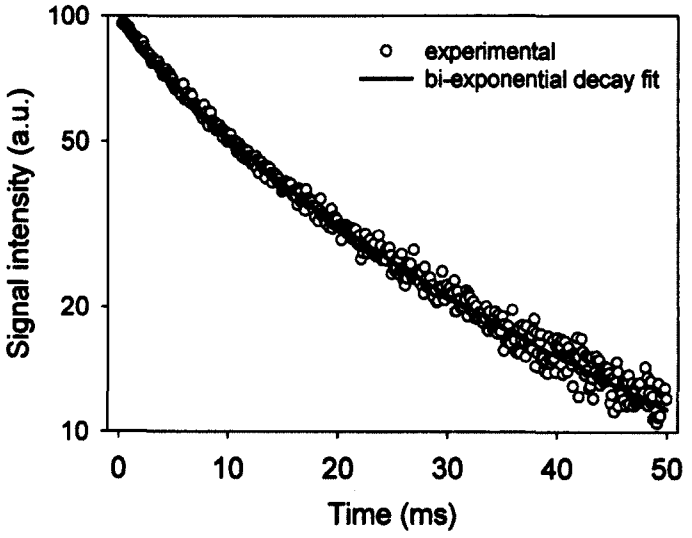

Figure 4.5. Experimental data for the T_2 (CPMG) decay of liquid resin. The solid line represents the bi-exponential curve fit.

Equation 4.5 was fit to the experimental data of each measurement in Fig. 4.4, corrected to remove the baseline offsets, to obtain the corresponding amplitudes and time constants. The results are presented in Fig 4.6. Fig. 4.6a reveals that the time constants T_{2S} and T_{2L} decrease monotonically with the curing time until they become practically equal after 500 min. The change in T_{2L} from the beginning to the end of the curing process is greater than the change of T_{2s}, which would make it a better indicator of state of the resin. Fig. 4.6b gives the signal amplitudes M_L, M_S and the sum of both terms as a function of curing time. While M_S has a relatively constant value after 100 min, M_L and the total signal amplitude decrease as the resin hardens. Based on these results, it appears that the parameters of the long signal component could be correlated with the state of the resin.

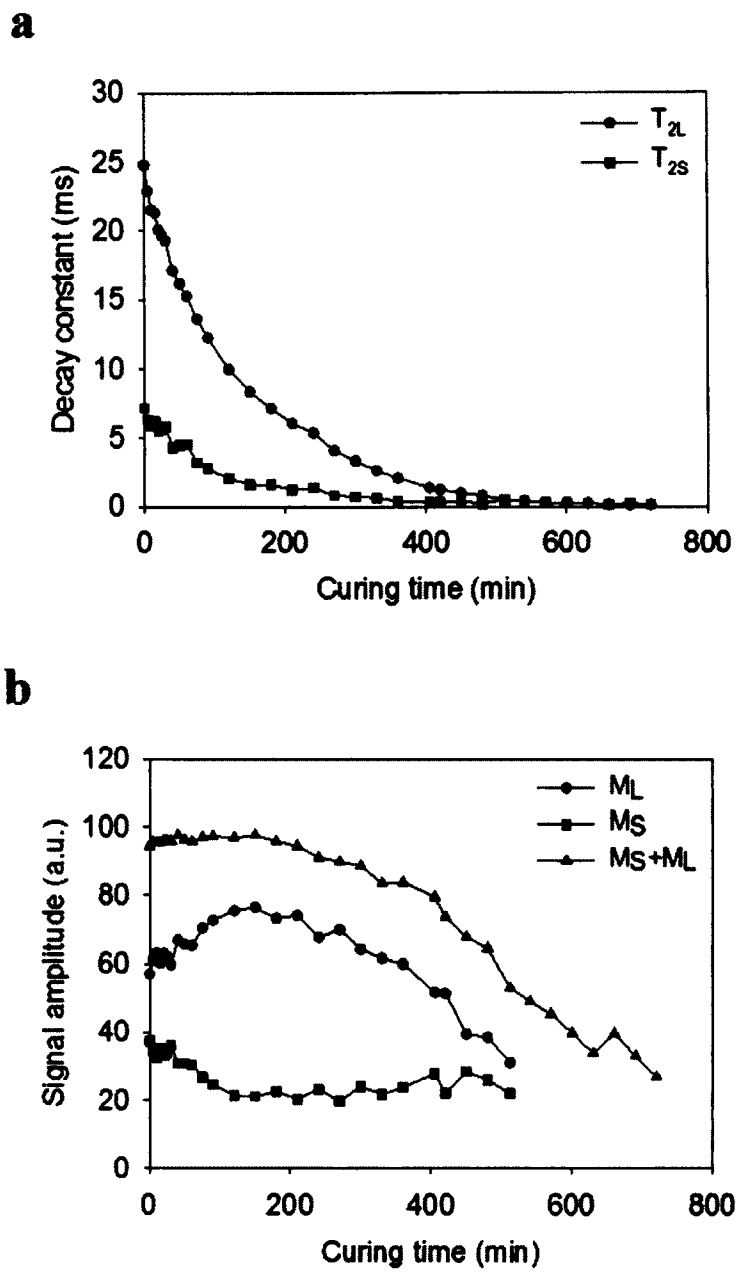

Figure 4.6. Experimental results from the cure at room temperature. a) Evolution of the time constants. b) Evolution of the signal intensity. Note that the signal intensity curves M_L and M_S end at approximately 500 min, a time where the corresponding time constants T_{2L} and T_{2S} become identical. After 500 min, only the total signal intensity is represented.

4.5.2 High temperature cure

The above experiment was repeated at various curing temperatures between 50 °C and 90 °C, and the results are presented in Fig. 4.7. In these cases, more complex trends in the relaxation parameters were expected due to the mechanisms involved. When a thermally activated thermosetting resin is heated, its viscosity initially decreases. However, as the cross-links form, the viscosity reaches a minimum value, known at the gelation point, and then starts to increase, eventually leading to vitrification.

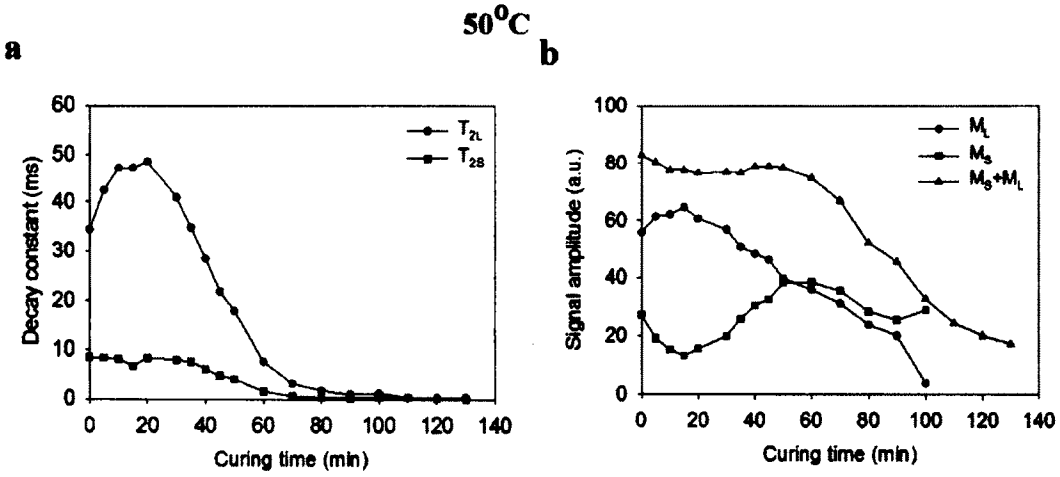

60°C

c

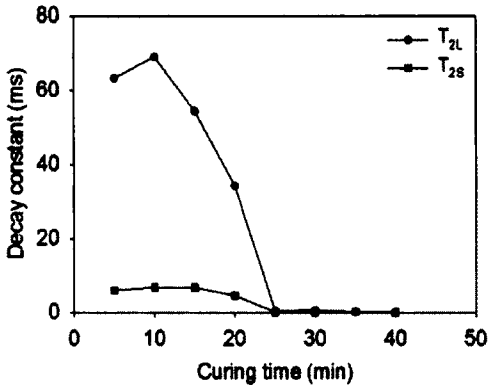

d

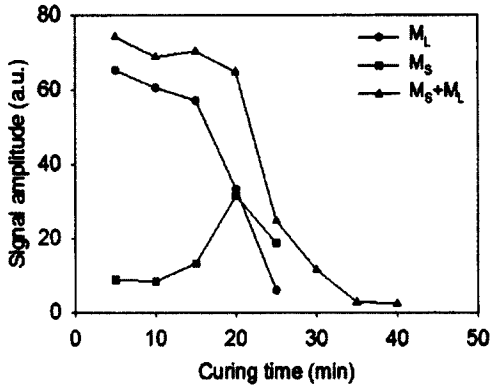

70°C

e

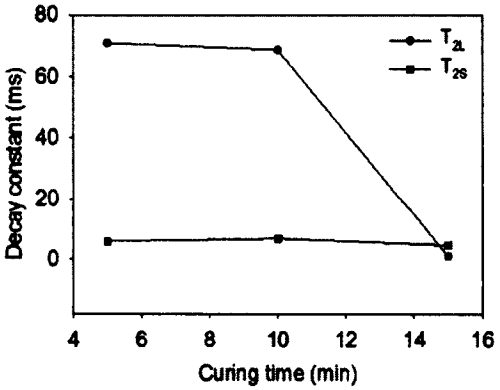

f

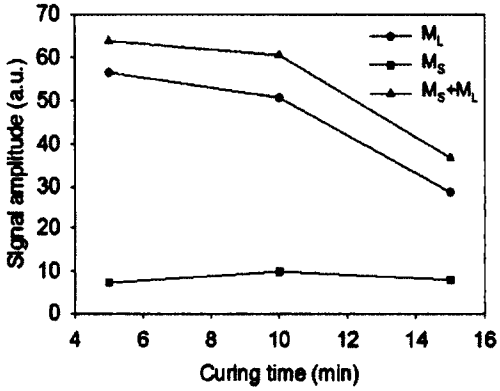

90°C

g

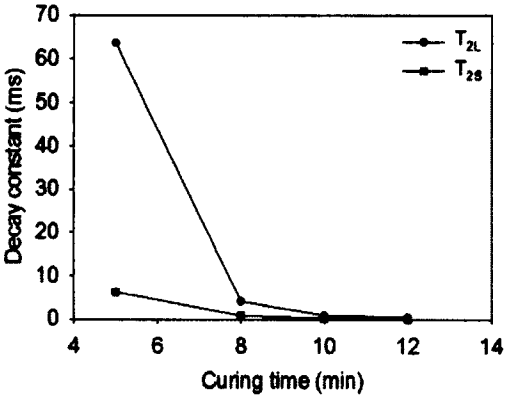

h

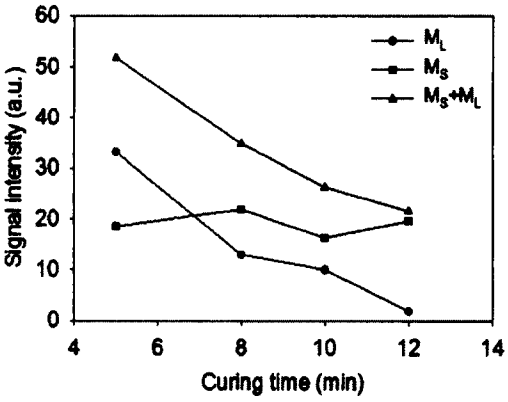

Figure 4.7. Experimental results from the high temperature cures. a) Evolution of the time constants during the cure at 50 °C. b) Evolution of the signal intensity during the cure at 50 °C. c) Evolution of the time constants during the cure at 60 °C. d) Evolution of the signal intensity during the cure at 60 °C. e) Evolution of the time constants during the cure at 70 °C. f) Evolution of the signal intensity during the cure at 70 °C. g) Evolution of the time constants during the cure at 90 °C. h) Evolution of the signal intensity during the cure at 90 °C. Note that in b and d, the signal intensity curves M_L and M_S end at the point where the corresponding time constants become identical. After that point, only the total signal intensity is represented.

During the cure at 50 °C, the temperature of the resin increased from room temperature to 50 °C within 3 min after pouring it in the beaker. During the first 15 min of cure, the temperature decreased by about 5 °C during the MR measurements (heater off for 45 s), but returned to 50 °C within 15 s after the heater was turned back on. Temperature variations will have an effect on T_2. However, after 15 min of curing, the exothermic reaction within the resin produced enough heat to maintain the temperature at 50 °C during the MR measurements. Fig. 4.7a indicates that, during the cure, T_{2L} initially increases to reach a maximum value of 48 ms after 15-25 min and then decreases asymptotically to a near zero value at the end of the cure. Fig. 4.7b shows a similar trend in M_L while the M_S behavior is more complex. These results further prove that the state of the resin could be correlated with the parameters from the long component of the signal.

Similar trends are observed at cure temperatures of 60, 70 and 90 °C, except that the cure occurs faster at higher temperature. At 60 °C (Fig. 4.7c), T_{2L} decreases from a maximum value of 69 ms to a near zero value between curing times of 10-25

min, a time period which also corresponds to a large decrease in M_L (Fig. 4.7d). At 70 °C (Fig. 4.7e and f) and 90 °C (Fig. 4.7g and h), the sharp decrease in T_{2L} and M_L are observed in curing time ranges of 10-15 and 5-8 min, respectively. In all cases, the unilateral MR probe clearly detected changes due to the evolution of the cure process.

Fig. 4.8 shows the temperature profile of the epoxy resin during the cures at 60 and 70 °C. At these cure temperatures, cross-linking occurs rapidly in the epoxy system and the heat generated by the exothermic reaction causes a temperature overshoot in the resin. The higher the cure temperature, the faster the occurrence of the peak resin temperature and the higher the peak. It is interesting to note that the cure time at which the peak temperatures are observed (25 min for 60 °C cure and 15 min for 70 °C cure) corresponds in both cases to the time at which T_{2L} reached a very small value in Figs. 4.7c and e. This constitutes proof that the cure is practically complete at that point because no extra heat is generated by the exothermic reaction.

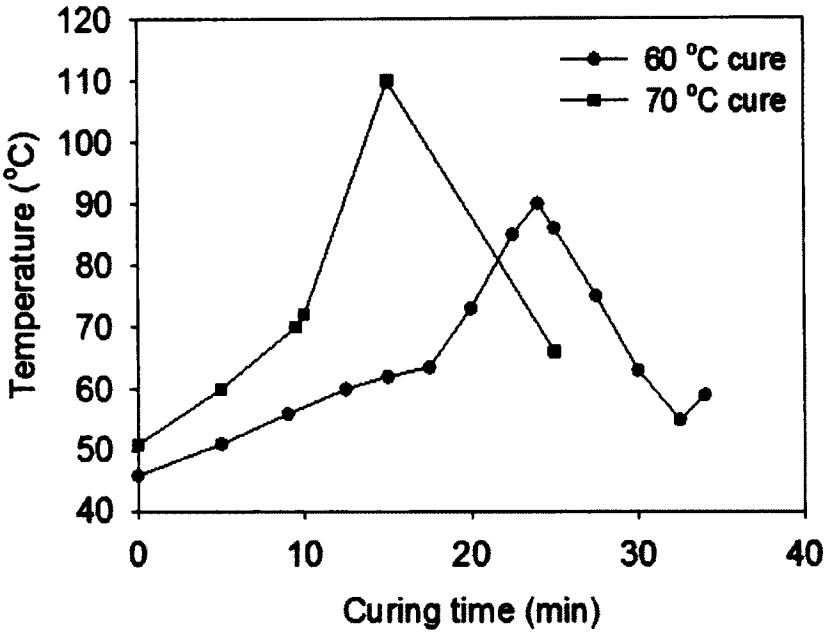

Figure 4.8. Temperature profile of the epoxy resin during cure.

4.5.3 Rapid measurement

The preceding section has shown that the cure of an epoxy resin system can be monitored by a unilateral MR probe. With the CPMG measurement, the monitoring required 32 scans (to obtain an adequate signal-to-noise ratio by observation) plus curve fitting to a bi-exponential decay equation for analysis. However, it is important to minimize experimental time if this technology is to be used in real applications. Ideally, the measurement should be completed in a single scan.

A modified CPMG method is proposed here, based on [18], to get faster information on the state of the cure in a single scan. As shown in Fig. 4.4, the observable MR signal decreases as the solid is formed during the curing process.

This behavior is exploited by summing the signal amplitudes from all the echoes in a CPMG sequence. With this method, the long decays and large amplitudes from the low viscosity resin will produce a larger summation result than the shorter decays and smaller amplitudes from the higher viscosity resin. In the present measurement, a train consisting of 200 echoes was utilized. Fig. 4.9 shows the result of the sum of 200 echoes for different times during the cure at 50 °C. The amplitude of the echo sum decreases during the cure interval considered. The measurement time of this method was 20 ms, which is very fast in comparison with the 8.0 s of the previous measurement.

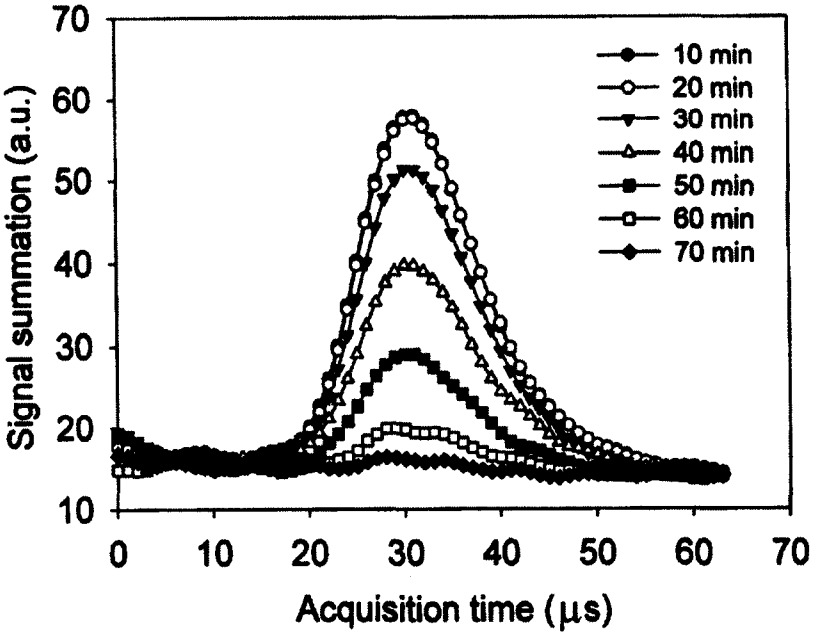

Figure 4.9. Results from the sum of 200 echo signals during cure at 50 °C. The abscissa corresponds to the time elapsed in the 63 μs acquisition window centered on each echo.

Fig. 4.10 presents the results of the application of this method to the curing process. For each cure temperature, the decrease in the signal intensity corresponds to an increase in resin viscosity leading to solidification. For the cure temperatures of 60 °C, 70 °C and 90 °C, the sharp decreases in signal intensity occur at times corresponding to the observations made with the conventional CPMG measurements and curve fitting. For the 50 °C cure, the signal intensity decreases more gradually, which is also in agreement with the conventional CPMG measurements. The proposed measurement provides similar information on the curing resin as the previous one in a fraction of the time. In addition, the measurement time could be reduced even further by using a shorter echo time and averaging more echoes.

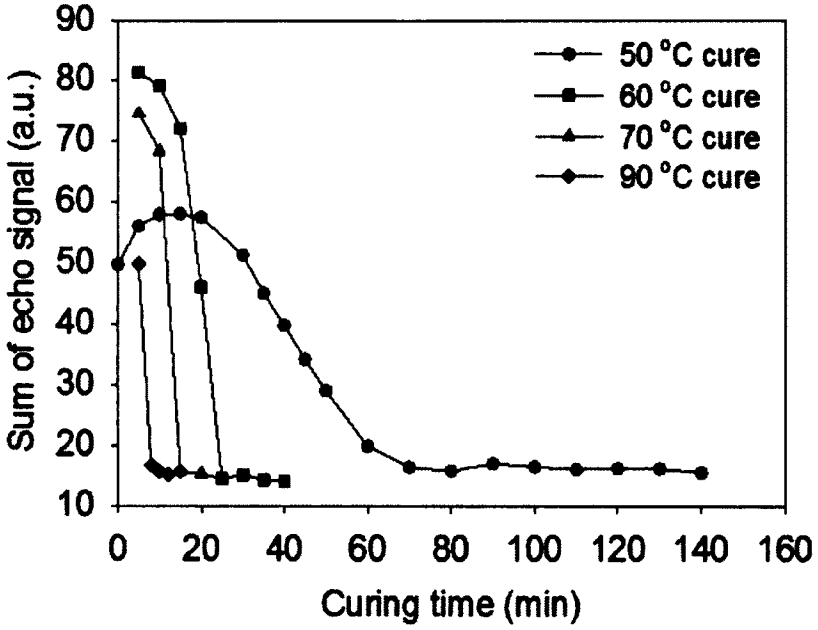

Figure 4.10. Results from the modified CPMG method.

4.6 Conclusion

This study has shown that, with an appropriate magnet array configuration, a simple portable unilateral MR probe can rapidly provide real-time information on the state of a curing thermosetting resin. The MR measurement is very rapid; it is performed in 20 ms. This method could be applied to the monitoring of a curing composite part. Although the MR measurement presented is a point-by-point spatially resolved technique, the probe could be moved to scan areas of reasonable size by moving from point to point across the surface of the part being fabricated. The technique could also possibly be used for quality control of composite parts where regions of incomplete cure would be detected by the unilateral probe.

Acknowledgements

The authors thank Composite Atlantic Ltd. (Lunenburg, NS, Canada) for supplying the epoxy resin and curing agent. G.L. thanks the Natural Science and Engineering Council (NSERC) for a Discovery grant. B.J.B. thanks the Canada Chairs Program for a Research Chair in MRI of Materials. The UNB MRI centre is supported by an NSERC Major Resources Support grant.

References

[1] LaPlante G, García-Naranjo JC, Balcom BJ, Real-time cure monitoring of an epoxy/polyamidoamine system with unilateral magnetic resonance, NDT&E International 2011; 44: 329 - 34.

[2] Maistros GM, Partridge IK, Dielectric monitoring of cure in a commercial carbon-fibre composite. Comp Sci Technol 1995; 53: 355-9.

[3] Challis RE, Unwin ME, Chadwick DL, Freemantle RJ, Partridge IK, Dare DJ, Karkanas PI, Following network formation in an epoxy/amine system by ultrasound, dielectric, and nuclear magnetic resonance measurements: A comparative study. J Appl Polym Sci 2003; 88: 1665-75.

[4] White SR, Mather PT, Smith MJ, Characterization of the Cure-State of DGEBA-DDS Epoxy Using Ultrasonic, Dynamic Mechanical and Thermal Probes. Polym Eng Sci 2002; 42: 51-67.

[5] Cocker RP, Chadwick DL, Dare DJ, Challis RE. A low resolution pulsed NMR and ultrasound study to monitor the cure of an epoxy resin adhesive. Int J Adhes Adhes 1998; 18: 319-31.

[6] Macan J, Bernardic I, Ivankovic M, Mencer HJ, DSC study of cure kinetics of DGEBA-based epoxy resin with poly(oxypropylene) diamine. J Therm Anal Calorim 2005; 81: 369-73.

[7] Mertzel E, Koenig JL. Application of FT-IR and NMR to epoxy resins. In: Dusek K, editor. Epoxy Resins and Composites II, Heidelberg. Berlin:Springer; 1986. P. 73-112.

[8] Andreis M, Koenig JL, Application of NMR to crosslinked polymer systems. In: Cantow HJ, editor. Polymer Characterization/Polymer Solutions, Heidelberg: Springer Berlin 1989, p. 69-160.

[9] Koller E, Kuhn W, Dobmann G, Kroning M. Magnetic resonance techniques (spectroscopy and imaging) for the nondestructive characterization of polymeric materials and composites. Nondestr Test Eval 1992; 8; 733-44.

[10] Blümich B, Perlo J, Casanova F, Mobile single-sided NMR. Prog Nucl Mag Res. Sp 2008; 52: 197–269.

[11] Eidman G, Savelsberg R, Blumler P, Blumich B. The NMR MOUSE, a mobile universal surface explorer. J Magn Reson A 1996; 122: 104-9.

[12] Banwell CN, Fundamentals of molecular spectroscopy. 3rd ed. New York: McGraw-Hill; 1983.

[13] Callaghan P, Principles of nuclear magnetic resonance microscopy, Oxford: Oxford University Press; 1991.

[14] Meiboom S, Gill D, Modified spin-echo method for measuring nuclear relaxation times. Rev Sci Instrum 1958; 29: 688-91.

[15] Stanley RK. Special nondestructive testing methods. In: Moore PO, McIntyre P, editors. Nondestructive testing handbook. 2nd ed. Columbus, OH: ASNT; 1995. P.398–420.

[16] Marble AE, Mastikhin IV, Colpitts BG, Balcom BJ. A compact permanent magnet array with a remote homogeneous field. J Magn Reson 2007;186:100–4.

[17] Mispelter J, Lupu M, Briguet A. NMR probeheads for biophysical and biomedical experiments, theoretical principles & practical guidelines. London: Imperial College Press; 2006.

[18] Randall EW, Nunes TG, Guillot G, Bodart PR. T_1-weighting of echo-trains in the stray-field for deuterium: prospects for imaging using long echo-train summation. Solid State Nucl Magn Reson 1999;14:165-72.

Chapter 5

A unilateral magnet with an extended constant magnetic field gradient.

This chapter is largely based on the paper "A unilateral magnet with an extended constant magnetic field gradient" published in Journal of Magnetic Resonance, 207, 2010, 337-344 [1]. It presents a new approach to the three-magnet array which features extended constant magnetic field gradients. Constant gradients of more than 3 cm extent can be achieved in a very simple, compact and safe design. Diffusion measurements from different positions over the magnet are presented in addition to practical applications for reservoir core plug characterization.

5.1 Introduction

In recent years Unilateral Magnetic Resonance (UMR) has became a powerful tool to explore samples of arbitrary size; permitting magnetic resonance experiments on more complex and challenging samples. A wide range of applications have been developed in

different areas such as down-hole oil well logging [2], biomedicine [3], concrete materials analysis [4] and characterization of food products [5]. The first area of application is now ubiquitous in the oil industry.

Different magnet designs have been proposed to create an MR compatible static magnetic field. Three main classes can be easily differentiated taking into account the distribution of the static magnetic field. In the first class [6, 7] the orientation of the magnets and RF coil are arranged in such a way that the grossly inhomogeneous B_0 and B_1 remain perpendicular in specific regions which, in conjunction with the RF excitation bandwidth, defines a sensitive spot for the measurement. A second class includes those magnets designed to produce a relatively homogeneous B_0 field in a defined region of space [2, 8, 9, 10, 11, 12]. This yields a large spot for RF excitation and reduces diffusive attenuation of gradients by molecular motion through underlying magnetic field.

The third class of unilateral magnets features a linear magnetic field distribution (constant gradient) in a region of interest which is suitable for profiling and diffusion measurements. Prado et al. [13] presented a palm-size unilateral magnet design which includes gradient coils. This design permits pulsed field gradients, making possible the application of pure phase encoding techniques. Blumich et al. [14] introduced a variation of the NMR-MOUSE employing a single bar magnet, with a constant gradient of around 2000 G/cm in its central part. This approach is very simple but the linear region of the magnetic field is limited to around 4 mm. Casanova and Blumich [15] and Perlo et al. [16] developed these ideas for 2D and 3D with an optimized design of the magnets, a set of switched magnetic field gradient and a new multi-echo sequence. Nevertheless, as in the

Prado approach, these ideas require a power source to produce the desired magnetic field gradients.

Perlo et al. [17] more recently introduced a magnet with a permanent gradient of 2000 G/cm perpendicular to the magnet surface. As in the STRAFI technique [18], the major effort was focused on producing a very uniform spot in a plane parallel to the magnet surface. This homogeneous plane is achieved by doubling the number of magnets in the original MOUSE and improving their spatial distribution. Selection of the plane of measurement inside the sample is achieved by changing the position of the magnet relative to the sample. This approach can produce high resolution profiles, but requires a complex magnet design, with associated complexity of fabrication.

A different approach to unilateral magnetic resonance with a constant gradient was suggested by Marble et al. [19]. He advocated the use of a shaped pole piece to create a permanent gradient. Magnetic field gradients of 30 to 250 G/cm have been produced based on this idea.

In separate work, Marble et al. conceived a very simple approach [11] for producing a homogenous spot unilateral magnet. This approach employs three simple magnet blocks, with the same field orientation, arranged along the same axis in a very safe (no repulsive forces) low energy configuration. In this way, the desired magnetic field distribution is achieved with a very compact design [20]. The natural field orientation, B_0 parallel to the surface, permits more sensitive surface coils to be employed for RF

excitation and detection. The relatively simple mathematical expressions required for calculating the field distribution make this approach very easy to simulate [11].

As outlined in this paper, vertical displacement of the central magnet block changes the design, from a uniform spot to an extended constant magnetic field gradient perpendicular to the magnet surface. Our desire is to create a new type of constant gradient unilateral magnet with a simple and robust design where the gradient is permanent. Practical measurements show that it is possible to generate constant gradients of more than 3 cm extent perpendicular to the magnet surface in a 1 cm diameter cylindrical volume.

In this paper we examine the properties of the constant gradient three-magnet array through simulation and experiment. We introduce the idea of a simple solenoidal RF coil encompassing cylindrical samples to aid sensitivity and selective excitation of regions substantially removed from the magnet surface. Samples of particular interest include petroleum reservoir core plugs within which we measure molecular self diffusion of the saturating fluid, exploiting the extended constant gradient in the sample space.

5.2 Theory

Our experimental goal is the creation of simple, low cost, magnet arrays with the B_0 field parallel to the magnet array surface. The magnetic field gradient is permanent, not switched, but may be readily adjusted by displacing the central magnet. This design permits the use of sensitive RF probes which may be surface coils or solenoids. In the latter case the long axis of the probe will be oriented in the x axis (see Fig. 5.1b). The

solenoid naturally yields a more homogeneous B_1 and will permit RF excitation over the full range of the constant magnetic field gradient permitting measurement at a wide range of depths into the sample.

5.2.1 Three-magnet array.

The distribution of the magnetic field over a three-magnet array can be calculated by evaluating Eq. 1 in [11], for each single block of width *w* and height *t* and superposing the results according to their positions in the *y*-*z* plane.

Figure 5.1 presents a constant gradient magnet array built employing this approach. Magnet blocks with the same dimensions as those described in [11] were employed. Magnetic field compensation with a steel plate, as described in [11], was unnecessary.

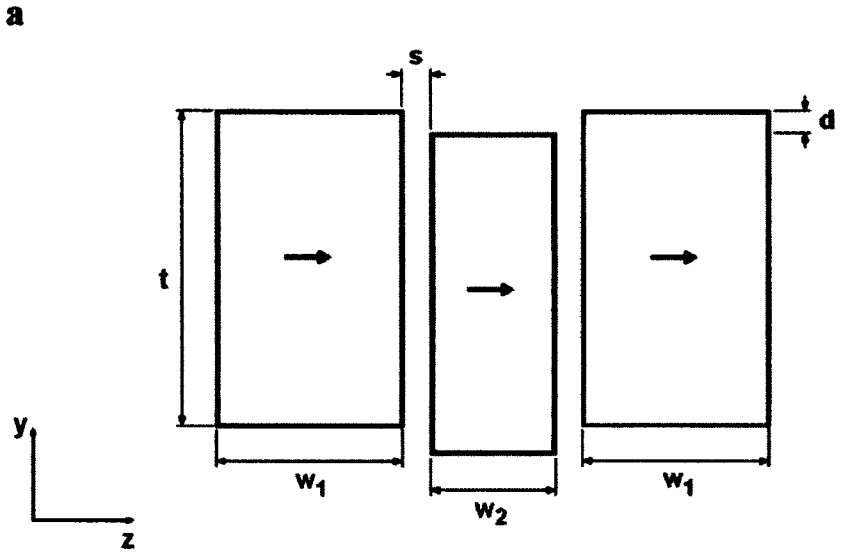

b

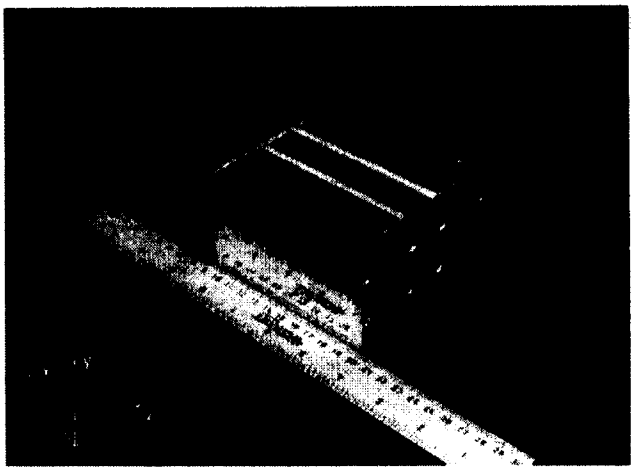

Figure 5.1. Schematic (a) and photo (b) of the three-magnet array. The static field B_0, parallel to the array surface, is oriented in the z direction. The width of the external (w_1) and central (w_2) blocks is 3 cm and 2 cm respectively. The separation between blocks was set to 4.76 mm and the displacement of the central block (d) is 2 mm for extended constant gradient.

It is straightforward, to calculate the first and second derivatives of the magnetic field produced by the three-magnet array along the *y* axis. Nevertheless, it is more complex to calculate the zeros of the second derivative as a function of the physical dimensions of the magnet array. A simple numerical evaluation of this function is preferred.

5.2.2 Extended constant gradient

Evaluation of the first derivative (gradient) of the magnetic field on a vertical line (*y* axis) over the centre of the array for a homogeneous spot design (solid line) is presented in Fig. 5.2. As can be observed, it is characterized by the presence of a maximum value, zero for homogeneous spot, followed by a minimum. The amplitude of the minimum,

termed the natural gradient hereafter, principally depends on the separation between the external magnet blocks (measured from their central line) and therefore cannot be changed once the array is built. However, the amplitude of the maximum is more dependent on the position of the central block and can be easily changed by moving it up or down.

Figure 5.2 presents the calculated magnetic field gradient for different positions of the central magnet block. As can be observed, different gradient values can be added to the sensitive spot (maximum of the curve) without a significant influence on the natural gradient. In fact, the central block can be displaced in such a way that the variable and natural gradients combine to produce an extended constant gradient with amplitude depending on the separation of the external blocks.

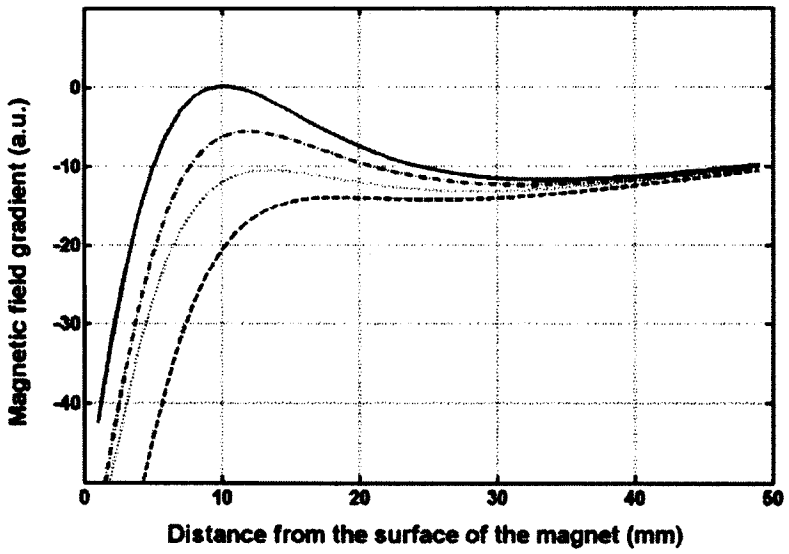

Figure 5.2. Magnetic field gradient along a vertical line on the centre of the array. A homogenous spot design (solid) translates to an extended constant gradient design (dashed) by vertical displacement of the central block from 4.8 to 2 mm from the surface. Intermediate positions exhibit small regions, near 1 cm, of good linearity (variable gradient) at lower gradient values. The extended

constant gradient is obtained by combining the variable (curve maximum) and natural (curve minimum) gradient of the array.

5.2.3 The probe

It is common practice in UMR to employ surface coils as the RF probe. As mentioned before, the orientation of the magnetic field produced by the three-magnet array allows exploiting the high sensitivity of the circular loop probe. Nevertheless, in some applications it is desirable to explore deep layers inside the sample, which makes more challenging the employment of surface coils. Increasing its diameter to increase the penetration depth will make the coil more susceptible to external interference and other undesirable effects but less sensitive to the desired signal through the principle of reciprocity.

In applications like rock core plug analysis, the shape of the sample suggests the employment of a solenoid oriented along the x-axis as the RF probe. It can be tailored to the sample, or a set of samples, in a very simple and well known way. For the three-magnet array with extended constant gradient, the well controlled distribution of the magnetic field makes even simpler the employment of a solenoid which, in addition, will contribute with a very homogeneous B_1 field.

5.2.4 Diffusion measurements

Diffusion in the presence of a constant gradient has been studied by many laboratories employing the fringe field of superconducting magnets [21, 22, 23, 24], well

logging tools [25] and portable systems [26]. Obtaining constant gradients over an extended distance in a unilateral magnet is a very challenging design goal.

Different pulse sequences have also been employed for measuring diffusion [21, 22, 26] in static gradients. In this work the static gradient stimulated echo sequence with 16 phase cycle steps [22] is employed to characterize the gradient produced by the three-magnet array. It is also exploited for measurements in realistic samples from petroleum reservoirs.

5.2.4.1 Static gradient stimulated echo sequence

The static gradient stimulated echo sequence (SGSTE) combined with CPMG (SGSTE-CPMG) as presented in Fig. 5.3 was introduced by Hurlimann and Venkataramanan [22] as a variation of the Laicher [27] approach for pulsed field gradient diffusion. Hurlimann added a 16 step phase cycling to select the contribution of the stimulated echo in order to obtain diffusion-T_2 distributions. The same sequence has been employed by Rata [26] for measuring diffusion with a reference acquisition at very short τ_2 as a normalization signal. In this case Eq. 5.1 was employed assuming no diffusive attenuation during the reference acquisition for a short τ_2.

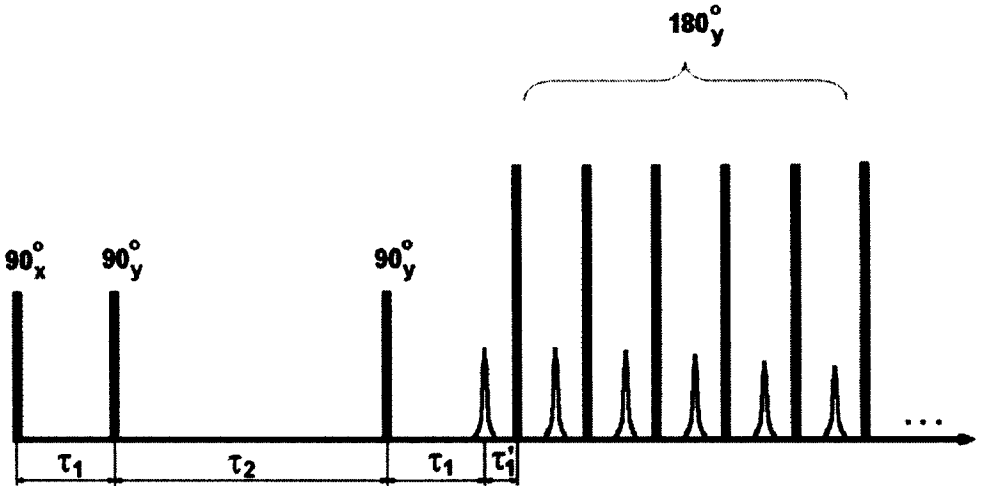

Figure 5.3. SGSTE pulse sequence combined with CPMG. For each diffusion measurement eight τ_1 values were employed. A reference acquisition for τ_2 of 0.5 ms was also performed

$$\ln\left(\frac{I}{I_0}\right) = -\gamma^2 G^2 D \tau_1^2 (\tau_2 + \frac{2}{3}\tau_1) \qquad (5.1)$$

This assumption makes more complex the process of choosing the τ_1 values for the measurement. The SGSTE sequence, as described in [21], should be relaxation independent, which means that the τ_1 values during the acquisition process should be the same as those employed for the reference acquisition. Therefore, the longest τ_1 cannot be longer than τ_2 for the reference acquisition. At the same time the τ_1 values should be spaced sufficiently to differentiate the signal attenuation produced by the diffusion process from the noise.

A simple mathematical analysis of Eq. 5.2 [24] for the reference and the measurement acquisitions yields Eq. 5.3 for the normalized signal attenuation where τ_{2r} is the τ_2 value employed for the reference acquisition.

$$M = \frac{M_0}{2} exp\left\{-\frac{\tau_2}{T_1} - \frac{2\tau_1}{T_2} - \gamma^2 D G^2 \tau_1^3 \left(\frac{2}{3} + \frac{\tau_2}{\tau_1}\right)\right\} \tag{5.2}$$

$$\ln\left(\frac{I}{I_r}\right) = -\frac{(\tau_2 - \tau_{2r})}{T_1} - \gamma^2 G^2 D \tau_1^2 (\tau_2 - \tau_{2r}) \tag{5.3}$$

For a chosen τ_2 the first addend is constant and the slope of the curve of attenuation versus τ_1^2 can be employed to calculate either the diffusion coefficient or the gradient. Even though this method requires an extra acquisition, the overall acquisition time can be reduced because of the increased SNR produced by averaging the CPMG echo train for both the reference and the measurement acquisitions.

5.2.4.2 Time-dependent diffusion coefficient

Diffusion measurements employing the SGSTE-CPMG sequence can be employed in order to obtain the volume to surface ratio (V/S) in rock core plugs [26]. By varying the diffusion time (τ_2) water molecules are allowed to diffuse for a length $L_D = \sqrt{D_0 \tau_2}$. In porous media this distance is limited by the pore walls resulting in an apparently smaller diffusion coefficient. By plotting the apparent diffusion coefficient vs. diffusion length, the value of V/S can be obtained by assuming linear behavior for short diffusion lengths according to Eq. 5.4 [26].

$$D(L_D) \approx D_0[1 - \frac{4}{9\sqrt{\pi}} \frac{L_D S}{V}] \quad (5.4)$$

5.3 Results and Discussion

Figure 5.4 presents the measured magnetic field over the prototype constant gradient magnet. The gradient strength is 218 G/cm over a constant region of 2.4 cm, with a maximum deviation of 1.5 G from linear behavior (Fig. 5.4a). The magnetic field measured 5 mm from the magnet centre to the left, right, front and back has also been plotted (Fig. 5.4b). Figure 5.4c shows the magnetic field plotted along horizontal lines (x and z directions) at three different heights over the magnet (1.3, 2.3 and 3.3 cm). The variation of the magnetic field is approximately 0.4% in the x direction and 1% along z. When the measurement point is moved to the right the error reached 1.7% for the plane closer to the magnet, which may be caused by small differences between the external blocks.

a

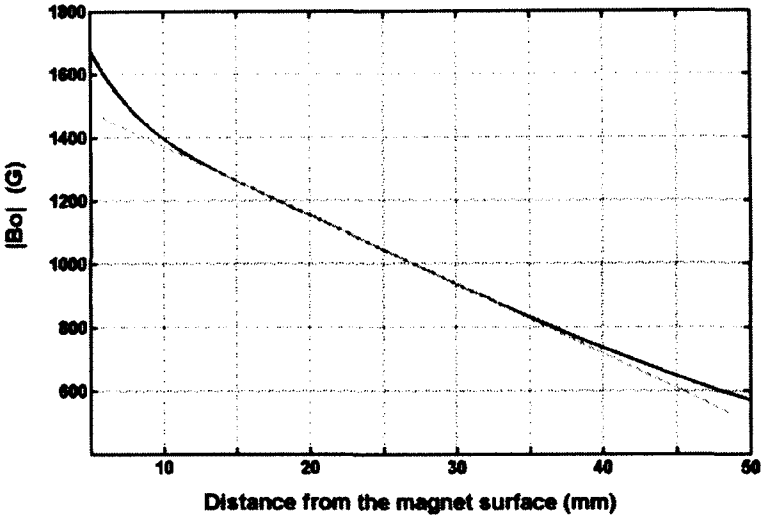
1800
1600
1400
1200
1000
800
600
|Bo| (G)
10
20
30
40
50
Distance from the magnet surface (mm)

b

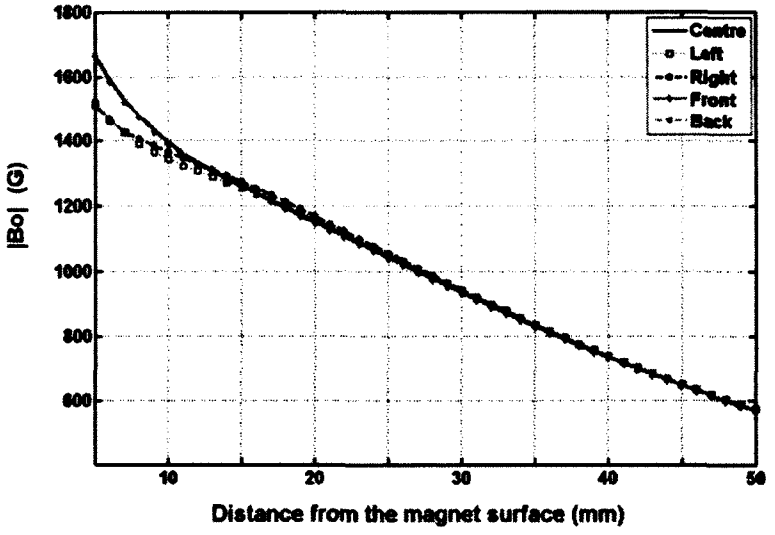
Centre
Left
Right
Front
Back
1800
1600
1400
1200
1000
800
600
|Bo| (G)
10
20
30
40
50
Distance from the magnet surface (mm)

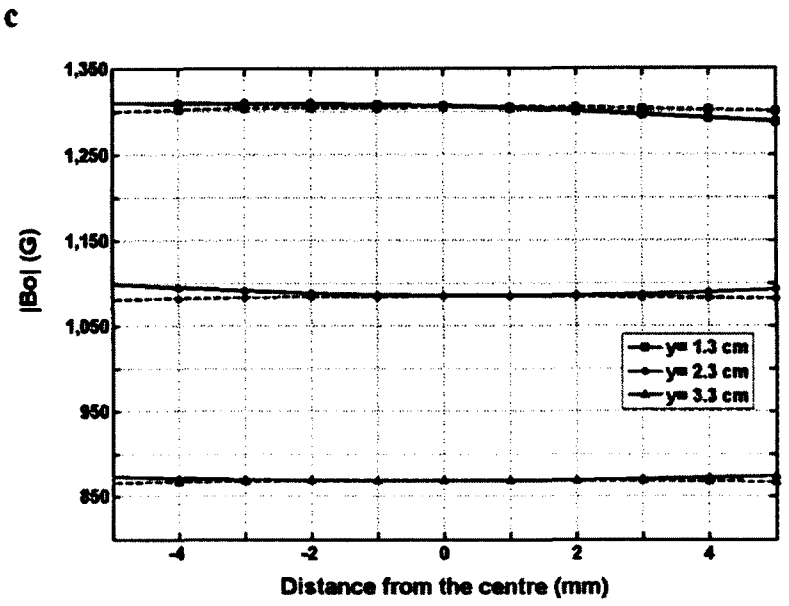

Figure 5.4. Measured magnetic field over the magnet. The extended constant gradient of 218 G/cm at the centre of the array is clearly observed in (a). The magnetic field on vertical lines spaced 5 mm from the centre have been plotted in (b). The magnetic field along horizontal lines (c) at three heights over the magnet. Solid and dashed lines correspond to measurements along the z and x axes respectively.

In order to obtain the desired constant gradient, the central block was displaced 2 mm down from the surface. The magnet blocks were spaced employing a fiberglass spacer to avoid acoustic ringing as described in [28, 29]. The outer case is still aluminum but because the case walls are further away from the RF coil they do not produce any appreciable ringing.

Diffusion measurements employing a 4 ml sample of distilled water were carried out at heights of 15.5, 20, 24.5 and 29 mm over the magnet. The surface coil and the sample were displaced in tandem with retuning as necessary for each position. The sample was placed over the coil with its long dimension in the x axis. Gradient values of 217, 220,

219 and 222 G/cm respectively were measured, from SGSE-CPMG measurements using a known water diffusion coefficient of 2.07 x 10^{-9} m^2/s at 21 °C.

In addition, a diffusion measurement employing CPMG for different τ values was undertaken for a 24.5 mm sample height. The measured gradient in this simple case was 223 G/cm. Figure 5.5 shows the results of the measurement at this position for SGSE-CPMG (Fig. 5.5a) and CPMG with variable τ (Fig. 5.5b). A good agreement is observed between the measurement from the three axis magnetic field plotter and the calculated gradient derived from both diffusion measurements. Small variations in the gradient value can be associated with noise or small changes in temperature during the experiment.

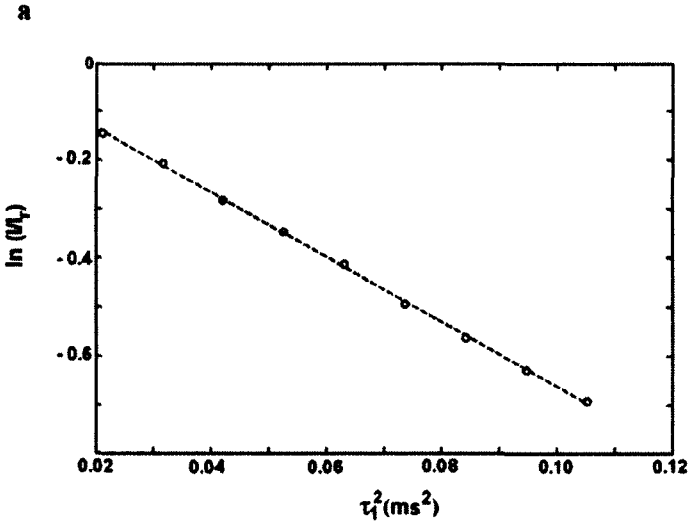

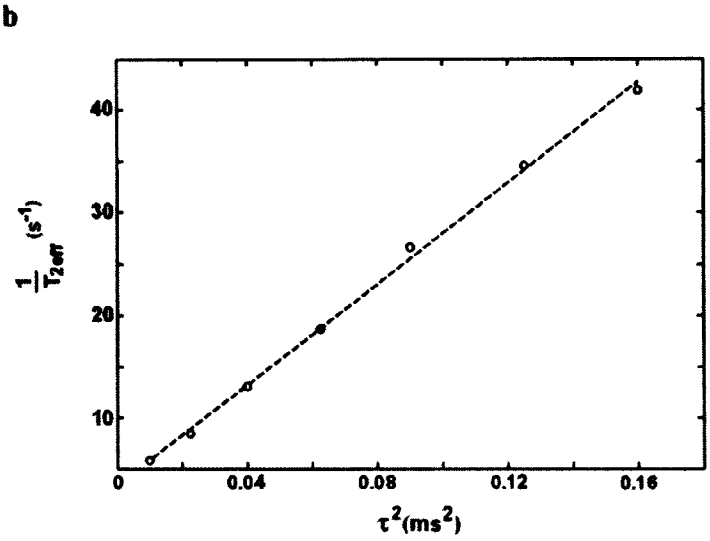

Figure 5.5. Diffusion measurement using a distilled water phantom at 24.5 mm over the magnet, assuming a diffusion coefficient of 2.07 x 10^{-9} m^2/s. The measured value of the gradient, G = 219 G/cm, for SGSTE-CPMG sequence (a) and G = 223 G/cm for CPMG with variable τ (b) agree with the magnetic field measurement (G = 218 G/cm).

Figure 5.6 presents a time-dependent diffusion coefficient measurement for two different types of rock core plugs and a reference sample of water. According to these results, fitting to Eq. 5.5, the volume to surface ratio in these rocks was determined to be around 9.7 μm for Bentheimer and 7 μm for Berea which result, assuming spherical pores, from radii of 30 μm and 20 μm respectively. These results agree with previous reports about these types of rocks in homogenous fields [30].

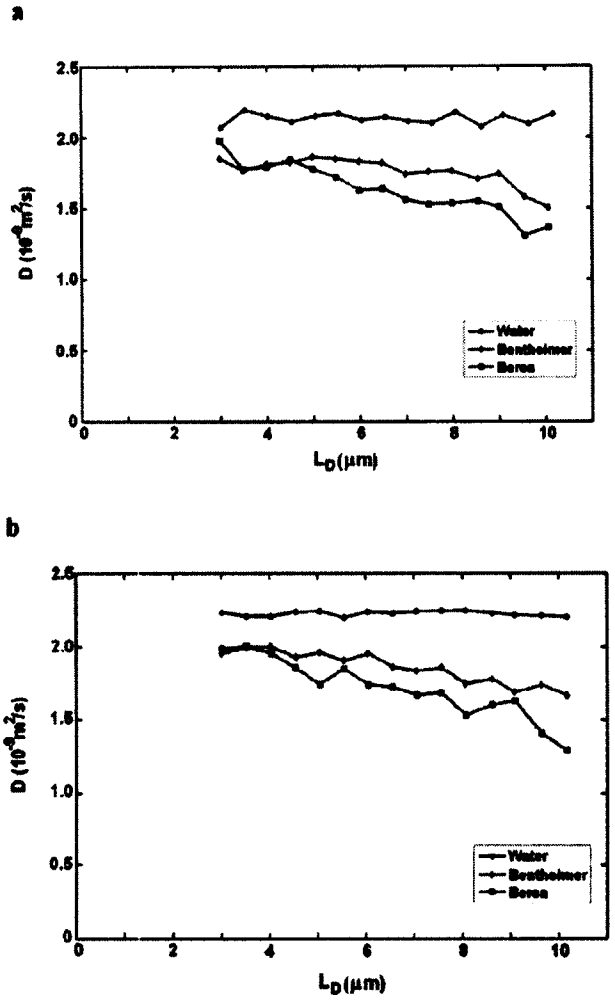

Figure 5.6. Time-dependent diffusion coefficient for two different types of rocks and a reference sample of water. Apparent diffusion coefficients for 16 different diffusion times τ_2 were measured. The measurement plane for the surface coil (a) was 5 mm deep and 1.25 cm for the solenoid (b).

A simple unilateral CPMG measurement was also undertaken to determine the porosity in both samples. For the Bentheimer rock the porosity was 28 % while for Berea it was 27 %. Table 5.1 summarizes the results of these measurements, including an estimation of T_1 for each rock core plug.

Table 5.1. Comparison of Berea and Bentheimer core plug samples

Sample	T_1 (ms)	Porosity (%)	V/S ratio (mm)	Permeability (mD)
Bentheimer	600	28	9.7	30
Berea	120	27	7	20

Measurement of the time-dependent diffusion coefficient was carried out employing a solenoid probe oriented in the x axis, with similar results (Fig. 5.6b) to those obtained with the surface coil. This type of RF probe gave us the opportunity to explore different planes inside the core plug. These planes are much deeper than those accessible to the surface coil probe. The plane position can be easily chosen by displacing the sample with respect to the magnet or by changing the RF frequency. In this last case RF probe retuning is necessary. For the measurements in Fig. 5.6 the measurement plane was 6 mm deep for the surface coil and 1.25 cm deep for the solenoid. The SNR was similar in both measurements. This result shows that the solenoid might be considered as a good choice for some specific applications in UMR. A solenoid probe can be easily built to fit specific samples or set of samples and is a natural choice for cylindrical samples.

Figure 5.7 shows a profile acquired with a small surface coil from a test phantom composed of layers of glass and silicone rubber as another example of the behavior and potential application of the extended constant gradient produced with the three-magnet array. The separation between peaks is 431 μm (40 kHz). The separation in the test phantom is 485 μm (45 kHz). A wider space between the central peaks (625 μm) can be

observed because of the presence of two layers of glass at that position. The amplitude of the peaks is modulated by the frequency response of the probe.

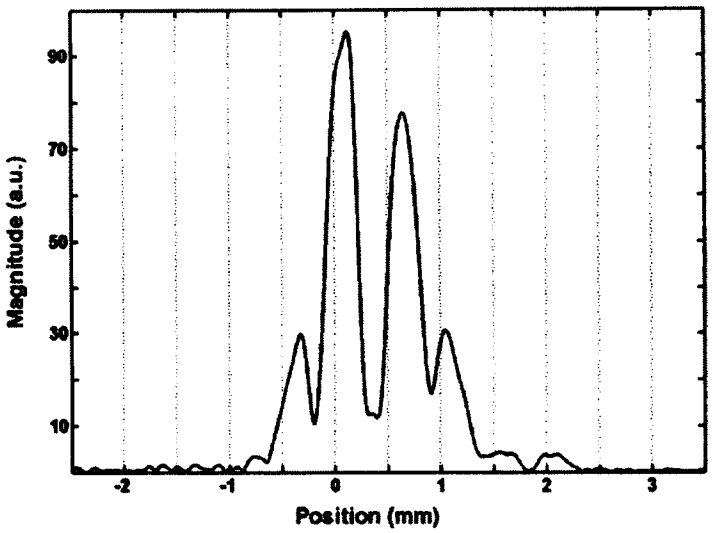

Figure 5.7. Profile obtained from a simple test phantom of glass and rubber layers. The separation between peaks is 431 μm except between the central peaks (625 μm) because of the presence of two layers of glass at that position.

One experimental goal is the use of UMR to interrogate central portions of rock core samples which may vary from 1 to 4 inch diameters. Given the rock core application, we seek a static field strength which is approximately 470 G (f_0 = 2 MHz) which is standard for rock core measurements. Figure 5.8 shows a plot of the magnetic field measured around the centre of a magnet designed for UMR constant gradient experiments at 2 MHz. In this case the gradient is 63 G/cm and the constant gradient region is 4 cm in extent, with a maximum deviation of 1 G from linear behavior. The lateral variation of the magnetic field in this case is 0.4 % in a 1 cm diameter around the centre. The reduction in the gradient value was achieved by doubling the width of the magnet blocks.

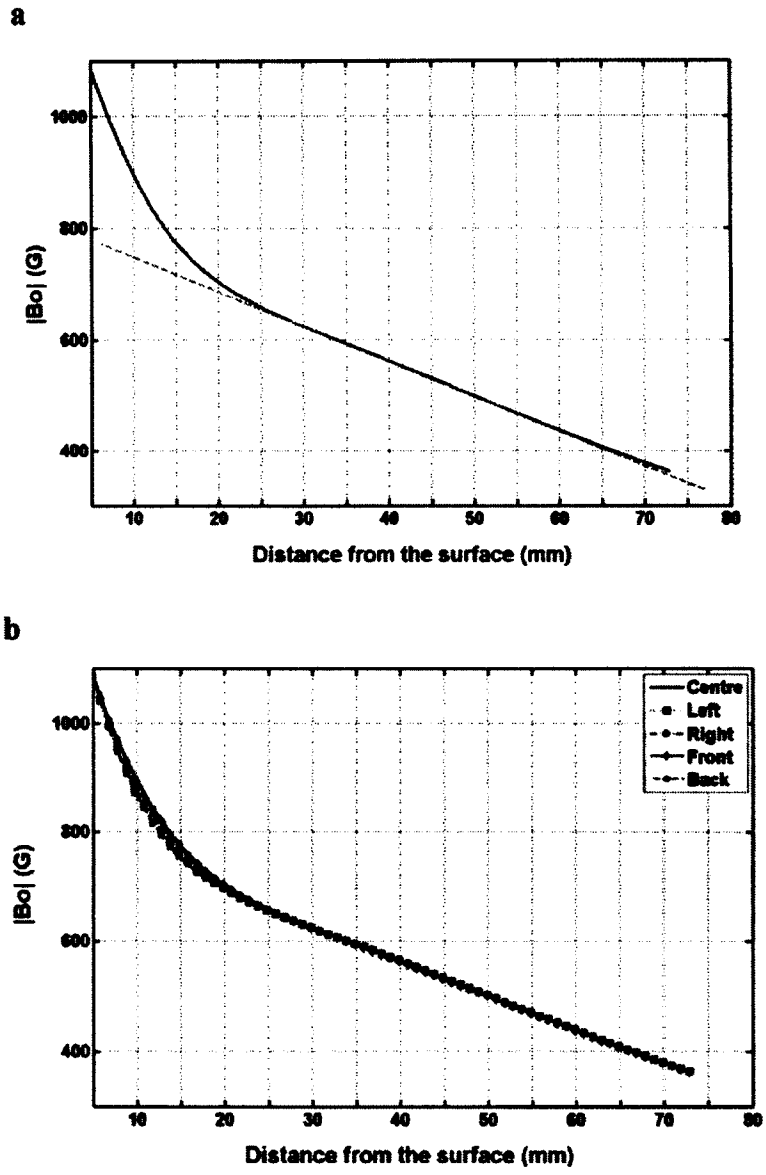

Figure 5.8. Constant gradient produced by a three-magnet array designed for a 2 MHz resonance frequency. The constant gradient of 63 G/cm and 3 cm extent are plotted in (a). The gradient for vertical lines spaced 5 mm from the centre are plotted in (b).

It is worthwhile to note that for lower gradient values, where the separation between the external blocks should be increased, a reduction in the overall magnetic field

intensity should be expected. In this case, increasing the thickness of the blocks, which means a bigger and heavier array, will increase their effective separation and produce a degree of compensation for the loss in field intensity. On the other hand, small arrays can produce higher strength gradients at higher fields but over a shorter distance. Therefore, all these factors should be taken into account to produce the best array according to the application.

5.4 Conclusions

A new and very simple way of creating constant magnetic field gradients in unilateral magnets has been introduced. Constant gradients of more than 3 cm extent can be achieved in a very simple and safe way. Diffusion measurements for different positions over the magnet employing SGSTE-CPMG, and CPMG with variable τ, have been employed to characterize the gradient employing magnetic resonance. Good agreement has been obtained with both sequences and with the magnetic field measured with a magnetic field sensor. Practical applications for core plug characterization employing a surface coil and a solenoid have been presented. The results show that the solenoid is a good candidate to explore deep inside the samples employing unilateral magnetic resonance.

5.5 Experimental

N48 NdFeB magnets (Yuxiang Magnetic Materials Ind. Co. Ltd., Xiamen, China) of 10 x 5 x 3 cm size were chosen for the external blocks. A 10 x 5 x 2 cm block was employed for the central magnet. The array was placed in an aluminum box with magnet blocks separated by 4.76 mm thick fiberglass spacers.

The magnetic field distribution along a 4.5 cm vertical line over the centre of the magnet was measured employing a three axis magnetic field probe (Lake Shore Cryotronics Inc., Westerville, USA) on a three axis plotter (Velmex Inc., Bloomfield, USA). Four additional measurements were carried out on vertical lines spaced 5 mm from the centre of the magnet to evaluate the behavior of the gradient outside the central line. Additionally, the magnetic field measured along horizontal lines in the x and z direction at 1.3, 2.3 and 3.3 cm above the magnet was also measured. The spatial resolution for each measurement was 1 mm.

In order to evaluate the gradient strength by NMR, a diffusion measurement in a distilled water sample, at heights of 15.5, 20, 24.5 and 29 mm over the magnet, was undertaken employing both SGSTE-CPMG and CPMG with variable τ. The sample container was 4 cm long with base of 1 cm on each side. It was placed in the centre of the magnet with its long dimension in the x direction. The gradient value was calculated, assuming a water diffusion coefficient of 2.07×10^{-9} m^2/s at 21 °C.

An extra diffusion measurement employing only CPMG with variable τ with the above distilled water sample at 24.5 mm from the surface was completed for comparison.

Seven data points were acquired for measuring the value of the gradient. For each data point a CPMG measurement with a different τ was carried out to determine the effective T_2 (T_{2eff}). The τ value was varied from 0.1 to 0.4 ms with an increase of 50 μs between points. The time of measurement was 40 min, which can be reduced by decreasing the number of τ values employed, the number of scans, and the repetition time.

A measurement of time-dependent diffusion coefficient was carried out employing core plugs of two different water saturated rocks (Bentheimer and Berea) and a sample of distilled water as a reference. The three samples employed for this measurement were 2.52 cm in diameter and 7.5 cm in length.

The static gradient stimulated echo sequence combined with CPMG (Fig. 5.3) and a 16 step phase table as suggested by Hurlimann [22] was employed. A reference signal at a short τ_2 (τ_{2r} = 0.5 ms) was acquired. The τ value for the CPMG part of the sequence (τ_1') was set to 80 μs for all measurements.

The number of scans was maintained at 64, with 400 echoes in the CPMG acquisition. For each diffusion measurement 9 different τ_1 values were employed. With these parameters and a repetition time of 10 s the measurement time was around 3 h. This duration may be reduced by decreasing the number of τ_1 values employed, the number of scans, and the repetition time. Additionally, employing a probe with shorter dead time would allow adding more echoes in the CPMG part of the sequence increasing the SNR and reducing the time of measurement.

For the time-dependent diffusion coefficient measurement 16 acquisitions for different τ_2 values, including the reference, were carried out. Both τ_1 and τ_2 values were chosen to obtain an equally spaced distribution of data points in all the measurements.

In order to determine the porosity of both samples a distilled water reference, same size as the core plugs, was employed. The CPMG decay for both core plugs and the reference were extrapolated to time zero. The ratio of amplitude for the core plugs and the reference expressed in percent was assumed as a measurement of porosity. Core plug measurements with 350 echoes, 128 averages and echo time of 0.2 ms, required 2 minutes for Berea and 6 minutes for Bentheimer core plug. A solenoid was employed as the RF probe.

A profile employing a small surface coil, 7 mm in diameter, was obtained from a phantom of simple layers of silicone rubber and glass. The thickness of the rubber and glass layers were 320 and 165 μm respectively. For the acquisition, a CPMG sequence with echo time of 0.2 ms and 300 echoes was employed, dwell time of 1μs. All the echoes were added to increase the SNR. A Fourier transform was applied to the resultant echo in order to obtain the profile. The measurement time was approximately 10 s.

The data acquisition was performed on a Minispec console (Bruker Analytik GmbH, Rheinstetten, Germany) with an external preamplifier (MITEQ, Hauppauge, USA). A surface coil of 2 cm diameter was employed for both radiofrequency transmission and reception. For measurements of the core plugs a solenoid probe of 3 cm in diameter, 3 cm long, was also employed. The pulse length was maintained at the same

value for the RF pulses, with the maximum output power (250 W) for the 180°, in all the measurements. For the surface coil the pulse length was 5 μs and 4.2 μs for the solenoid. For the small surface coil employed for profiling, the pulse length was 2 μs.

Acknowledgements

JCG and BJB thank the Atlantic Innovation Foundation and ACOA for supporting this work. Saudi Aramco and Green Imaging Technologies are also thanked for sponsorship. BJB thanks NSERC for a Discovery grant and the Canada Chairs program for a research chair in MRI of materials.

References

[1] J. C. García-Naranjo, I. V. Mastikhin, B. G. Colpitts, B. J. Balcom, A unilateral magnet with an extended constant magnetic field gradient, J. Magn. Reson. 207, 337- 344, 2010.

[2] R.L. Kleinberg, A. Sezginer, D.D. Griffin, M. Fukuhara, Novel NMR apparatus for investigating an external sample, J. Magn. Reson. 97, 466–485, 1992.

[3] R. Haken, B. Blumich, Anisotropy in Tendon Investigated in Vivo by a Portable NMR Scanner, the NMR-MOUSE, J. Magn. Reson. 144, 2, 195-199, 2000.

[4] P.F. de J. Cano-Barrita, A.E. Marble, B.J. Balcom, J.C. García, I.V. Masthikin, M.D.A. Thomas, T.W. Bremner, Embedded NMR sensors to monitor evaporable water loss caused by hydration and drying in Portland cement mortar, Cem. Concr. Res. 39, 324–328, 2009.

[5] S. Rahmatallah, Y. Li, H.C. Seton, I.S. Gregory, R.M. Aspden, Measurement of relaxation times in foodstuffs using a one-sided portable magnetic resonance probe, Eur. Food Res. Technol. 222, 298–301, 2006.

[6] G. Eidmann, R. Savelsberg, P. Blumler, B. Blumich, The NMR MOUSE, a mobile universal surface explorer, J. Magn. Reson. A 122, 104–109, 1996.

[7] W.H. Chang, J.H. Chen, L.P. Hwang, Single-sided mobile NMR with a Halbach magnet, Magn. Reson. Imaging 24, 1095–1102, 2006.

[8] E. Fukushima, J. A. Jackson. Unilateral magnet having a remote uniform field region for nuclear magnetic resonance. U.S. Patent 6,489,872, 2002.

[9] J.A. Jackson, L.J. Burnett, J.F. Harmon, Remote (inside-out) NMR. III. Detection of nuclear magnetic resonance in a remotely produced region of homogeneous magnetic, J. Magn. Reson. 41, 411–421, 1980.

[10] A. E. Marble, I. V. Mastikhin, B. G. Colpitts, B. J. Balcom, An analytical methodology for magnetic field control in unilateral NMR. J. Magn. Reson. 174, 78–87, 2005.

[11] A. E. Marble, I. V. Mastikhin, B. G. Colpitts, B. J. Balcom, A compact permanent magnet array with a remote homogeneous field. J. Magn. Reson. 186, 100–104, 2007.

[12] J. Perlo, F. Casanova, B. Blumich, Ex situ NMR in Highly homogeneous fields: ^{1}H spectroscopy. Science, 315, 1110-1112, 2007.

[13] P.J. Prado, One-dimentional imaging with palm-size probe. J. Magn. Reson. 144, 200–206, 2000.

[14] B. Blumich, V. Anferov, S. Anferova, M. Klein, R. Fechete, M. Adams, F. Casanova, Simple NMR-mouse with a bar magnet, Conc. Magn. Reson. B 15, 255–261, 2002.

[15] F. Casanova, B. Blumich, Two-dimensional imaging with a single-sided NMR probe, J. Magn. Res. 163, 38–45, 2003.

[16] J. Perlo, F. Casanova, B. Blumich, 3D imaging with a single-side sensor: an open tomograph, J. Magn. Reson. 166, 228–235, 2004.

[17] J. Perlo, F. Casanova, B. Blumich, Profiles with microscopic resolution by single-sided NMR, J. Magn. Reson. 176, 64–70, 2005.

[18] P. J. McDonald and B. Newling, Stray field magnetic resonance imaging, Rep. Prog. Phys. 61, 1441–1493, 1998.

[19] A. E. Marble, I. V. Mastikhin, B. G. Colpitts, B. J. Balcom, A constant gradient unilateral magnet for near-surface MRI profiling. J. Magn. Reson. 183, 228–234, 2006.

[20] J.C. García-Naranjo, B. J. Balcom, I. V. Mastikhin, B. G. Colpitts, Three-magnet array for Unilateral Magnetic Resonance, 9th colloquium of mobile NMR, August 30 – September 4, Montana, USA, 2009.

[21] R. Kimmich, E. Fischer, One- and Two-dimensional pulse sequences for diffusion experiments in the fringe field of superconducting magnets. J. Magn. Reson. Series A 106, 229-235, 1994.

[22] M.D. Hurlimann, L. Venkataramanan, Quantitative measurement of two- dimensional distribution functions of diffusion and relaxation in grossly inhomogeneous fields. J. Magn. Reson. 157, 31-42, 2002.

[23] L. J. Zielinski, M. D. Hurlimann, Short-time restricted diffusion in a static gradient and the attenuation of individual coherence pathways. J. Magn. Reson. 171, 107-117, 2004.

[24] R. Kimmich, W. Unrath, G . Schnur, E. Rommel, NMR measurement of small self-diffusion coefficients in the fringe field of superconducting magnets, J. Magn. Reson. 91, 136-140, 1991.

[25] M. D. Hurlimann, D. D. Griffin, Spin Dynamics of Carr-Purcell-Meibon-Gill-like sequences in grossly inhomogeneous B_0 and B_1 fields and application to NMR well logging, J. Magn. Reson. 143, 120-135, 2000.

[26] D.G. Rata. F. Casanova, J. Perlo, D.E. Demco, B. Blumich, Self-diffusion measurement by a mobile single-side NMR sensor with improved magnetic field gradient. J. Magn. Reson. 180, 229-235, 2006.

[27] G. Laicher, D. C. Ailion, A. G. Cutillo, Water Self-diffusion measurement in excised rat lungs, J. Magn. Reson. Series B 111, 243-253, 1996.

[28] M. L. Buess, G. L. Petersen, Acoustic ringing effect in pulsed nuclear magnetic resonance probes. Rev. Sci. Instrum. 49, 1151-1155, 1978.

[29] E. Fukushima, S. B. W. Roeder, Spurious ringing in pulse NMR, J. Magn. Reson. 33, 199-203, 1979.

[30] H. Liaw. R. Kulkarni, S. Chen, T. Watson, Characterization of fluid distributions in porous media by NMR techniques. AIChE J. 42, 538-546, 1996.

Chapter 6

Magnetic Resonance core plug analysis with the three-magnet array.

Magnetic Resonance has a long history of applications in the petroleum industry due to the sensitivity of the NMR experiment to the fluids water, oil and gas which occupy the pore space of the rock matrix. We can distinguish two general classes of experiments and instruments. The first class involves the downhole NMR tools (Fig. 6.1) mentioned earlier in this thesis. In this class of measurement one has an instrument lowered into a borehole in the field with a sensitive spot displaced into the rock matrix [1, 2, 3]. A variety of MR measurements can be undertaken to determine the local porosity, the type of fluids present, the mobility of the fluids and the pore size distribution [4, 5, 6, 7].

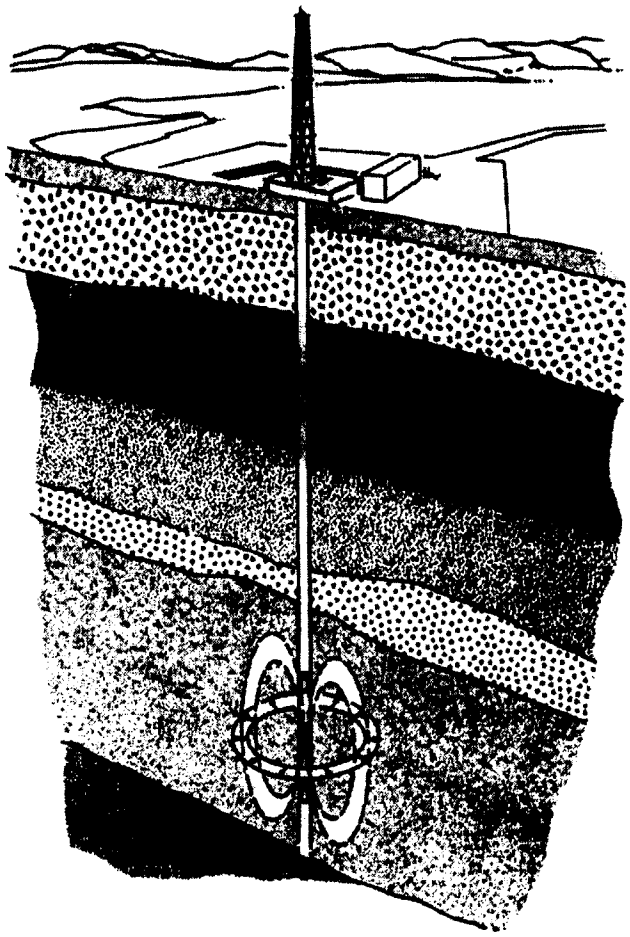

Figure 6.1. Downhole NMR tool [1]. The sensitive spot of the instrument is inside the rock matrix.

These measurements rely on the quantitative nature of the MR experiment where the signal amplitude, neglecting relaxation time effects, is proportional to the quantity of ^1H bearing fluids. These results also exploit the ability of CPMG echo measurements to measure a T_2 distribution which is well known to be an excellent proxy measurement for the fluid occupied pore size distribution.

The second class of MR core analysis measurement is a benchtop measurement of smaller core plugs extracted from reservoir cores drilled as part of an exploration or production program. These core plugs may then be examined in a laboratory measurement, usually with low field permanent magnet based instruments (Fig. 6.2).

Such instruments, common in the core analysis field, are based on closed magnets where the core plug is placed into the magnet structure for measurement. For this type of magnet it can be problematic to measure long core plugs like those obtained from the drilling process during the exploration of reservoirs. These magnets are also clearly limited in the sample diameter that can be accommodated.

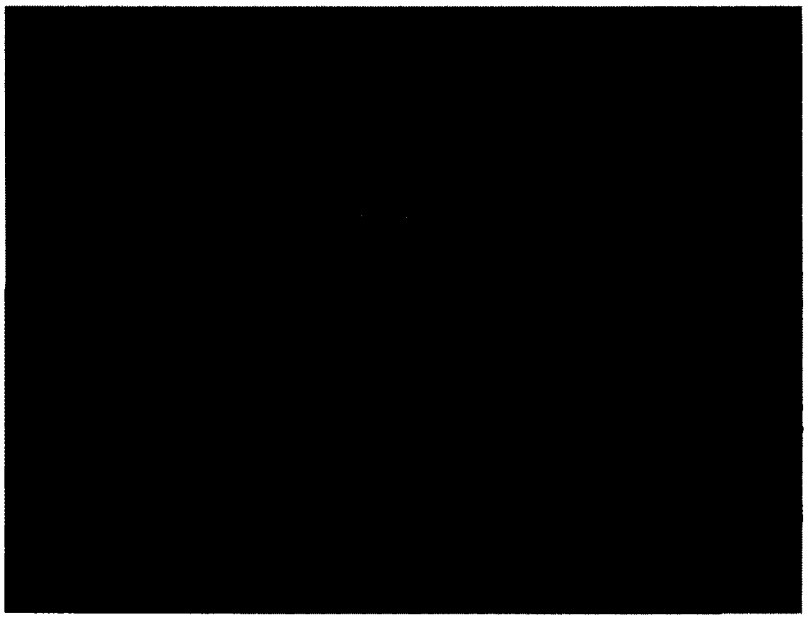

Figure 6.2. Closed permanent magnet employed for core plug analysis in the laboratory.

This chapter presents a new approach for this second class of measurements, employing a three-magnet array with a solenoid as the RF probe. The three-magnet array WA-1 (Section 3.3.2), with a homogeneous spot centered at a frequency of 2.25 MHz, and WA-2 with an extended constant gradient, centered at the same frequency, were employed. This frequency is similar to the value employed by the MR benchtop instrument previously described for core plug analysis in the laboratory. The 2 MHz frequency is a worldwide standard for NMR core analysis. Higher fields and frequencies introduce significant internal magnetic field gradients [8] in the pore space, which artificially change the T_2 distribution (see Eq. 2.15).

Figure 6.3. Three-magnet array WA-2, similar in size and weight to WA-1 (see Fig. 3.16), surface coil and solenoid RF probes for measuring core plugs of 1.5, 2.5 and 3.5 inches.

Core plugs of different diameters can be measured employing solenoids of different diameters as the RF probe. In fact, a set of solenoids of different diameters can be readily built according to the core plug diameters to be measured. The measurement concept is similar to well logging NMR instruments (sample is removed from the magnet), but in this case the experiment is undertaken in the laboratory with a simple device. The measurement is undertaken from a specific spot inside the core plug (see Fig. 6.4), which avoids any signal from the surface. As mentioned in Section 3.3.2 the near surface region is affected by the cutting tools and therefore does not produce reliable information about the core plug. As shown in this chapter, despite the simplicity, the UMR measurement yields reliable results.

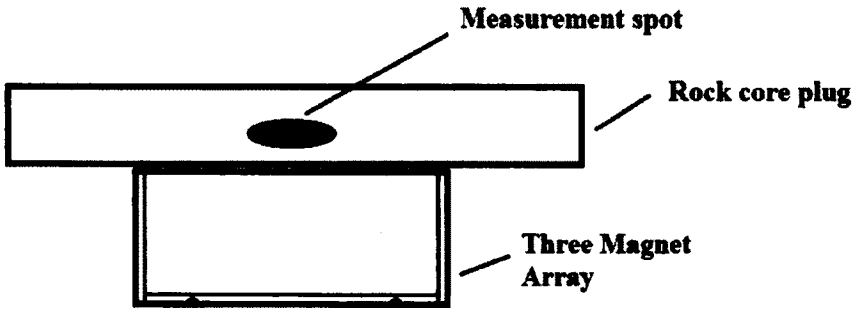

Figure 6.4. Schematic of the measurement employing the three-magnet array. The measurement in undertaken from a specific spot inside the core plug.

For this approach there is no limitation on the length of the core plugs that can be studied. Long core plugs can be analyzed by displacing the core plug inside

the probe. Equivalently the magnet and RF probe may be displaced along the core plug. In this way longitudinal profiles of different parameters can be obtained.

The laboratory basis of this measurement means it is difficult to measure cores and core plugs maintained under reservoir conditions. If the core or core plug has been depressurized, gas will appear as a separate phase in the fluid. In the language of core analysis we have dead oil rather than live oil. Cores and core plugs extracted from relatively shallow reservoirs, as found in many parts of the Middle East are however amenable to this type of testing. In many cases in this region cores are extracted and simply cased in a plastic sleeve. These samples are particularly amenable to screening by the laboratory methods outlined in this chapter.

A similar laboratory measurement approach has been proposed by Anferova et al. [9] based on a Halbach magnet design [10]. In this case the magnet encompasses the sample and is displaced along the core plug to obtain a porosity profile along the sample (Fig. 6.5). This approach produces good results and is probably less expensive than classic NMR benchtop scanners. Nevertheless, the adjustment process for the Halbach magnet can be troublesome and time consuming. The fixed diameter of the magnet bore clearly restricts the diameter of core plug that can be studied. Larger core plug diameters require building a new magnet which, as mentioned before, is not a simple process. Measurements employing Halbach magnets yield information about the full sample cross section, including regions close to the surface. In the Halbach magnet designs the introduction of magnetic field gradients, for spatial encoding or motion encoding, requires the introduction of

magnetic field gradient coils and gradient amplifiers. This vastly increases the complexity of the instrument.

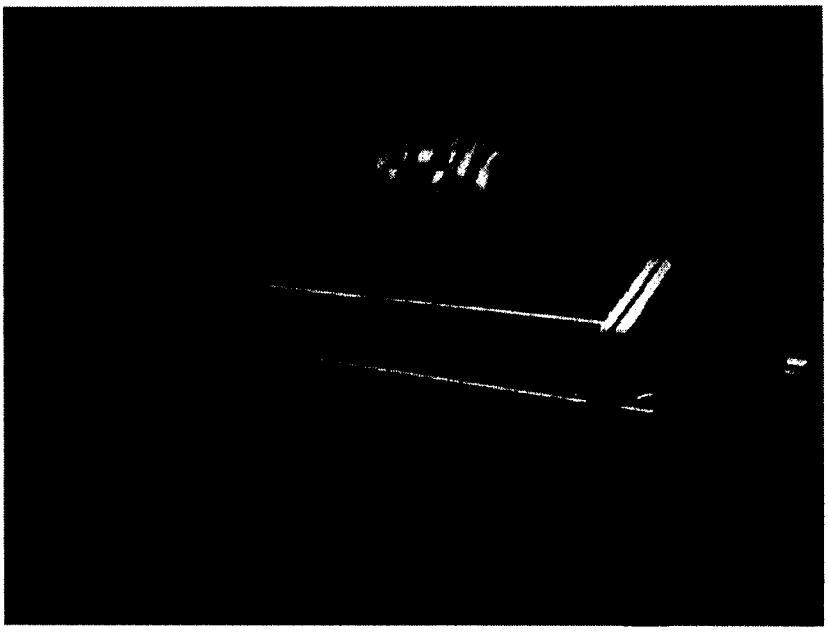

Figure 6.5. Halbach core scanner introduced by Anferova et al. in [9]. The core plug diameter that can be studied is limited by the size of the magnet bore.

This chapter presents the results of porosity profile and T_{2eff} distribution measurements employing a three-magnet array with a solenoid as the RF probe. We show that, despite the low cost and simplicity of the magnet, reliable results are produced. An additional comparison of the behavior of a surface coil and solenoids of different diameters is also included.

6.1 Choosing the RF probe

A near surface UMR measurement of core plugs should be avoided in order not to measure the near surface region affected by the cutting tools (see Section 3.3.2). A deeper sensitive spot is required. This requirement is a challenge for a surface coil. The rapid decay of B_1 with distance from the coil requires the employment of high power and/or long duration RF pulses in order to excite the desired region properly. Both factors can be troublesome. High power RF pulses require high quality capacitors for tuning the RF probe in order to avoid electric arcing during the excitation. Long duration RF pulses reduce the excited spot size compromising SNR during reception.

For the three-magnet array a solenoid can be employed as the RF probe. The solenoid, in addition to a more homogeneous B_1, presents higher sensitivity than the surface coil for deeper regions. Nevertheless, for large diameter core plug samples the necessity of higher power or longer RF pulses can produce the same undesirable effects described for the surface coil. The small size of the spot in comparison with the probe diameter, can also compromise the SNR during the experiment.

As a first step, a comparison among three solenoids of different diameters and a 3 cm diameter surface coil was undertaken. All the UMR measurements were carried out with a portable LapNMR console from Tecmag, connected to a 250W RF power amplifier from TOMCO Technologies and a MITEQ preamplifier. The three-magnet array WA-1 with a homogeneous spot was employed for these tests.

Three solenoids of 4.2 (sol15), 7 (sol25) and 9.5 cm (sol35) diameter and 2 cm length and a surface coil (sc) of 3 cm diameter (Fig. 6.3), were built for measuring core plugs of 1.5, 2.5 and 3.5 inch diameter.

All probes were adjusted to have a loaded Q factor of 22. For sol15 the tuning frequency and the Q were verified, once the sample was placed inside the probe. The tuning frequency changed by 4 kHz and no change of the Q was observed. Three Bentheimer core plugs, fully saturated with brine (2%), of 1.5, 2.5 and 3.5 inch diameter were employed as initial test samples. Single echo spin-echo measurements, with RF pulses of the same duration and echo time of 500 μs, were employed for initial testing. The voltage for the 90° RF pulse was set at one half of the voltage for the 180° RF pulse. Table 6.1 shows the results of these measurements.

Table 6.1. Result of the comparison of different probes for core plug analysis

sc	3	14	175
sol15	4.2	8	1553
sol25	7	16	940
sol35	9.5	20	495

As can be observed even the largest radius solenoid produces more signal than the surface coil. The surface coil was tested with the 1.5 inch diameter sample only. The pulse length for the surface coil is less than for the sol25 and sol35

solenoids, which means a higher B_1 for equivalent power. The smaller signal for the surface coil can be associated with the fact that, because of the rapid decay of B_1 with distance, only thin layers of the sample are excited with the proper B_1. For the solenoid the entire sensitive spot is excited with the same B_1 and therefore more signal is available during reception. The level of noise was similar for all acquisitions.

6.2 Exploring deep layers inside the core plug

The more homogeneous B_1 from the solenoid, permits measurement of deeper layers inside the core plug than can be reached with a surface coil. For the following experiment two solenoids (sol25 and sol35) and the surface coil were employed with the three-magnet array WA-2, which has similar dimensions and weight as WA-1 but features a constant gradient of 60 G/cm over a distance of more than 4 cm from the surface. Figure 6.6 shows the magnetic field distribution along the vertical central line of the array.

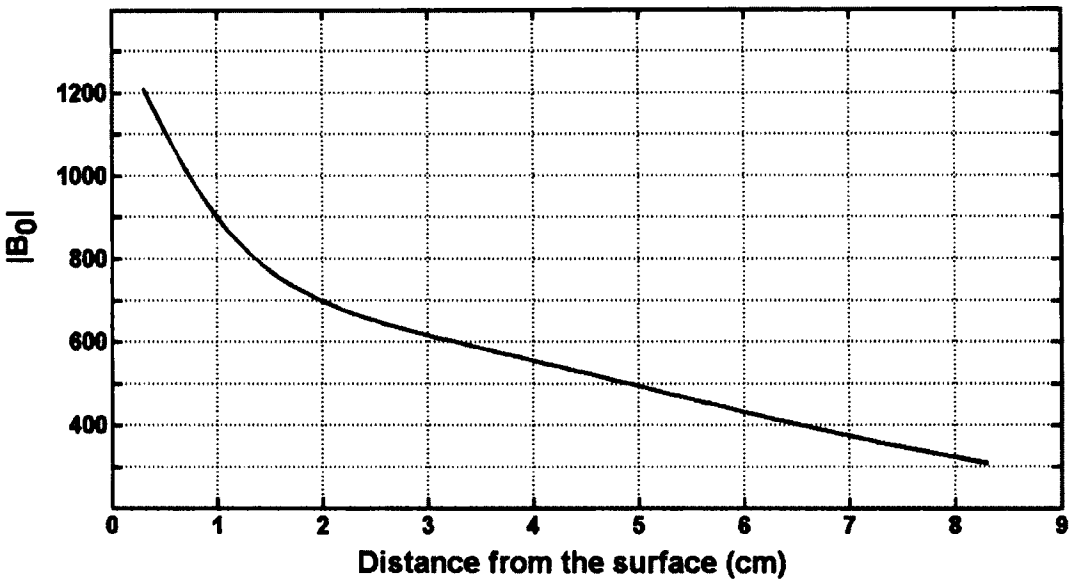

Figure 6.6. Magnetic field along the vertical central line of the three-magnet array WA-2. The strength of the constant gradient is 60 G/cm in the region from 2.5 to 7 cm.

The extended constant gradient in combination with the solenoid allows selection of deeper spots inside the core plug through appropriate choice of the MR resonance frequency. Table 6.2 shows the amplitude of the echo signal obtained from the centre of three Berea core plugs of different diameters with a single echo spin-echo sequence. The sol15 solenoid was not employed for this measurement because the centre of the core plug is 2 cm inside the core plug, which is closer than the position of the homogenous spot previously explored in Section 6.1. The depth of the measurement spot was measured from the surface of the core plug. The surface of the core plug is 4 mm form the magnet surface (see Fig. 6.6).

Table 6.2. Comparison of the signal obtained with the surface coil and two solenoids exploring deep layers inside the core plug.

Position of the spot (cm)	Probe	Echo signal
3	sc	-
	sol25	305
4.5	sc	-
	sol35	260

For the surface coil the RF pulse was varied in duration from 10 to 50 μs, but it was impossible to obtain any signal from the centre of the core plugs. This means that for the surface coil the limit of depth that can be studied is around 2 cm. This result shows that the solenoid is a better choice to explore deep layers inside the core plugs. For these experiments the number of scans was increased to 1024 because of the reduced signal amplitude. The echo time was 500 μs and the time of measurement 35 min. The presence of the gradient reduces the size of the spot in comparison to the homogeneous spot version WA-1. From Fig. 3.15 and Fig. 6.6 it can be observed that for a probe with 100 kHz of bandwidth ($Q_L = 20$) and RF pulses less than 10 μs the measurement spot is reduced in the vertical direction (y) from a width of 1.5 cm to 0.4 cm by the constant gradient. In the horizontal directions (x, z) the spot remains the same size.

6.3 Measuring porosity in long core plug samples.

For these measurements, four different rock core plugs (Table 6.3) saturated with brine (2 %) were analyzed. The porosity was determined by back extrapolating the T_{2eff} decay obtained from a CPMG measurement calibrated by a reference sample.

Table 6.3. Rock core plugs employed for the measurements

	Core plug	Length (cm)	Porosity (%)
1	Berea gray sandstone	11	21
2	Indiana limestone	10.5	14
3	Bentheimer sandstone	7.5	21
4	Nugget sandstone	11	15

Long core plugs were imitated by employing composite core plug samples (CPS), built by combining four core plugs of the same diameter and different porosities (Fig. 6.7). Three CPSs were created of 1.5 (CPS15), 2.5 (CPS25) and 3.5 (CPS35) inch diameter. The core plugs were placed inside the CPS in the same order they are presented in Table 6.3.

Figure 6.7. Composite core plug sample (CPS) of 2.5 inch diameter created from individual core plugs of different types of rocks.

The CPS was longitudinally displaced inside the RF probe in steps of 1 cm for CPS15 and 2 cm for CPS25 and CPS35. At each spatial point a CPMG measurement was undertaken. For each CPMG echo 128 time domain points were acquired. The first point of the CPMG decay was determined as the maximum of the first echo. Subsequent CPMG points were measured at multiples of the echo time (500 μs). The repetition time TR = 5 s was set according to the T_1 of the Bentheimer core plug which is the longest T_1 in the CPS. The number of scans was 128, 256 and 512 for CPS15, CPS25 and CPS35 respectively. The measurement durations at each position of the CPS were 12 min, 25 min and 50 min respectively. The RF pulse lengths were set according to Table 6.1. The Berea core plug with porosity of 21 % was employed as the reference sample.

Figure 6.8 shows a typical CPMG decay obtained during the porosity measurement from CPS15.

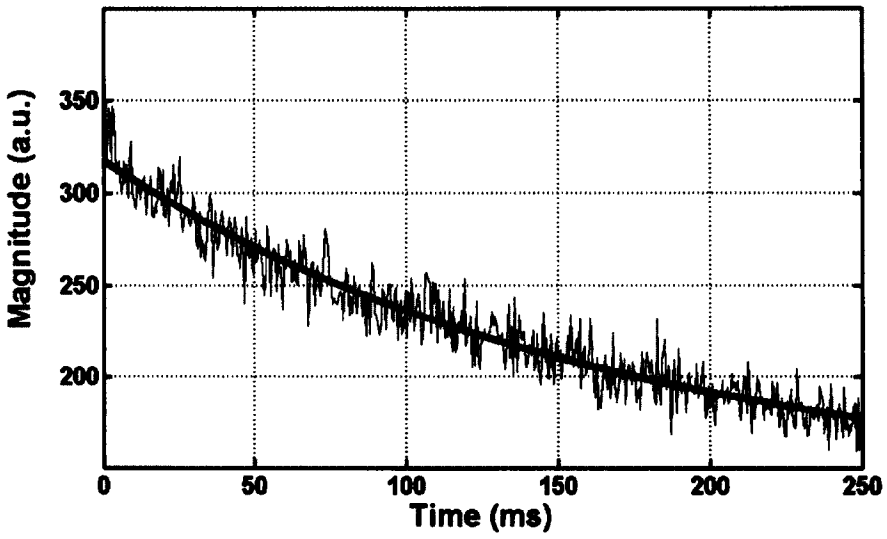

Figure 6.8. CPMG decay from the section corresponding to Bentheimer sandstone in the CPS.

Figure 6.9a shows the porosity profile obtained from CPS15. All the reported porosity values were obtained employing a Berea sandstone core plug (21 % porosity) as the reference. The dashed vertical lines represent the limits of the different core plugs inside the CPS. As stated previously, each measurement point is separated by 1 cm. As can be observed there is a clear discrimination of porosity inside the CPS. The porosity for the first and last point of the profile has been underestimated because the portion of the CPS is smaller than the sensitive volume of the probe and therefore smaller than the reference. The sharpness of the transition bands has been affected by the length of the sensitive spot of the probe (2 cm).

A T_{2eff} profile of the CPS is presented in Fig. 6.9b. All CPMG decays were fit to a single exponential function even in the transition regions where double exponential behavior was expected. The T_{2eff} value for one point in the Bentheimer region of the CPS, 24 cm, seems to be in error.

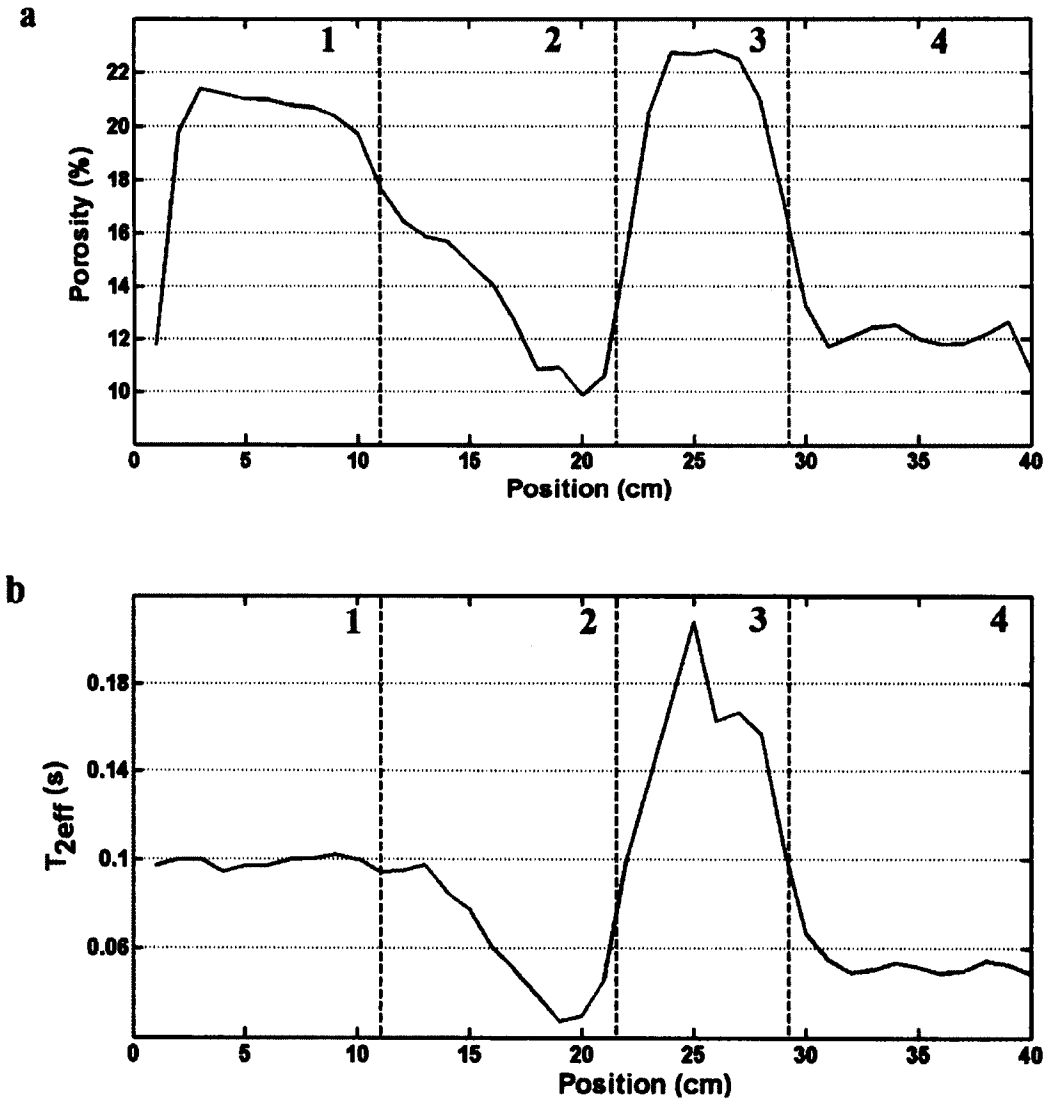

Figure 6.9. Porosity (a) and T_{2eff} (b) profiles measured employing the three-magnet array along CPS15. The error during the estimation of the profile amplitude is less than 1 % in porosity units. For the T_{2eff} profile the error

is 3 %. The dashed lines and the numbers in the top part of the figure represent the position of the core plugs in the CPS (see Table 6.3).

Special attention should be directed to the section of the CPS corresponding to the Indiana Limestone core plug (number 2). The distribution of porosity was expected to be flat as for the other core plugs but the data of Fig. 6.9a suggests the presence of significant inhomogeneities along the sample. In order to confirm this behavior, a porosity profile was obtained with a spin-echo measurement in a homogeneous field 8 MHz MARAN DRX HF scanner. Figure 6.10 shows the porosity profile obtained. As can be observed there is a good agreement with the results obtained with the three-magnet array.

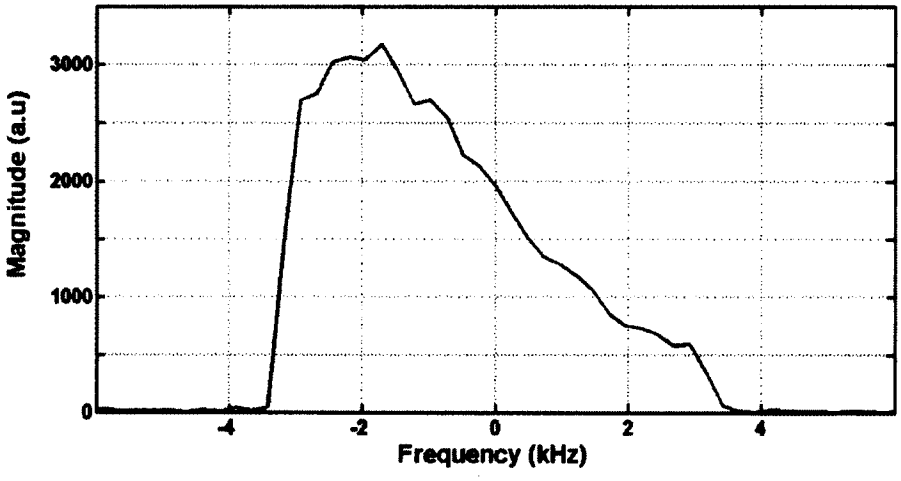

Figure 6.10. Porosity profile obtained with a spin-echo measurement in a homogeneous field magnet for the Indiana limestone. This result agrees with the profile obtained in Fig. 6.9a for the section of the Indiana core plug.

Porosity profiles were also obtained for CPS25 and CPS35. These types of long core plugs are usually more difficult to measure in closed magnets because of their large diameter. Figure 6.11 shows a representative CPMG measurement obtained from each CPS with the three-magnet array and the solenoids sol25 and sol35 respectively.

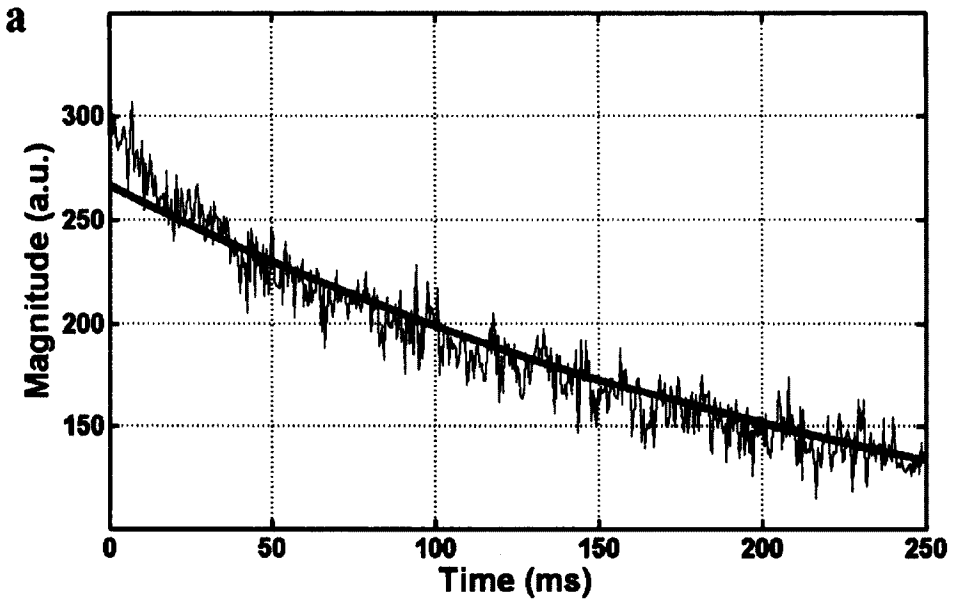

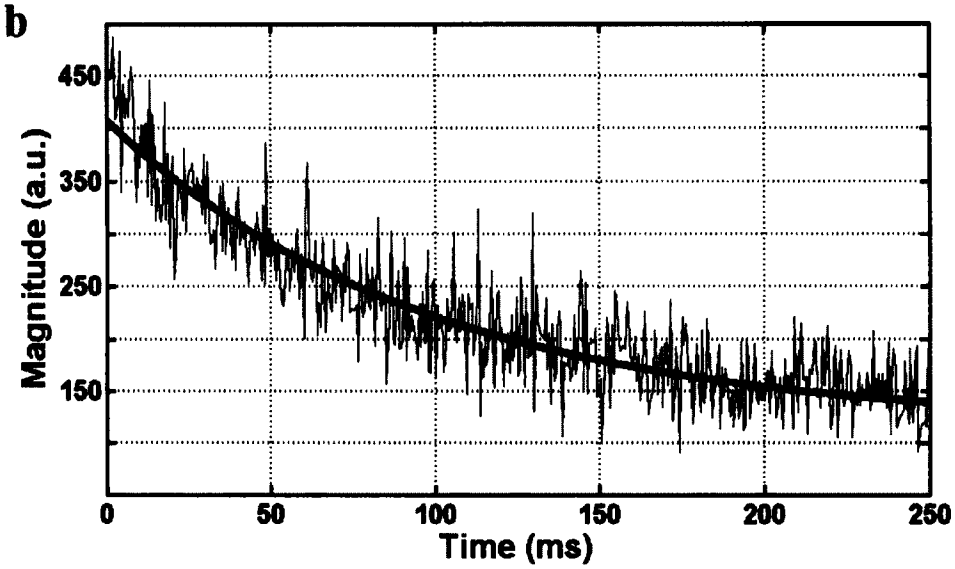

Figure 6.11. CPMG decays obtained from CPS25 (a) and CPS35 (b).

Figure 6.12 shows the porosity and T_{2eff} profile for CPS25 and Fig. 6.13 for CPS35. In these cases the separation between successive measurement points was 2 cm.

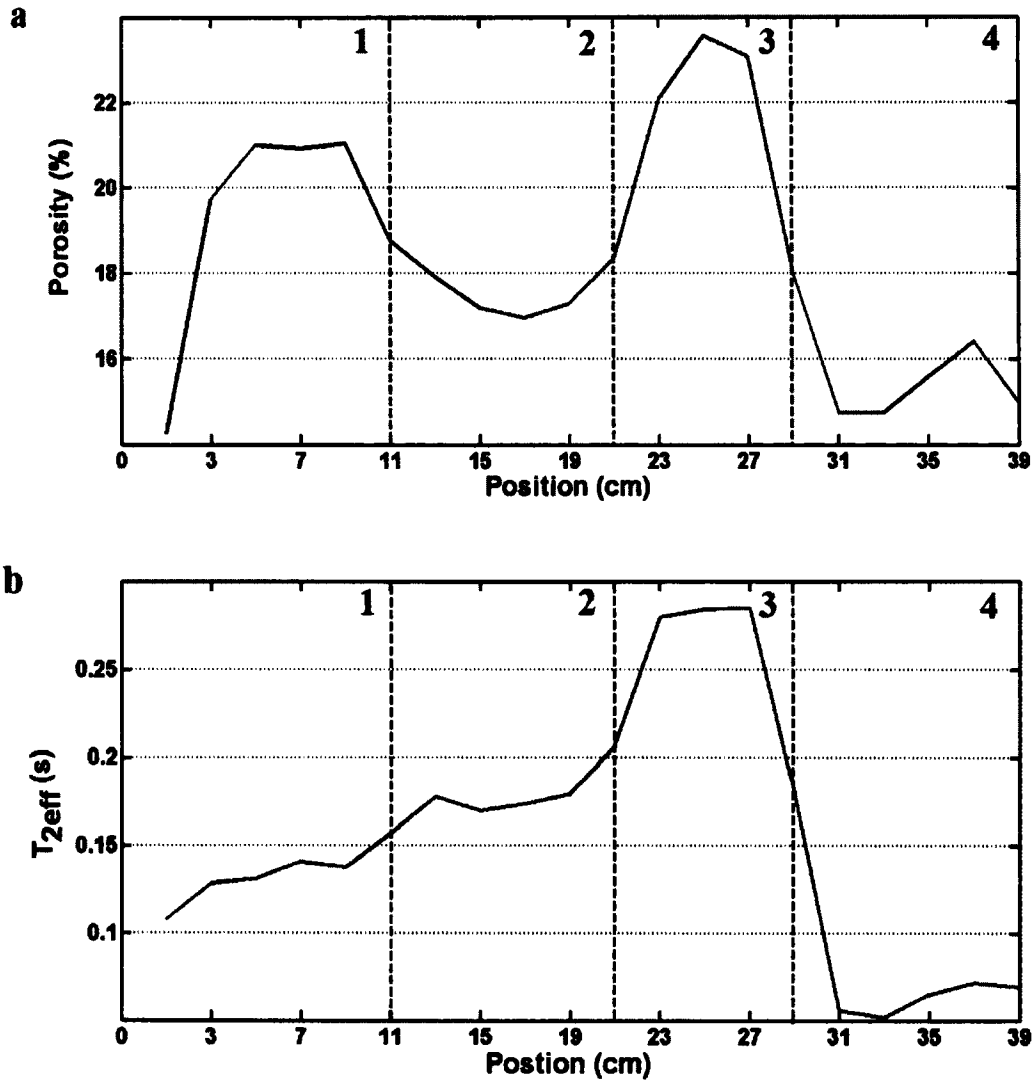

Figure 6.12. Porosity (a) and T_{2eff} (b) profiles of CPS25 obtained with the three-magnet array. The dashed lines and the numbers in the top part of the figure represent the position of the core plugs in the CPS (see Table 6.3).

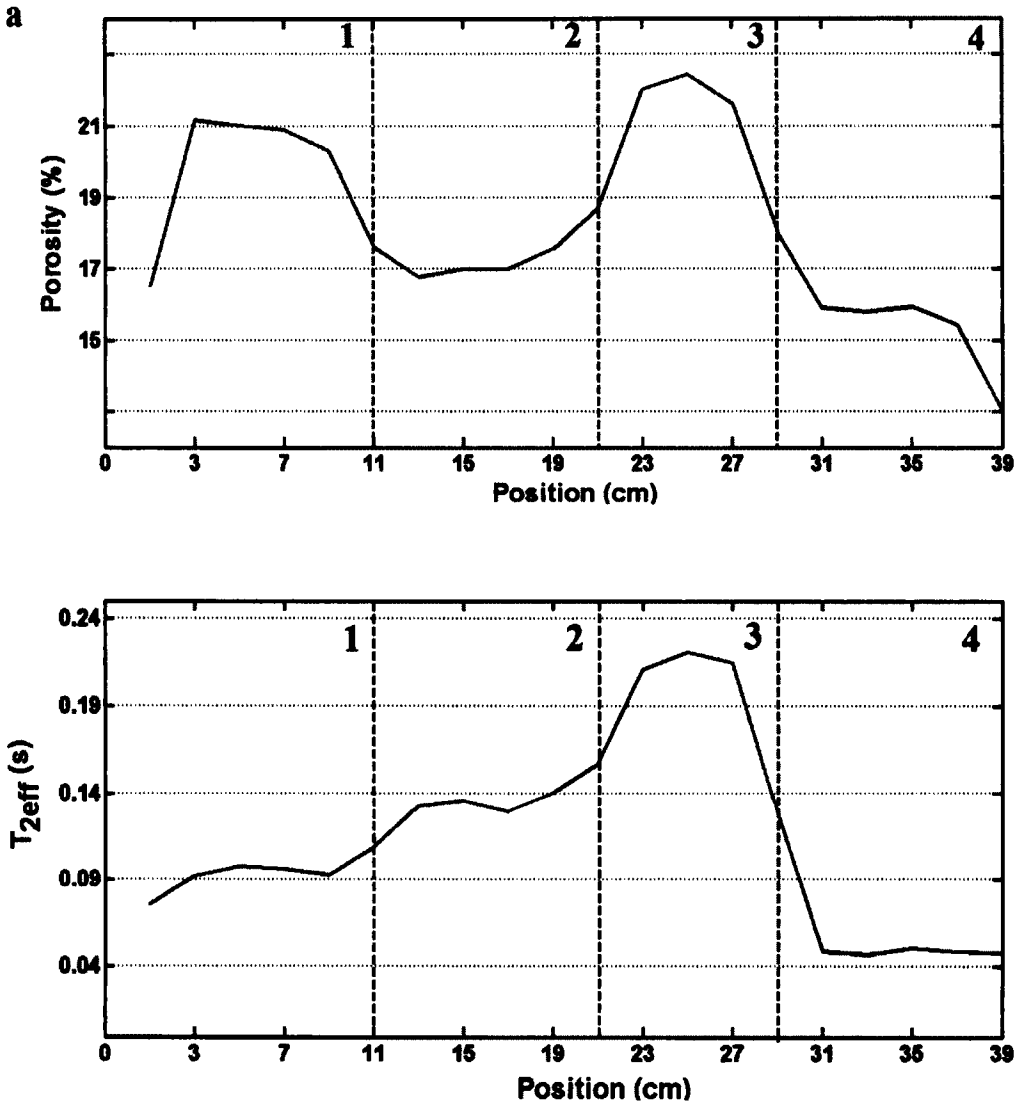

Figure 6.13. Porosity (a) and T_{2eff} (b) profiles of CPS35 obtained with the three-magnet array. The dashed lines and the numbers in the top part of the figure represent the position of the core plugs in the CPS (see Table 6.3).

The profile variation in the Indiana limestone section is the result of inhomogeneities in this core plug, as was shown for the 1.5'' sample (CPS15). Figure 6.14 shows T_2 distributions obtained from different transverse planes of the Indiana limestone core plug measured employing the spin-echo SPI method in an 8

MHz homogenous magnet with a MARAN DRX HF console from Oxford Instruments. These inhomogeneities explain the differences in the profiles.

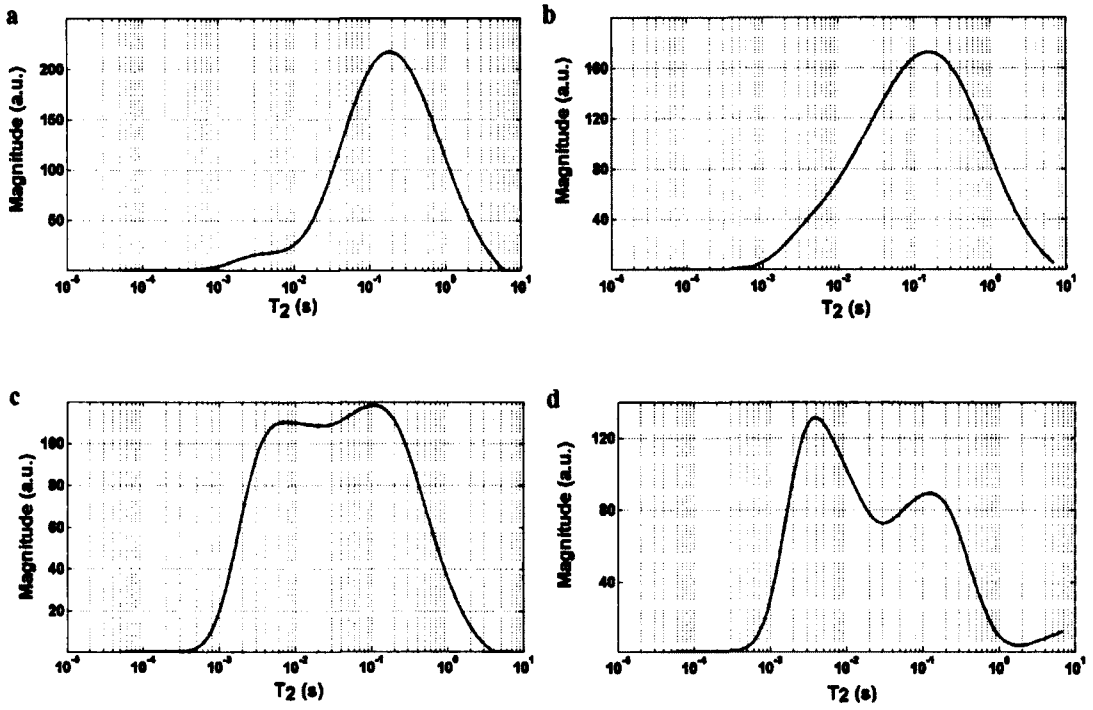

Figure 6.14. T_2 distribution, spatially resolved, measured for transverse planes at 1 cm (a), 4 cm (b), 7 cm (c) and 9 cm, along the longitudinal axis of the Indiana core plug. The variations with position show the sample is substantially inhomogeneous.

6.3.1 Measuring different fluids in the pore space of a core plug employing the three-magnet array.

Evaluating the fluids inside a core plug is another important test in core analysis. For this experiment, two different water/oil ratios were evaluated in a 1.5'' diameter Berea core plug. A new solenoid of 2'' diameter (sol20) was employed for this experiment in order to measure the core plug inside a core holder. The core plug,

firstly saturated with brine (2 %), was flooded with the oil phase, dodecane, at a flow rate of 0.3 ml/min. After three hours, the total production of water was 11.7 ml. The water saturation (S_w) was thus 59.9 % and the oil saturation (S_o) was 40.1 %. In a second experiment the flow rate was increased to 10 ml/min. After two hours, the total production of water was 17.1 ml. The water saturation (S_w) in this case was 41.8 % and the oil saturation (S_o) was 58.2 %. For both samples a 256 scan CPMG acquisition was undertaken in a uniform spot unilateral magnet WA-1 with echo time of 500μs and 2000 echoes. The RF pulse length was 12 μs. The time of measurement was 5 min. For comparison, after each experiment the same sample was measured in a 2 MHz homogeneous magnet with a MARAN Ultra console from Oxford Instruments.

Figure 6.15 illustrates the T_2 distribution for the full brine saturated (dotted), the first (dashed) and the second (solid) water/oil ratio sample. Figure 6.15a represents the T_2 distribution for the measurements in homogeneous field and Fig. 6.15b for the three-magnet array WA-1. The T_2 distribution was processed by inverse Laplace transformation of the CPMG echo train. For the measurement with the three-magnet array the CPMG echo train was acquired from the centre of the core plug. For the experiment with the 2 MHz desktop Maran Instrument the measurement was from the entire core plug.

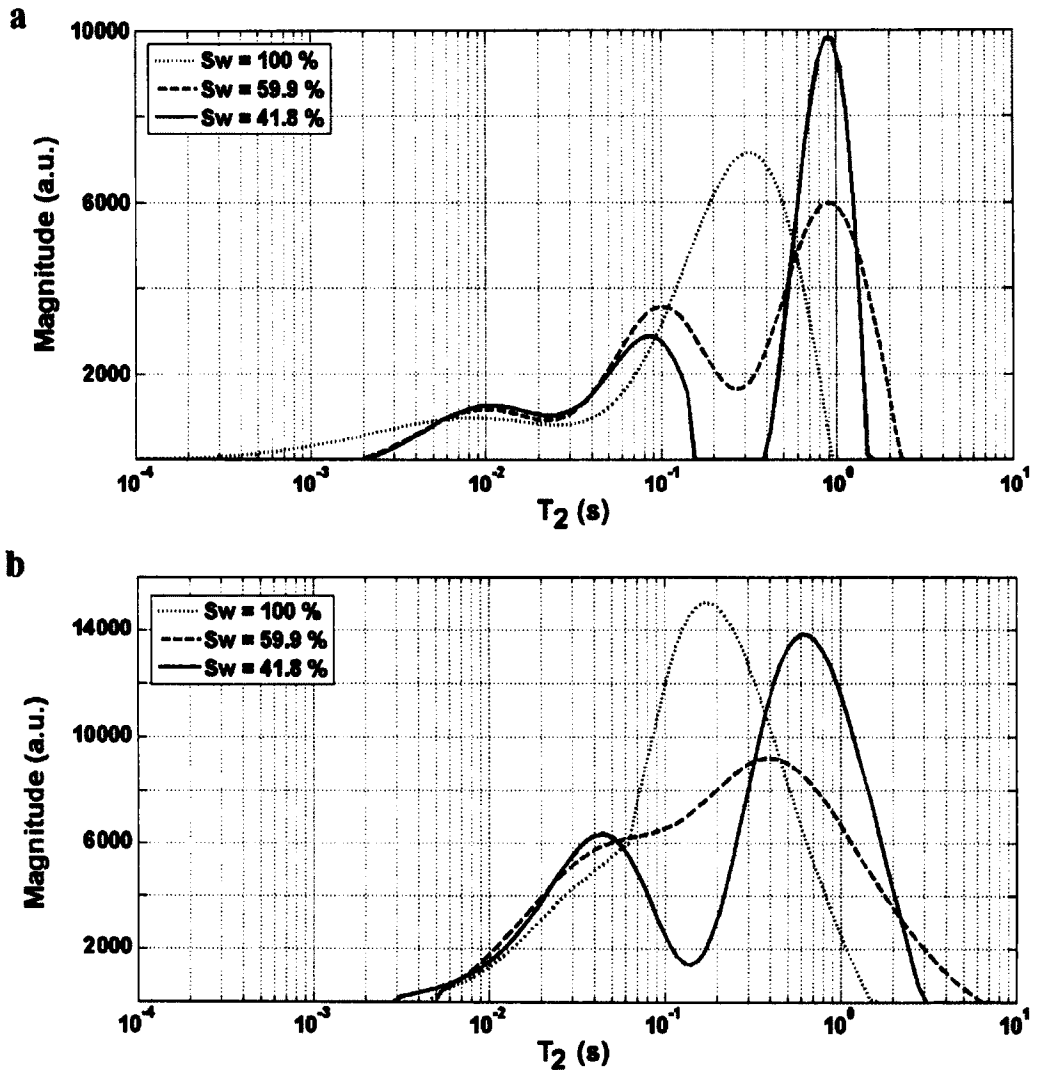

Figure 6.15. T_2 distributions for different water/oil ratios, observed in a 2 MHz homogenous field magnet (a) and employing the three-magnet array WA-1 (b). The dashed line represents the T_2 distribution for the first water/oil ratio (59.9% water and 40.1 % oil) and the solid line for the second ratio (41.8% water and 58.2 % oil). The dotted line shows the T_2 distribution for the full brine saturated sample.

The Berea sample under test is known to be water wet. The surface relaxivity of water in the pore space is higher and the T_2 distribution is shifted to the shorter T_2s than is the case for dodecane with a reduced surface relaxivity. With the continuous

flooding of dodecane, the movable water is displaced by dodecane phase, the saturation of dodecane increases, the right peak shifts to long T_2 component. The right most peak of the dashed curve corresponds to dodecane, the left most part of the distribution correspond to water that is difficult to displace. There is a slight overlap between the T_2 distribution of movable water and dodecane. From the solid curve, the dodecane phase and the water phase can be separated clearly by the T_2 distribution. The right peak of the T_2 curve corresponds to dodecane. The left peak corresponds to irreducible water. The volume of oil and water in the core plug can be estimated by the area under the curve in the T_2 distribution. The water saturation has been reduced from 100% to 59.9% and then to 41.8% by flooding. These are close to the values determined from the production data (57.7% and 38.6%). We do not achieve a reliable measure of irreducible water saturation, because the inlet pressure (15 psi) is not high enough to displace all the movable water.

This chapter has shown that the three-magnet array is a very simple and reliable tool for core plug analysis. We have shown that long core plugs of different diameters can be easily characterized employing this approach by simply changing the RF probe to be employed. The best RF probe for this approach is a simple solenoid which is easy to design and build. This type of probe is a much better approach than the surface coil in order to explore deeper layers inside the sample. In addition to the higher sensitivity, the more homogeneous B_1 permits a better excitation of the measurement spot which increases the level of the signal during

reception. The core plug, even when fully brine saturated, did not affect the Q of the probe during the experiment.

It has been shown that, even though the three-magnet array with an extended constant gradient reduces the size of the measurement spot and therefore reduces the SNR, it is a reasonable option for exploring very deep layers inside the core plug.

This experiment has also shown that the three-magnet array is a reliable approach to observe the T_2 distribution in rock core plug analysis. The T_2 distribution is a basic measurement that can be employed to obtain additional information from the core plug such as total porosity, pore-size distribution, permeability, bound-fluid porosity and free-fluid porosity [6, 7].

References

[1] J. A. Jackson, L.J. Burnett, J. F. Harmon, Remote (inside-out) NMR. III. Detection of nuclear magnetic resonance in a remotely produced region of homogeneous magnetic, J. Magn. Reson. 41, 411–421, 1980.

[2] C. G. Masi, M. N. Miller, NMR system for well logging. U.S. Patent 4717876, Jan. 1988.

[3] R. L. Kleinberg, A. Sezginer, D. D. Griffin, M. Fukuhara, Novel NMR apparatus for investigating an external sample, J. Magn. Reson. 97, 466–485, 1992.

[4] R. L. Kleinberg, NMR measurement of petrophysical properties, Conc. Magn. Reson, Vol. 13(6), 404–406, 2001.

[5] G. R. Coates, L. Xiao, M. G. Prammer, NMR logging principles and applications, Halliburton Energy Services Publication,1999.

[6] R. Freedman, Advances in NMR logging, J. Petrol. Tech. Jan, 60-66, 2006

[7] C. Straley, D. Rossini, H. Vinegar, P. Tutunjian, C. Morriss, Core Analysis by Low Field NMR, The Log Analyst, 38 (2), March – April, 1997.

[8] P. M. Singer, G. Leu, E. J. Fordham, P. N. Sen, Low magnetic fields for flow propagators in permeable rocks, J. Magn. Reson. 183, 167–177, 2006.

[9] S. Anferova, V. Anferov, J. Arnold, E. Talnishnikh, M.A. Voda, K. Kupferschläger, P. Blümler, C. Clauser, B. Blümich, Improved Halbach Sensor for NMR Scanning of Drill Cores, Magn. Reson. Imag. 25, 474-480, 2007.

[10] K. Halbach, Design of permanent multipole magnets with oriented rare earth cobalt material. Nucl Instrum Methods, 169, 1– 10, 1980.

Chapter 7

Application of selective pulses in UMR employing the three-magnet array

In commercial MRI the combination of RF pulses of narrow bandwidth applied in the presence of magnetic field gradients permits observation of the NMR signal from a small portion of the sample. In this way, different parts of the sample can be studied without interfering signal from adjacent regions. This technique, known as selective excitation, is common practice in MRI, but it is not common in UMR.

In UMR, unlike MRI, the magnetic field gradients will be permanent rather than switched. The magnetic field gradient will also tend to vary with position in UMR given the nature of the inhomogeneous fields employed.

For a variety of reasons, including observation of the NMR signal from a restricted portion of the sample, and attempting to remove short T_2^* effects due to inhomogeneous static fields, selective excitation has great merit in UMR.

Selective excitation has been minimally explored in UMR. Only one reference has been found in the literature [1]. The main reason is probably related to the fact that the sensitive spot is naturally small and a selective excitation will reduce still further the available signal compromising SNR. In this chapter we undertake an initial survey of the merits of employing shaped RF pulses for selective excitation in UMR.

Todica et al. [1] employed selective excitation with a DANTE sequence in order to reduce the power requirements in a portable UMR system. This technique employs a series of RF pulses which, in combination with magnetic field gradients, allow excitation of very narrow slices inside the sample. Marble et al. [2] combined the constant gradient produced by a unilateral magnet with the excitation produced by sinc shaped pulses in order to obtain better excitation profiles.

Perlo et al. introduced a different idea in order to produce selective excitation. In this case, the magnet design combines a strong magnetic field gradient of 20 T/m, perpendicular to the surface of the magnet, with excellent lateral homogeneity in a parallel plane. This combination allows selection in frequency and space even when non selective pulses are employed.

In this chapter we employ a three-magnet array UMR magnet design fabricated to produce a homogeneous spot [3]. The magnetic field at the centre of the spot was 1068 G. A solenoid was employed as the RF probe in order to provide a homogeneous B_1 for the measurements.

Our initial motivations in this study are (i) to reduce the bandwidth of the NMR signal to obtain FID signals, which are otherwise difficult or impossible in UMR because of the short T_2^* associated with an inhomogeneous static B_0 field. (ii) In addition reducing the ΔB_0 of the excited signal should result in a more ideal response of the spins system to CPMG measurement yielding a T_{2eff} measurement which is closer to the true T_2 behavior.

7.1 Frequency selection in UMR

Frequency selection of the detected NMR signal can be readily achieved by narrowing the low-pass filter width or employing selective excitation. In UMR, given the naturally inhomogeneous B_0 fields, the short lifetime of FID signals and rapid echo attenuation because of diffusion, it is best to evaluate the advantages and disadvantages of both approaches.

Reducing the low-pass filter width to modify the detected UMR signal is a very simple approach but it has the drawback of increasing the dead time of the receiver (see Eqs. 3.4 and 3.5). While not extensively discussed in earlier chapters, controlling and modifying the bandwidth of the detected UMR signal by altering the low pass filter is a strategy we commonly employ.

It is not however possible to narrow the filter sufficiently to isolate a sufficiently narrow range of frequencies to permit observation of an FID in UMR. For spin-echo measurements, the longer dead time associated with narrow bandwidth

filters implies longer echo times and additional T_2 and diffusion attenuation of the observed signal.

Frequency selection can be achieved by selective excitation. It can be implemented by reducing the bandwidth of the RF pulse, in order to excite only the desired band of frequency, or by suppressing the net magnetization in regions adjacent to it. The first approach usually results in long RF pulses and therefore, loss of signal because of relaxation during the excitation. With the second approach, selection by suppression, only the desired bandwidth remains in the *z* direction after exciting the adjacent bands employing selective pulses. In this way, very short 90° pulses can be employed for rotating the sample magnetization toward the transverse plane. Figure 7.1 illustrates both approaches to selective excitation.

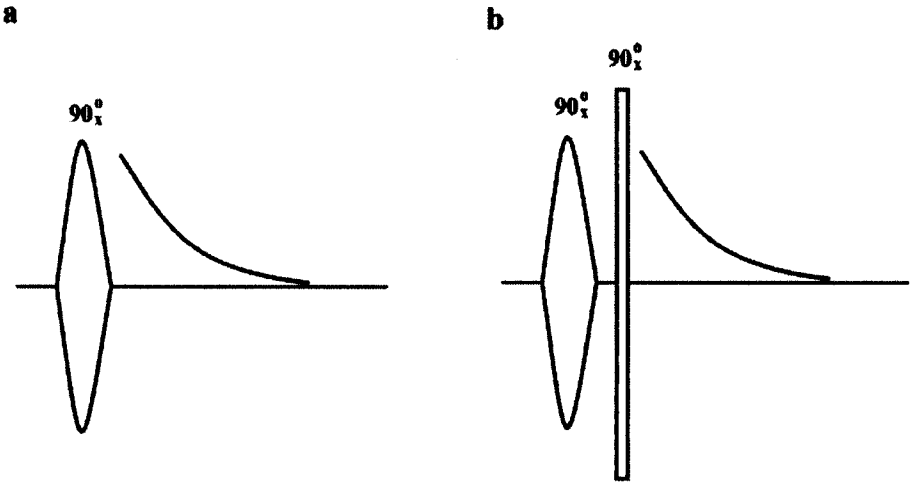

Figure 7.1. RF pulses for selective excitation, a) selective excitation by selection and b) suppression.

From the previous analysis, selective excitation by suppression has been chosen for our measurements. The suppression pulses were designed employing the Shinnar-Le Roux (SLR) algorithm [4, 5].

7.2 Shinnar Le Roux algorithm

The design of RF pulses for NMR is a non-linear problem because of the non-linearity of the Bloch equation. For small tip angles a Fourier transform analysis produces good results. For a 90° pulse, better results can be obtained by applying optimization methods and for larger angles, like 180°, optimization methods are indispensable [4].

The Shinnar-Le Roux algorithm [4,5] is based on a discrete approximation to the spin domain version of the Bloch equation [4]. The design of the RF pulse is based on the well known Parks-McClellan algorithm [6] for digital filter design. The resulting digital filter, designed according to the desired excitation bandwidth, is then mapped back into an RF pulse employing the Shinnar-Le Roux inverse transformation. The pulse generated by the algorithm; once applied to the sample, because of the non-linearity of the Bloch equations, will produce an excitation profile according to the desired pulse specifications.

By choosing the characteristics of the digital filter, different RF pulses can be obtained. Linear phase pulses, as required for the 90° and 180° pulses in spin-echo sequences, can be produced in this manner. Similarly, minimum and maximum phase

pulses, useful where the phase is not relevant such as in saturation pulses, can also be generated. Minimum and maximum phase pulses produce better suppression profiles than those with linear phase.

7.3 Designing the RF pulse

In order to design the selective RF pulse the MATLAB function MATPULSE [7] was employed. As illustrated in Fig. 7.2 different parameters may be set in order to obtain the desired pulse. For suppression pulses the band to be selected is determined by the separation between the two frequency bands to be excited. The parameters in Fig. 7.2 correspond to the actual pulse employed for the measurements.

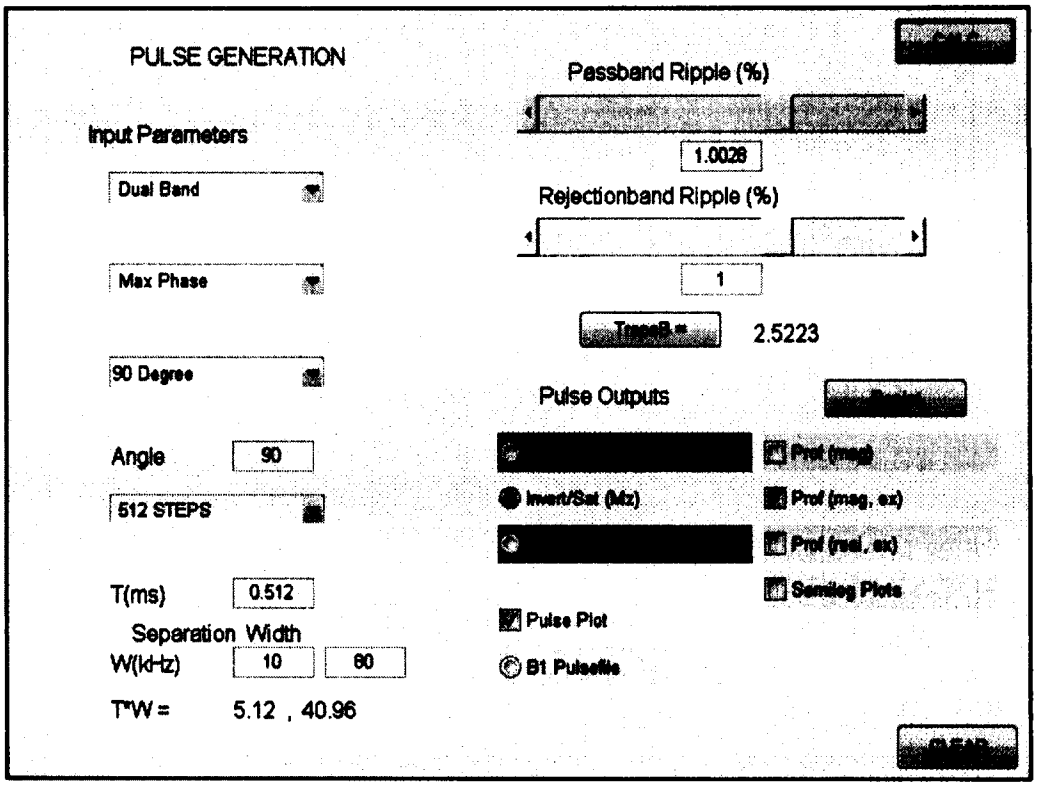

Figure 7.2. Dialog box of the MATPULSE function. All parameters for the RF pulse can be set in order to obtain a desired profile.

Figure 7.3a shows the excitation profile and the Fourier transform of the pulse generated employing MATPULSE. The differences between the two spectra are the result of the non-linearity of the Bloch equations. It should also be taken into account that the actual pulse applied to the sample is affected by the behavior of the transmission system. Different methods can be applied in order to evaluate and compensate for these distortions. For our experiments, a simple evaluation of different consoles, employing the spectrum in Fig. 7.3b, was undertaken in order to choose the most appropriate hardware system for the measurements.

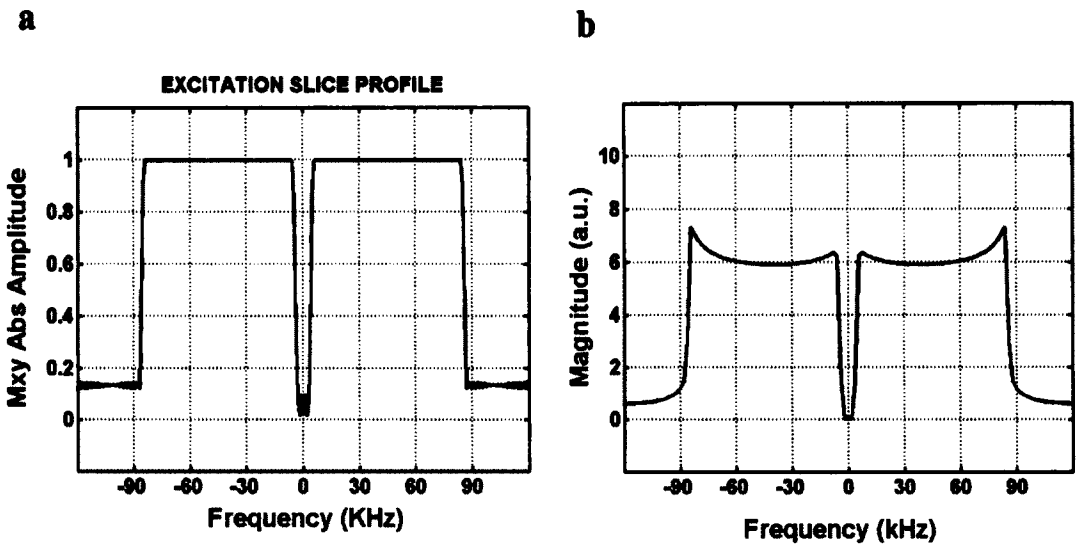

Figure 7.3. a) Excitation profile generated employing MATPULSE and b) Fourier transform of the generated pulse. The RF pulse, whose Fourier transform produces the spectrum in b), should produce the excitation profile in a).

The amplitude variation with time during the selective pulse is critical, therefore the linearity of the transmission system is critical to success. Non-linearities can introduce amplitude distortion and therefore alterations to the final excitation profile. A simple comparison of the RF pulse spectrum at different points of the transmission chain (see Fig. 7.4) was carried out on three different consoles in the UNB MRI laboratory. A Bruker Minispec console, an Oxford Instrument DRX console and a Tecmag Redstone console were compared for the measurement. The DRX and Redstone consoles employed a TOMCO Technologies power amplifier.

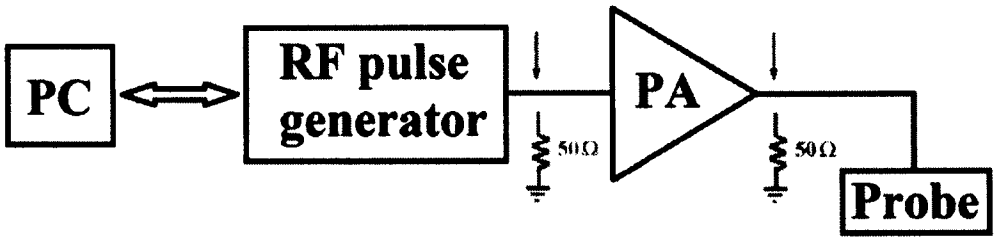

Figure 7.4. Measurement points in the transmission system. For each measurement the output of the stage was disconnected and replaced by a 50 Ω load.

Figure 7.5 shows the spectrum at the output of the power amplifier for the Minispec system (Fig. 7.5a) and the Redstone console combined with the TOMCO power amplifier (Fig. 7.5b).

a

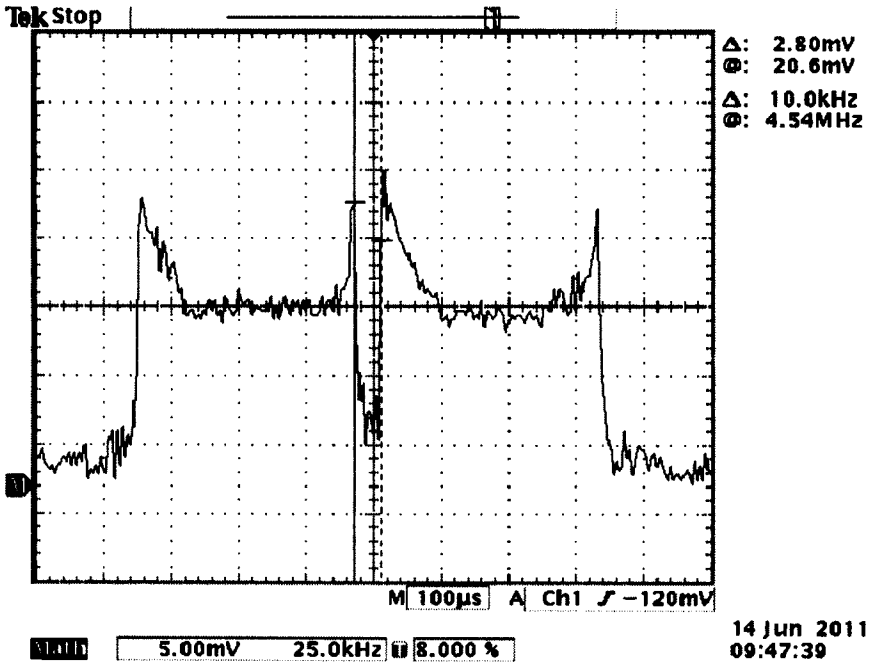

b

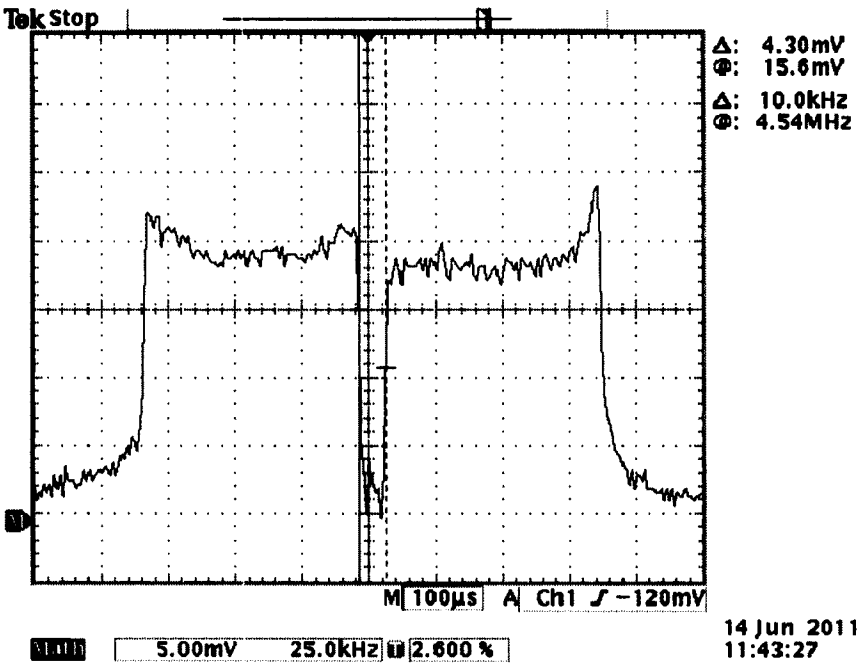

Figure 7.5. Spectrum of the chosen suppression pulse measured at the output of the power amplifier in two different NMR instruments. By comparison with the spectrum of the pulse at the input, the system with the output in b) was chosen for the measurements.

By comparison with the ideal output (see Fig. 7.3b) the combination of a Redstone console and a TOMCO power amplifier was chosen for the measurement. The distortions in the Minispec console could be related to the fact that it was designed to work at 10 MHz instead of 4.45 MHz which is the frequency at the centre of the sensitive spot in the three-magnet array, and hence the frequency of our trial pulse.

7.4 Spin echo experiment with selective preparation

In order to set the correct power for the selective pulse, the excitation profile produced by a spin echo sequence preceded by a suppression pulse was employed (see Fig. 7.6). The time τ_1, measured from the centre of the pulse was maintained at 360 μs for all measurements. The suppression pulse moves the longitudinal magnetization in the undesired regions of the spectrum to the transverse plane, leaving only the bandwidth of interest along the z axis, with this condition the spin echo sequence is performed as explained in section 2.1.4.1.

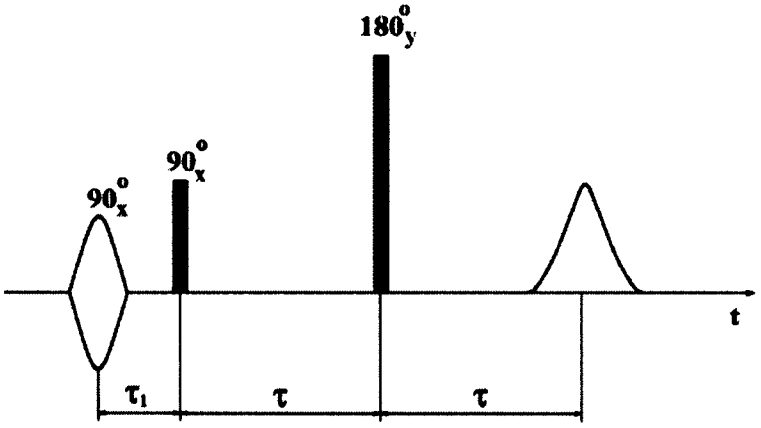

Figure 7.6. Spin echo sequence combined with a 90° suppression pulse

It should be noted that, after applying the 90° hard pulse, one half of the magnetization, moved onto the transverse plane by the selective pulse, remains in the transverse plane producing an echo at time $2\tau_1$ which is then refocused by the 180° pulse. The combination of the 180° pulse and the selective pulse produces an

additional echo at time $2\tau + \tau_1$. These echoes can be removed by choosing the appropriate phase cycling [8]. Table 7.1 shows the phase cycling scheme for the suppression pulse (SP), the 90° (HP1) and 180° (HP2) non selective pulses and the acquisition (Acq.).

Table 7.1. Phase cycling for spin echo with selective preparation

	1	2	3	4	5	6	7	8
SP	0	0	180	180	270	270	90	90
HP2	0	0	180	180	90	90	270	270
HP1	90	270	90	270	0	180	0	180
Acq.	0	0	180	180	90	90	270	270

For these measurements a solenoid was employed as the RF probe. To adjust the RF power, a homogeneous sample of cod liver oil was employed. This sample produces a good NMR signal, is less sensitive to diffusion attenuation, and has a shorter T_1 than water, which allows speeding up the measurements. The optimum suppression pulse power value was assumed to be the one that generates a profile close to the design parameters. Figure 7.7 shows the profile for three values of RF attenuation (Att) and the classic spin echo experiment with no selective pulse, which is employed as a reference. The best power value was found for a power attenuation of 4.5 dB of the selective pulse.

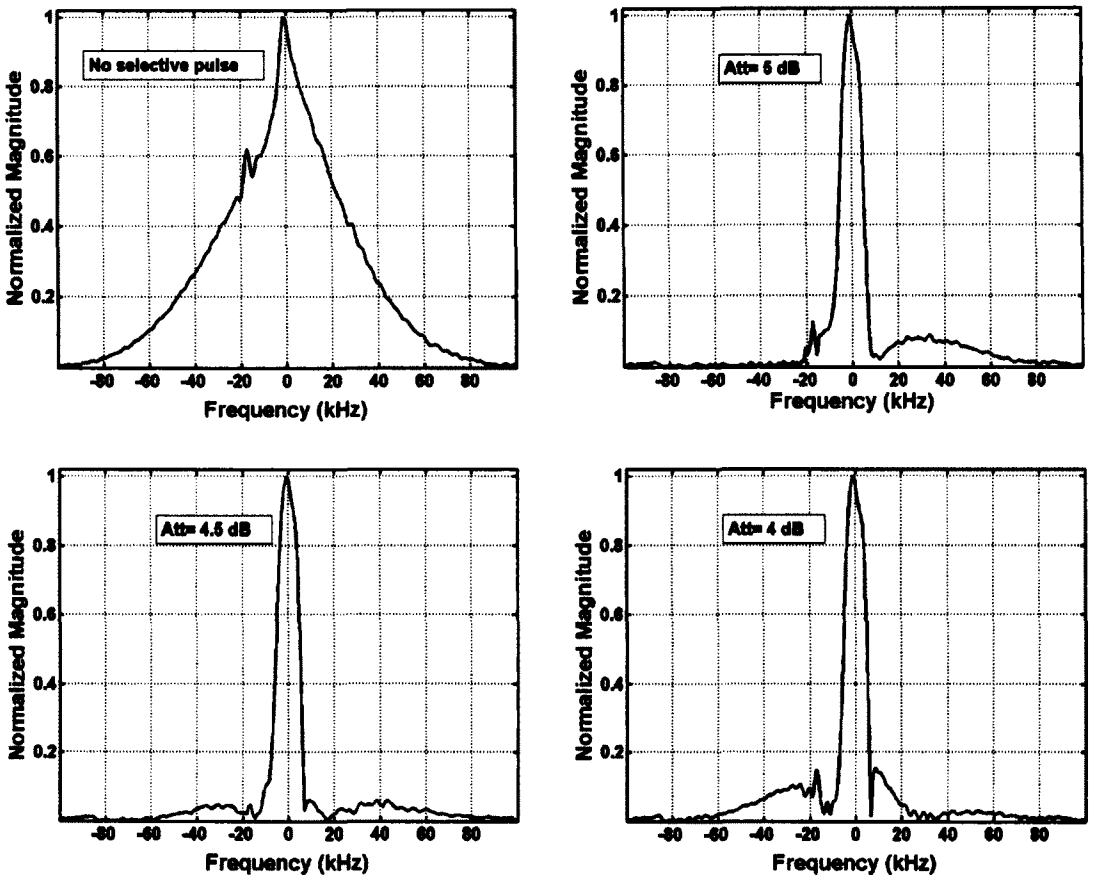

Figure 7.7. Profiles obtained for different values of RF power of the suppression pulse in a spin echo sequence with selective preparation.

As Fig. 7.7 shows there is good selection of the band of interest, although it was impossible to obtain a flat profile outside this band. Different factors can contribute to this problem. The electronics of the transmission system, even when selected to reduce this effect, can introduce distortions to the suppression pulse. The Q of the probe introduces another factor in the spectrum of the excitation pulse, which affects the excitation profile. In addition, imperfections of the 90° or 180° non-

selective pulses, which are hard to avoid in UMR, can also produce undesirable effects. The small peak around -20 kHz present in all the spectra is an artefact produced by an external interference.

7.5 FID signal employing selective preparation.

Because of the inhomogeneous magnetic field, the lifetime of the FID signal in UMR is usually shorter than the receiver dead time. Increasing the observable signal lifetime can be achieved by applying a suppression 90° pulse preceding the non-selective 90° pulse as outlined in Fig. 7.1b. Figure 7.8 shows the result of the measurement employing a sample of cod liver oil. The amplitude of the selective pulse was set according to the results of Section 7.3 for the spin echo experiment. Figure 7.8a shows the result of an acquisition applying a non-selective 90° pulse. No FID is observable. Figure 7.8b presents the result when the 90° pulse is preceded by a 90° suppression pulse. In this case the FID signal is clearly observed.

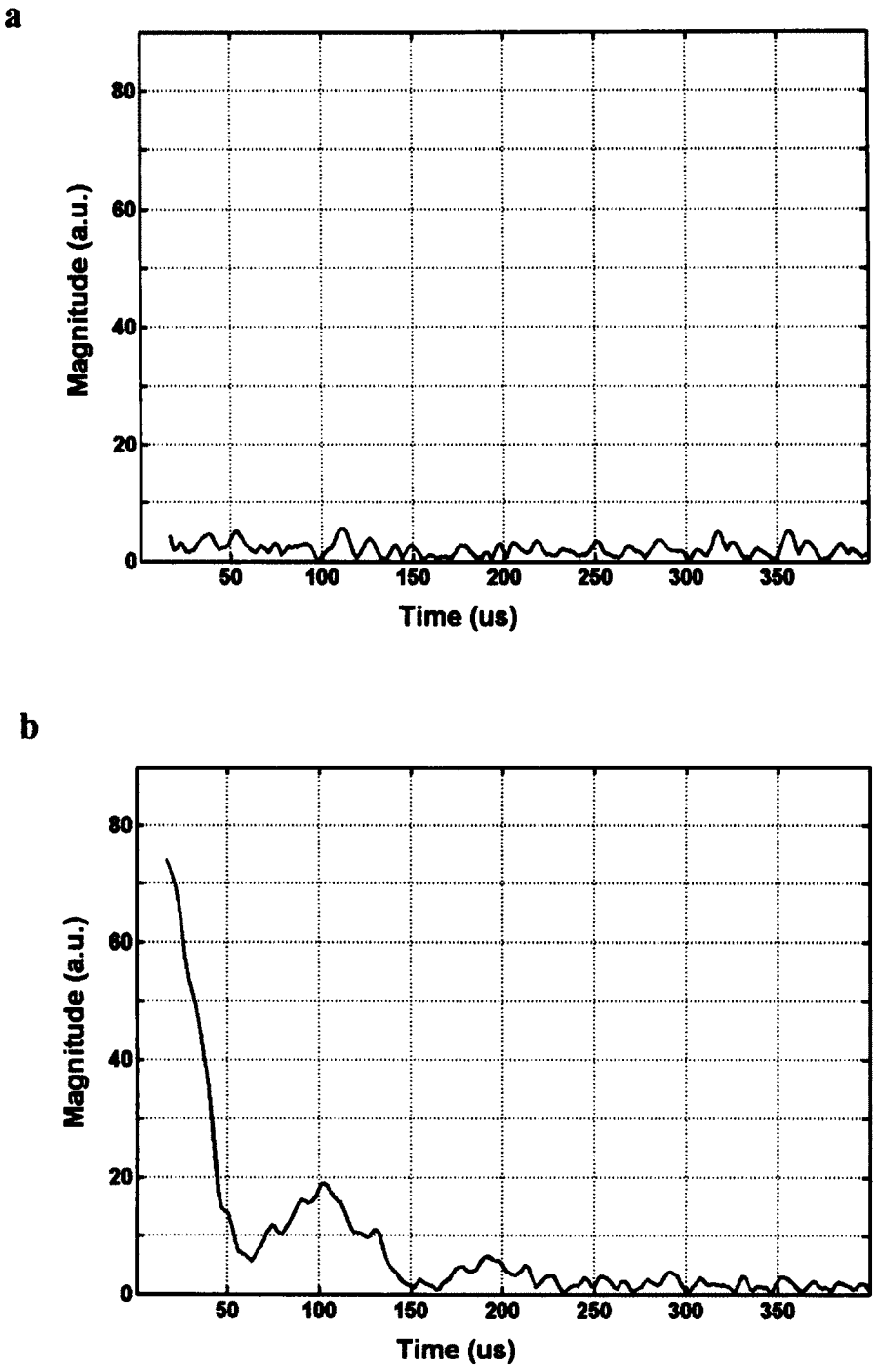

Figure 7.8. Signal after a 90° pulse. No FID is obtained when a non-selective pulse is applied (a). When the suppression pulse is applied in combination with the non-selective pulse the FID is clearly observed.

Despite the fact the FID signal is clearly observed with the selective preparation, it is dominated by the magnetic field inhomogeneities (see Eq. 2.11) in the selected region, making it almost impossible to differentiate samples with different natural lifetimes T_2. Figure 7.9 shows the normalized FID for three different samples with different T_2 values. Distilled water (solid line) with T_2= 2.5 s, cod liver oil (dashed line) with T_2= 175 ms and doped water (dotted line) with T_2 = 14 ms were employed for the comparison. The time of measurement was 85 min for water, 9 min for cod liver oil and 1 min for doped water. The number of scans was 512 for all the measurements. As can be observed the signal decay is the same for the three samples. This result was expected taking into account the natural linewidth for the three samples and the excitation bandwidth. The Sinc like shape of the observed FID (Fig. 7.9) is a result of the roughly boxcar shape of the unsuppressed signal (Fig. 7.7) which is observed following selective suppression.

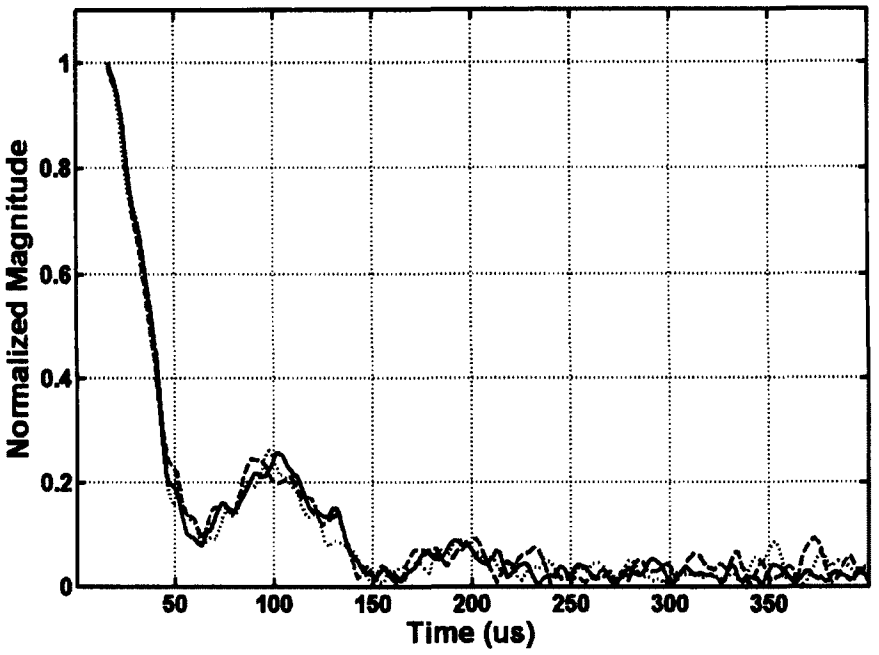

Figure 7.9. FID signals for three samples with different T_2 values. Distilled water (solid), cod liver oil (dashed) and doped water (dot) were employed.

Better differentiation could be achieved for samples with very short T_2 where the natural linewidth is broader than the 10 kHz of the selected band of frequency. Nevertheless, in this case the SNR of the measurement could be another issue for a realistic measurement.

7.6 CPMG measurement with selective preparation.

The CPMG sequence can also be combined with suppression pulses in order to obtain more localized T_2 measurements. Reducing the excitation bandwidth should yield T_{2eff} decay closer to the actual sample T_2 because of less contribution from regions of the space with stronger gradients and more ideal rotation of sample

magnetization by the pulse train. Figure 7.10 shows the CPMG sequence preceded by a 90° suppression pulse.

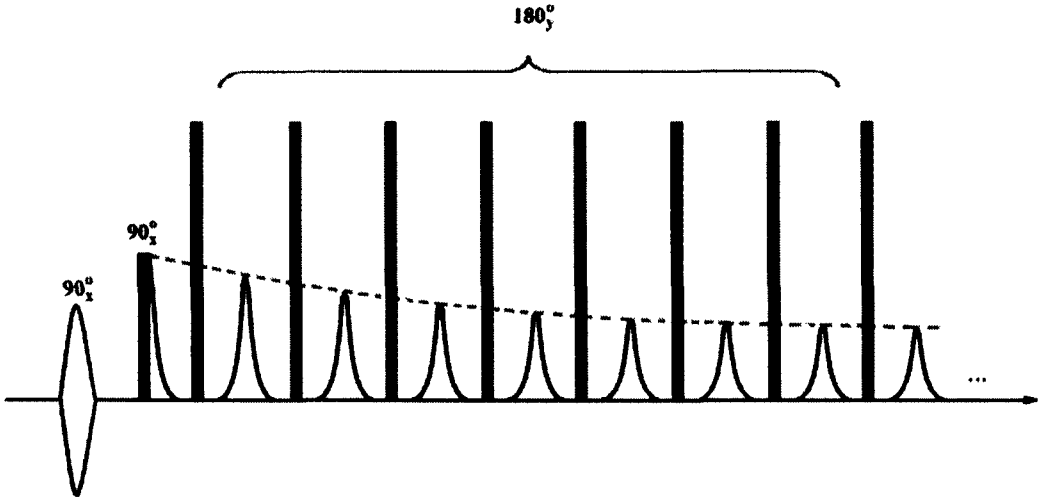

Figure 7.10. CPMG sequence with a suppression pulse preparation.

For the first measurement a homogeneous sample of distilled water was employed. The power of the suppression pulse was set to the optimum value obtained for the selective spin echo sequence. An additional measurement without selective excitation was undertaken for comparison. The time of measurement for the selective excitation was 3h for 1024 scans and 1h and 30 min for 512 scans with non selective excitation. Figure 7.11 shows the results for both measurements. The measured T_{2eff} decay is 265 ms for the selective excitation with CPMG and 169 ms for simple CPMG. The oscillation of the first echoes is approximately the same in both cases.

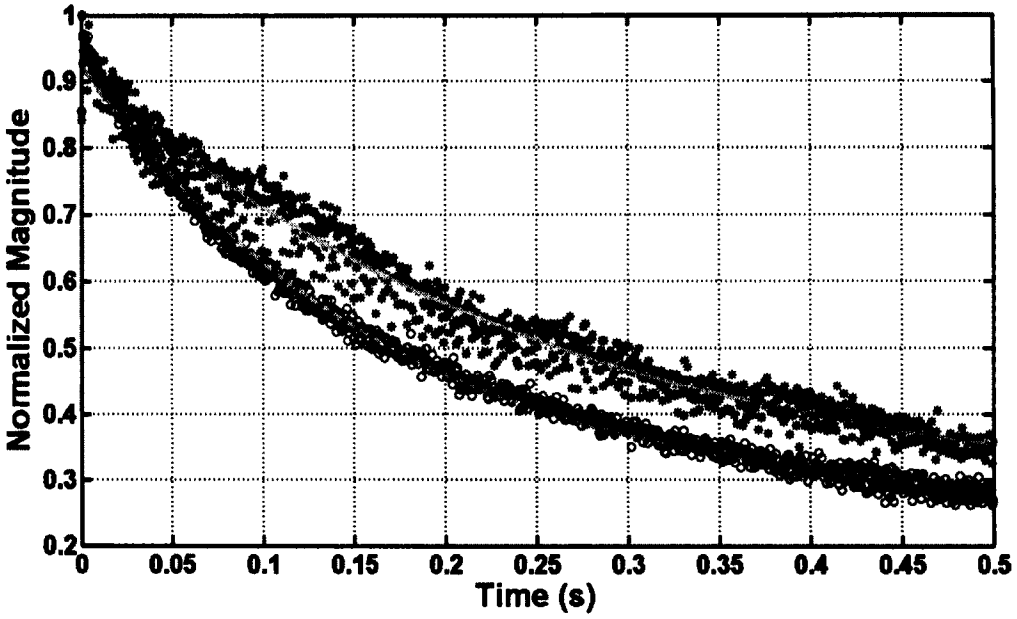

Figure 7.11. CPMG decays for a sample of water without selective preparation (o) and employing selective excitation (*).

As expected, the T_{2eff} for the selective measurement is longer than for the classical CPMG but it is still very different from the true T_2 of the sample measured at 10 MHz in a homogeneous field magnet, 1.6 s. In this case, both diffusion and T_1 are influencing this result therefore it is convenient to separate both effects in order to evaluate their influence. There is also a decrease in SNR because of the reduction in size of the sensitive spot.

A second experiment was undertaken employing a solid sample in order to reduce the effect of diffusion, and to separate the effect of the T_1 contribution (see Eq. 2.23). An elastomeric sample (T_1 = 20 ms) of polyvinyl chloride, 3 cm in length,

2.2 cm width was employed for this measurement. The T_2 value of this sample, measured at 10 MHz in a homogeneous field, was 2.2 ms. As in previous experiments, measurements with and without selective excitation were undertaken for purposes of comparison. Figure 7.12 shows the result of these measurements.

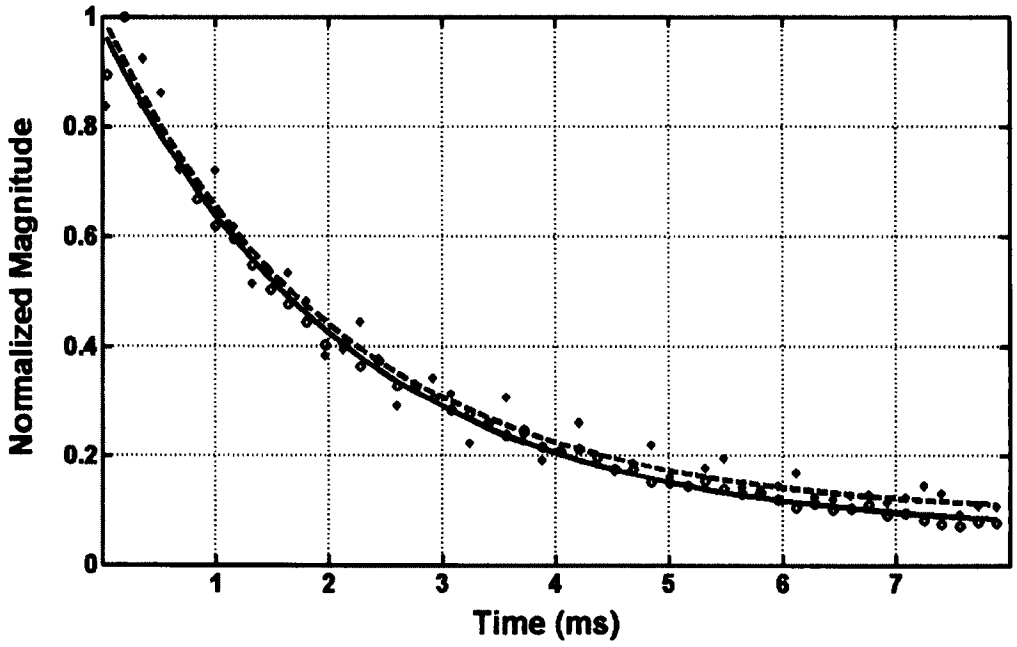

Figure 7.12. CPMG decays of an elastomeric sample employing selective excitation (diamonds) and without selective pulses (open circles).

The T_{2eff} measured for the selective excitation CPMG experiment was 2.1 ms and 2.2 ms for CPMG without selective preparation. Both results are quite similar to the homogeneous field measurement. This result shows that the influence of T_1 is practically insignificant even without selective pulses.

The previous results show the strong influence of diffusion on the measurement, even when selective pulses are employed. By reducing the frequency range of the excitation, the sensitive spot is reduced in size. This reduction will have a stronger effect in regions where the magnetic field gradients are very strong. Nevertheless, those regions will still contribute to the signal reducing its lifetime. How significant is the influence of these regions can be explored by running a CPMG measurement without selective preparation with a very small sample of cod liver oil placed at the centre of the spot. Figure 7.13 shows the result of this measurement. The sample was cylindrical with a 5 mm diameter and 1 cm length. For this measurement the longitudinal axis of the sample was oriented along the x axis of the magnet.

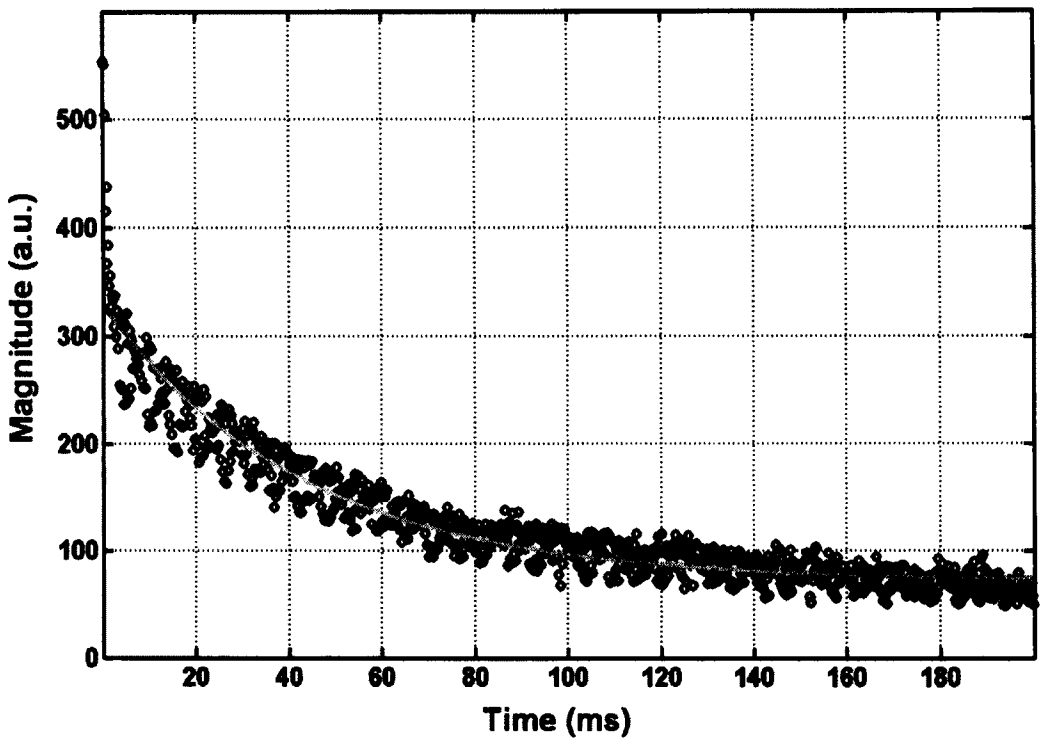

Figure 7.13. T_2 decay of a small size sample of cod liver oil. The number of scans for this measurement is 8 times greater than employed for selective excitation.

The measured T_{2eff} was 43 ms, which is shorter than the T_2 in homogeneous field (T_2 = 175 ms). This result shows that even inside a reduced size spot the gradients are strong enough to produce appreciable attenuation by diffusion. The SNR for this measurement was lower than for the selective suppression experiment even when the sample covered a wider frequency bandwidth (20 kHz vs. 10 kHz in selective excitation). This reduction means that for selective excitation other regions over the magnet are also contributing to the signal.

These results can be explained by examination of the magnetic field distribution over the magnet. Figure 7.14 shows the distribution of the magnetic field at the centre of the spot along the *z* direction.

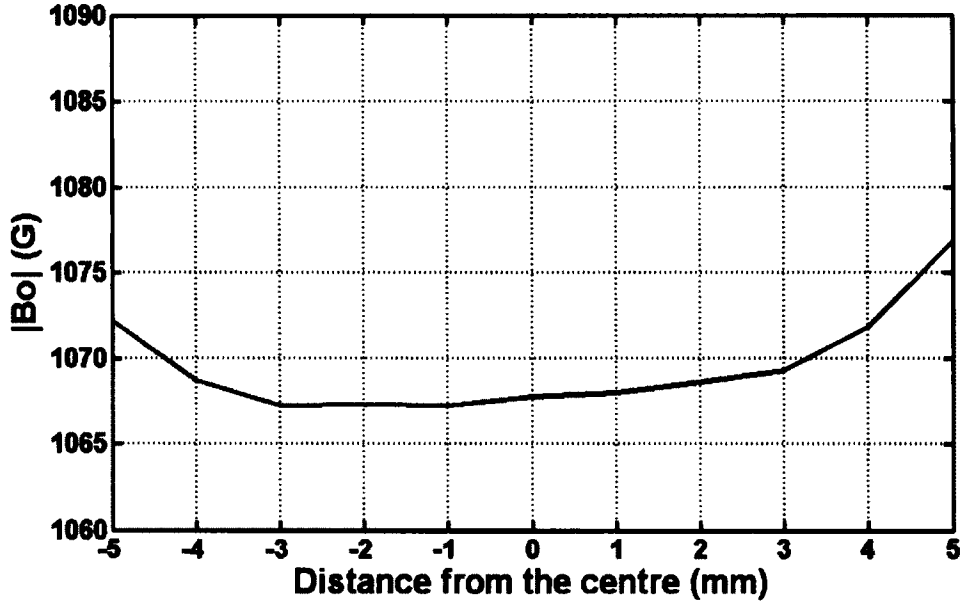

Figure 7.14. Magnetic field distribution along the z axis in the region around the centre of the sensitive spot. This gradient is produced by small differences between the external blocks.

As can be observed there is a magnetic field gradient of 4 G/cm in a region of 5 mm around the centre, and even higher further away. This gradient is a result of small differences between the field strength of the external blocks. Reducing the bandwidth of the excitation pulse reduces the size of the spot, but not the gradient.

From these results it can be inferred that selective excitation it is not very helpful in obtaining better quality T_2 measurements employing the three-magnet array. Any solution for this problem should be focused on discrimination in diffusion more than

in position, which means measurements more gradient selective than frequency selective.

References

[1] M. Todica, R. Fechete, B. Blumich, Selective NMR excitation in strongly inhomogeneous magnetic fields, J. Magn. Reson. 164, 220–227, 2003.

[2] A. E. Marble, I. V. Mastikhin, B. G. Colpitts, B. J. Balcom, Analytical design techniques in Unilateral NMR, 5th Colloquium on mobile NMR, Perugia, Italy, 2005.

[3] A. E. Marble, I. V. Mastikhin, B. G. Colpitts, B. J. Balcom, A compact permanent magnet array with a remote homogeneous field. J. Magn. Reson. 186, 100–104, 2007.

[4] J. Pauly, P. Le Roux, D. Nishimura, A. Macovki, Parameter relations for the Shinnar-Le roux selective excitation pulse design algorithm, IEEE Trans. Med. Imaging, Vol. 10, No. 1, 53-65, 1991.

[5] G. B. Matson, An integrated program for amplitude-modulated RF pulse generation and re-mapping with shaped gradients, Mag. Reson. Imaging, Vol. No. 8, 1205-1225, 1994.

[6] A.V. Oppenheim, R.W. Schafer, Discrete-Time Signal Processing, Prentice Hall, New Jersey, 476-478, 1989.

[7] G. B. Matson, An integrated program for amplitude-modulated RF pulse generation and re-mapping with shaped gradients, Mag. Reson. Imaging, Vol. No. 8, 1205-1225, 1994.

[8] D. D. Traficante, Phase-Sensitive Detection. Part II: Quadrature Phase Detection, Concepts Magn. Reson., 2, 181-195, 1990.

Chapter 8

Contributions and Conclusions

8.1 Contributions

This thesis has presented solutions and new applications for three-magnet UMR magnet arrays. Parts of this work have been published as articles in refereed journals and conference proceedings.

We have provided a detailed description of the building process for the three-magnet array. Substantial improvements to the original design have been introduced in order to broaden the applications and possibilities of this approach. Technical details for choosing the parameters of the RF probe have been also analyzed. We have shown that it is possible to explore deep layers inside the sample employing the three-magnet array. These results are important for applications like rock core plug analysis.

A handheld three-magnet array has been introduced as well as the idea of employing a solenoid as the RF probe for core plug analysis. These contributions

were presented at the "10th International Conference on Magnetic Resonance Microscopy" in Montana, USA.

The employment of the three-magnet array for monitoring the cure process of an epoxy/polyamidoamine system, included as Chapter 4 in this thesis, has been published as an article in the journal NDT&E International. We have shown that it is possible to monitor the curing process by observing the decreasing of the amplitude and the T_{2eff} obtained from a CPMG echo train. This behavior also allowed very fast measurements employing a single scan CPMG acquisition.

We have proposed a new idea for generating extended constant gradients employing the three-magnet array. Extended constant gradients of more than 3 cm extent were obtained. Applications for measuring diffusion, rock core plug characterization and profiling were presented. These results, presented in Chapter 5, have been presented at the 10^{th} Conference on Magnetic Resonance in Porous Media in Leipzig, Germany, and published by the Journal of Magnetic Resonance as a scientific article.

We have modified the spacers of the three-magnet array to reduce the inhomogeneities produced, along the longitudinal axis of the array, by the finite length of the magnet blocks. The improvement on the magnetic field distribution employing split steel spacers has been shown with practical magnetic field measurements.

We have shown that the three-magnet array can be applied for measuring long core plugs of different diameters. This approach is simpler and cheaper than previous ideas and produces reliable results.

A new approach for low pass filtering during MRI experiments with pure phase encoding has been presented as an appendix of this thesis. We showed that it is possible to increase the SNR by around 20 % during the acquisition process by properly setting the bandwidth of the lowpass filter in accordance with the applied gradient strength.

8.2 Conclusions

This thesis has presented a group of solutions to broaden the range of applications of the three-magnet array. With this magnet design it is possible to generate sensitive spots 2.5 cm from the surface of the magnet. This idea will allow exploring deeper layers into the sample which is a requirement for core plug analysis.

It has been shown that a simple portable unilateral MR probe, such as the three-magnet array, can rapidly provide real-time information on the state of a curing thermosetting resin. A single measurement can be accomplished in a single scan in around 20 ms. This method could be applied for monitoring and quality control of composite parts.

It has been shown that it is possible to increase the NMR signal obtained with the three-magnet array by around 90 % by employing ferromagnetic spacers. This thesis has shown that it is possible to generate constant magnetic field gradients of more than 3 cm extent with the three-magnet array.

We have proven with practical measurements that the three-magnet array can be employed for core plug analysis. This approach combines a simple, robust and flexible magnet design with a simple RF probe. Core plugs of different diameters can be studied just by changing the diameter of the solenoid employed as the RF probe. This idea is simpler than previous approaches and also produces reliable results.

Selective excitation has also been tested with the three-magnet array. Even though it is possible to obtain FID signals and better T_2 decays, they are dominated by the effect of the magnetic field inhomogeneities inside the selected spot. In addition, the reduction of the sensitive spot leads to low SNR during the measurements.

8.3 Future directions

The three-magnet array design has been improved as a result of the work of this thesis, but it still has potential for substantial further improvement. The lateral homogeneity of the array could be improved along the transverse direction by exploiting the idea presented here for the longitudinal axis. In the transverse direction the two external blocks can be assumed as split parts of a single block. It should be

possible to find the optimum width of the ferromagnetic spacers in order to improve the homogeneity in this axis.

Generating constant gradients of lower intensities, without reducing the overall static field produced by the array, is a challenging problem. A solution for this will be beneficial for many applications.

The employment of MATLAB as a flexible tool for the design process should be extended to the employment of ferromagnetic spacers. This would make easier the design process and would be very helpful to extend the idea to the transverse axis. MATLAB can be also employed to simulate the behavior of the probes over the irregular and conductive surface of the three-magnet array.

An important future direction is the development of new applications for the three-magnet array. New applications in rock core plugs analysis should be developed. 2D measurements correlating T_2 and diffusion attenuation, T_1-T_2 and other new measurements can be implemented in order to extract more information from the rock core plugs.

Appendix

Variable Bandwidth Filtering for Magnetic Resonance Imaging with Pure Phase Encoding

This Appendix is largely based on the paper "Variable Bandwidth Filtering for Magnetic Resonance Imaging with Pure Phase Encoding" published in the Journal of Magnetic Resonance, 202, 2010, 234-238. It proposes a new way of filtering, employing variable bandwidth filters, for MRI experiments with pure phase encoding.

9.1 Introduction

Magnetic resonance with pure phase encoding has been employed for approximately twenty years in different applications, mainly related to the study of solid-like samples and porous media [1-7]. Because of the fixed encoding time t_p, the magnetization time evolution is not measured. Instead spatial information is encoded by changing the amplitude of the applied gradient and a different k-space point is sampled for each RF pulse. Single point methods are largely immune to artifacts

caused by magnetic field inhomogeneities, chemical shift, and dipolar and quadrupolar distortions [2].

Nevertheless, pure phase encode measurements are inherently less sensitive than frequency encoding due to the fact each excitation results in acquisition of only a single k-space point. Balcom *et al.* introduced the SPRITE measurement which demonstrated a dramatic reduction in the time of experiment [3]. However, SPRITE is still inefficient compared to frequency encoding and additional strategies to improve the inherent SNR are desirable. Eliminating or reducing the necessity of signal averaging is critical to speeding up the technique.

Romanenko et al. [4] has introduced a variable flip angle excitation scheme for increased sensitivity in SPRITE MRI with very good results. A second complementary approach is presented in this paper, focused on the filtering process in the SPRITE measurements.

Conventional filtering, employed in pure phase MRI experiments, is inefficient. The central k-space points, with narrow signal bandwidth, are filtered using a fixed low-pass filter set according to the bandwidth of peripheral k-space points. This study introduces a new way of filtering for pure phase encoding sequences using a Variable Bandwidth Filter (VBF). Practical measurements show a gain of 20% in SNR in comparison with conventional fixed low-pass filtering, which would translate into a 31% reduction in the duration of the experiment (if limited by SNR), without other effects on the original image.

9.2 Theory

9.2.1 Pure phase encoding experiment.

In pure phase encoding measurements, as in SPRITE (see Fig. 9.1), magnetization evolution for a fixed time with different gradient strengths is employed to acquire data points in k-space. The n^{th} sampled k-space point (commencing at the origin) is given by,

$$k_n = \frac{\gamma n \Delta G t_p}{2\pi}, \qquad (9.1)$$

where ΔG is the fixed gradient increment between RF pulses.

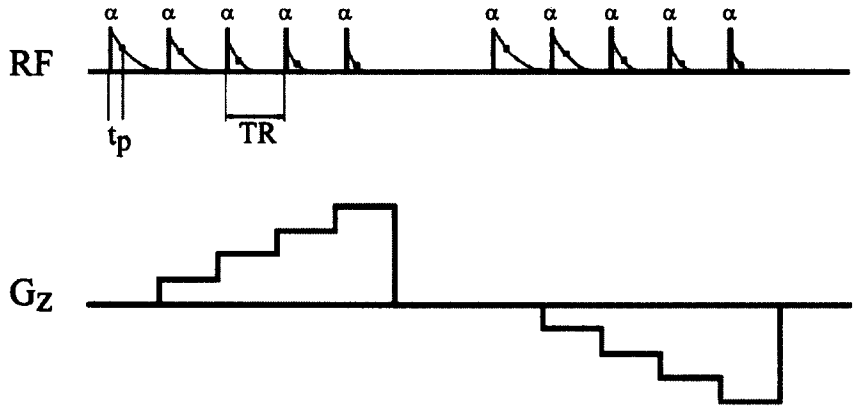

Figure 9.1. SPRITE pulse sequence. A one dimensional phase-encoding gradient (G_z) is employed to obtain a sample profile. A single FID point is sampled at a time tp after each RF pulse (α).

For each k-space point a new gradient value and RF excitation pulse is applied and, after a fixed encoding time t_p, a single data point is acquired. In the proposed scheme the signal bandwidth will increase proportional to k_n in progressing from the center to the extreme of k-space. The low-pass filter width FW should normally be set according to the maximum applied gradient amplitude,

$$FW \geq \frac{|G_{\max}|}{2t_p \Delta G}, \tag{9.2}$$

as given by Gravina and Cory [2]. The signal from the central points of k-space, which have narrow bandwidth BW given by,

$$BW = \frac{n}{2t_p}, \tag{9.3}$$

will incorporate noise and be filtered inefficiently. An optimal solution will involve the use of a filter with variable bandwidth linked to the k-space sample index. This means that for each gradient step a new filter width should be applied.

9.2.2 Variable Bandwidth Filter

The simplest way to examine the VBF is to consider noise in the signal as white noise (as is the case for thermal sources), with an ideal transfer function of the low-pass filter having $|H(f)|=1$ in the pass-band, $|H(f)|=0$ in the stop-band [8, 9]. In this case, because the noise power spectral density is constant over the whole

bandwidth, the reduction in noise power will be directly related to the selected bandwidth. Therefore, changing the filter width according to the signal bandwidth will result in a decrease in the noise power from the extremities of k-space, where the bandwidth is wide, to the centre where it is very narrow. This means that in the filtered k-space the ideal power spectral density function (Φ_n) will follow a linear variation, directly proportional to the k-space sample index (Fig. 9.2). Therefore, it should be possible to remove one half of the noise power in the k-space data, which means an increase of $\sqrt{2}$ in SNR of the profile.

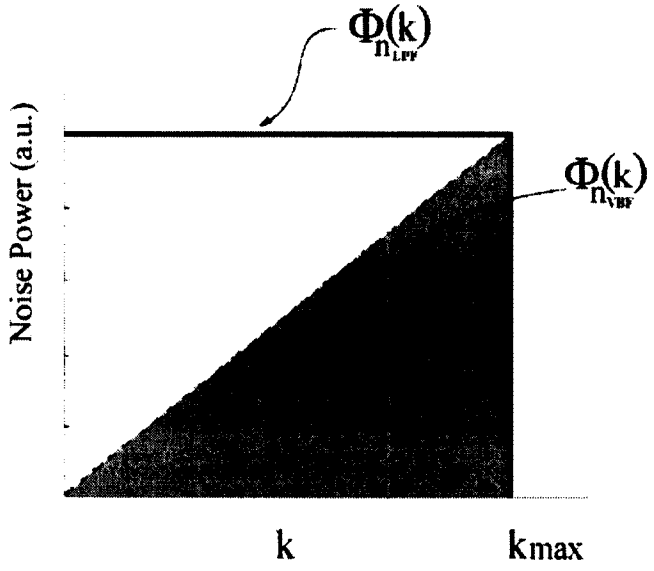

Figure 9.2. Power spectral density of ideal white noise $\Phi_n(k)$ resulting from the filtering process using an ideal low-pass filter. The shaded area represents the power spectral density when the VBF is applied. Ideally one half of the noise power from the k-space data should be removed, which means an increase of $\sqrt{2}$ in SNR for the profile.

In SPRITE the maximum encoding bandwidth increases with each added dimension because of the linear superposition of the gradients. For 2D the required filter width *FW* is,

$$FW = \frac{\gamma}{2}(FOV_x \mid G_{x\max} \mid + FOV_y \mid G_{y\max} \mid) \qquad (9.4)$$

The filter width for 2D is therefore twice that of 1D for a square FOV. Similar analysis can be undertaken for 3D with similar results. The conclusion is always the same, namely that the maximum overall increase in SNR available is $\sqrt{2}$.

One usually assumes that the SNR in an acquisition will be directly proportional to the square root of the number of averages [10]. Therefore, the gain in SNR using VBF is the same as two signal averages using classical low-pass filtering. In other words, VBF offers a potential reduction of 50% in time for a SPRITE experiment with fixed SNR.

In the practical implementation of VBF, a zero-phase filter (zero delay) [8, 9] is required in order to avoid problems with phase modulation of k-space. This type of (non-causal) filtering is physically unrealizable [8] and is only possible with offline processing [11]. Even when this phase modulation can be corrected, because the parameters of the VBF are known, this would introduce an additional and unnecessary complexity to the filtering algorithms. Therefore, for real time applications it is very important to maintain the same delay for all frequency

components. This means that all the filters must have the same order and the sampling frequency must be constant and independent of the bandwidth [8, 9]. Hence, even for VBF, the data must be acquired with a significantly higher bandwidth than would usually be the case.

We anticipate very efficient filtering at the k-space origin, which should improve SNR. In reality the filter cannot be set to zero and is subject to a minimum constraint dependent on t_p and system dead-time. In addition the VBF will be less efficient at the k-space periphery, which controls fine details in the image.

Ideal behavior is of course not always observed for real electronic systems [12]. Hence, it is not possible to evaluate the true VBF performance in advance. Therefore, this study presents the result of applying 28 VBF filter widths in a 64 point centre-out double half k-space acquisition. This result is compared with a classical fixed low-pass filtered image. Each filter width was applied in both half k-spaces, resulting in 56 VBF filtered k-space points during the whole acquisition process to obtain the filtered profile.

9.3 Results and Discussion

Figure 9.3 shows four filter widths of the VBF obtained with the parameters and proposed algorithm; the pass-band attenuation is 0 dB and, more than 60 dB in the stop-band. For the central k-space point, where no gradient is applied, a very narrow filter could be employed making very efficient the VBF in this area. The only

limitation for the filter width at this point is the signal linewidth which is inversely related to T_2^*. Therefore, the most efficient filter will depend on a sample parameter, making the filter setting sample specific which is not desirable. Instead, the minimum filter width was set according to the first non-zero gradient which is related to the image field of view and is therefore size specific. The VBF was not applied to the k-space extremity points where classical low-pass filtering was employed.

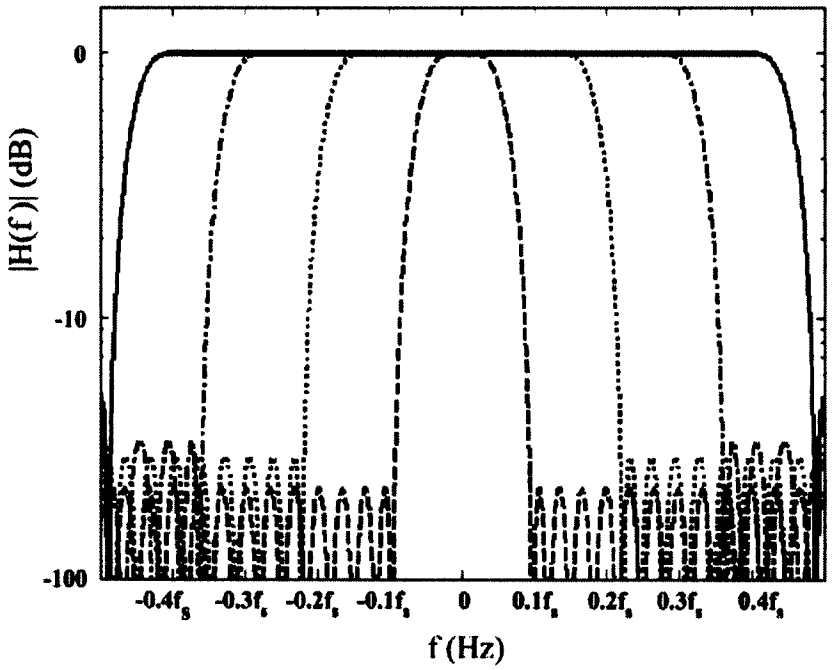

Figure 9.3. Transfer function *H(f)* of four VBF filter widths. The filter width is very narrow in the centre of the k-space (--) and wider in the extremity (-). The sampling frequency (f_s) is 1 MHz and the filter order has been fixed to 30.

In the first experiment, a noise only profile was acquired in the absence of sample. The noise voltage with and without VBF was calculated for forty profiles to measure the noise reduction in each of them. The mean value reduction in all these

measurements was 20% with a standard deviation of 8%. One of the noise profiles with and without VBF is illustrated in Fig. 9.4.

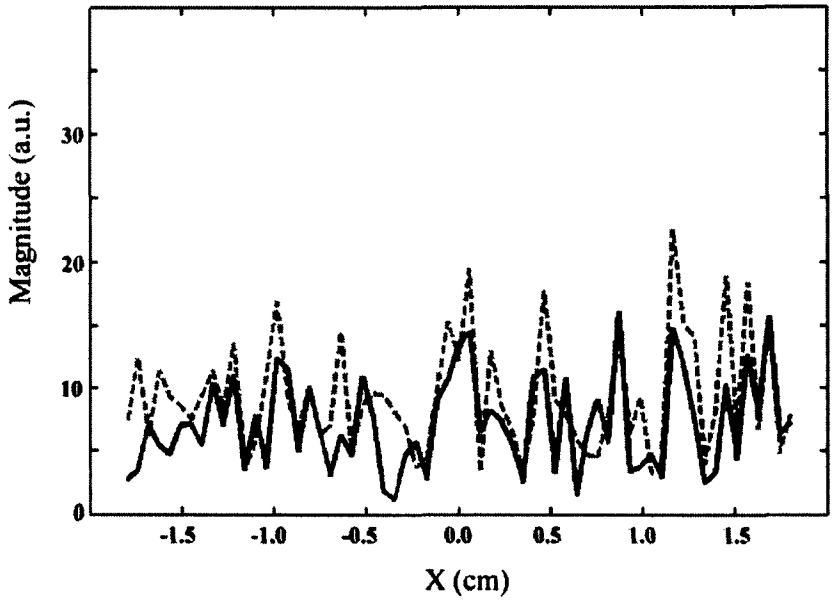

Figure 9.4. Image acquisition in the absence of sample using a classical low-pass filter (--) and VBF (-).

In a second step, the same measurement was carried out over a homogeneous region of one profile from the experimental sample, obtained with the same acquisition and processing parameters of our previous experiment. Figure 9.5 shows a comparison between the filtered profile using classical low-pass filtering and VBF. Because of the shape of our sample, the ideal profile should be a boxcar function and any uncertainty will be considered noise. In this case, the gain in SNR is 24% in the homogeneous region (top centre) of the profile, which agrees with the previous result and means a reduction of 35% in the time of experiment. As can be observed, the VBF has no deleterious effects on the profile shape.

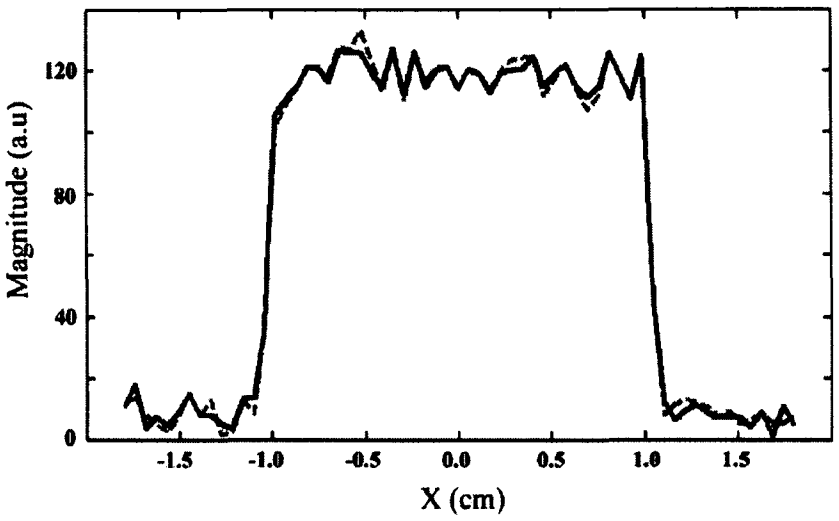

Figure 9.5. 1D image obtained with classical low-pass filter (--) and VBF (-). In this case, the gain in signal to noise was 24%, which means a reduction of 35% in the time of experiment. VBF does not affect the sharp edges in the profile.

The filter width of the classical low-pass filter was set for 500 kHz, which is wider than the optimal value (81.6 kHz), to be able to acquire 128 points for post processing. The filter widths of the VBF have been designed according to the bandwidth of the classical low-pass filter and the number of gradient steps. Wider low-pass filter will imply wider VBF filter widths. Therefore, the noise reduction, as a relative measurement, will be independent of the bandwidth.

The observed difference between the ideal SNR gain (40%) and the experimental realization (20%) can be explained from a critical analysis of the experiment assumptions.

In the ideal case, zero filter width in the k-space origin was assumed. Nevertheless, in practical implementations of VBF the minimum filter width was set according to the lowest gradient value different from zero, which is wider than the signal linewidth. This reduces the filtering effectiveness in the centre of the k-space, shifting up the ideal noise distribution (Fig. 9.6), but makes the VBF independent of the sample.

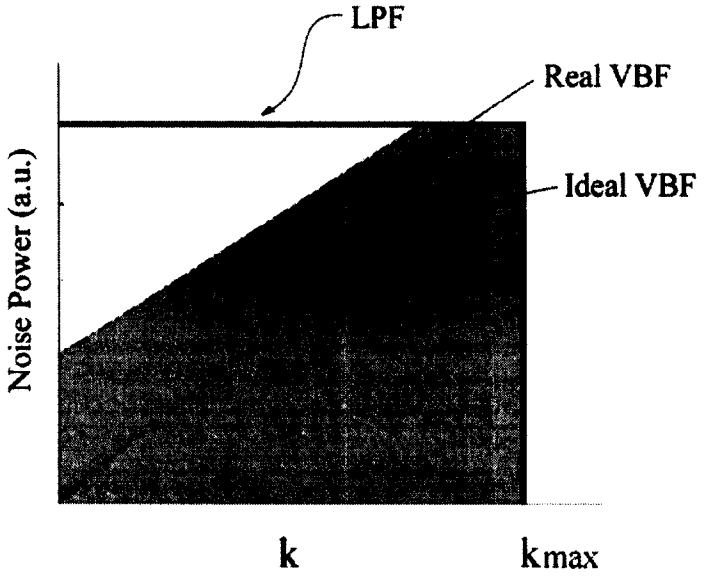

Figure 9.6. Descriptive representation of the influence of real factors on the ideal VBF performance of Fig. 2. Wider filter width in the centre of k-space and noise in electronic systems (non ideal) shift up the ideal line in the centre of k-space. Unfiltered k-space extremity points shift it left. The non ideal transition band of the VBF filter widths contribute to both effects.

In general, the white noise condition is not achieved because of the combination of different noise sources in electronic devices, most of them in the low frequency band [10, 12]. The combination of all these sources will increase the noise

energy in the low frequency band and therefore increase the noise in the centre of k-space (Fig. 9.6). The power spectral density of the noise in the receiver system (Fig. 9.7) obtained from forty noise acquisitions employing Welch averaging modified periodograms [8] shows this behavior.

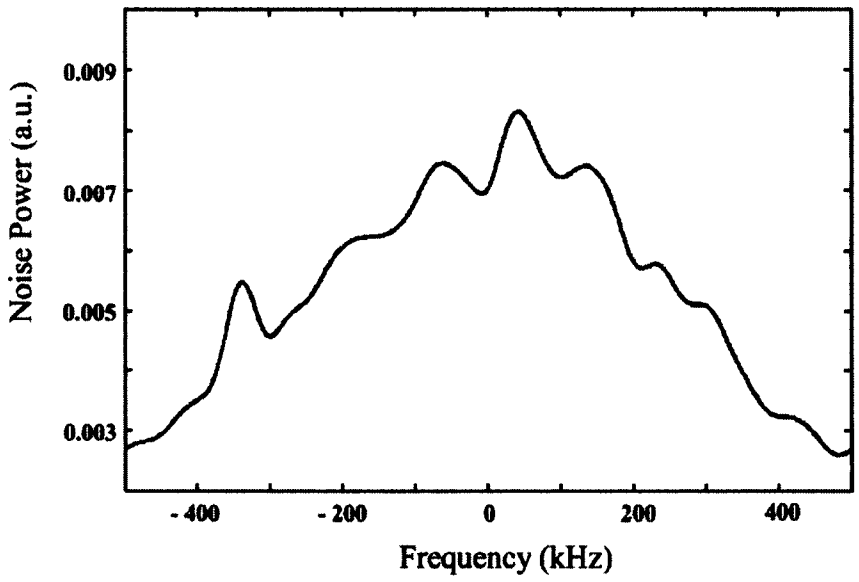

Figure 9.7. Noise power spectral density in the receiver channel of MARAN-DRX console. Higher energy concentration in the lower frequencies reduces the effectiveness of the VBF.

In addition, in real cases it is not possible to employ a VBF for the extremity points of k-space because the bandwidth is close to the sampling frequency and undesirable aliasing could take place because of the transition band in the non-ideal filter transfer function [9]. This reduces the number of VBF filter widths applied from 32, which is the number of points of one half of the k-space, to 28. In these extremity points conventional low-pass filtering was employed. The extremity k-space data points will contribute to fine profile structure, but will also reduce the

SNR gain by shifting left the ideal noise distribution line in the extremity of k-space (Fig. 9.6). Furthermore, the filter transition band will also increase the noise contribution in comparison to the ideal case (Fig. 9.6). This characteristic could be improved by increasing the filter order but it will also increase the filter dead time, which is not desirable for samples with fast T_2^* decay.

Figure 9.8 shows the actual k-space power spectral density measured using classical low-pass filter and VBF. Similar behavior to the model in Fig. 9.6 can be observed. Measurements of the area under both curves shows a reduction of 18% for VBF, which agrees with the reported gain in SNR.

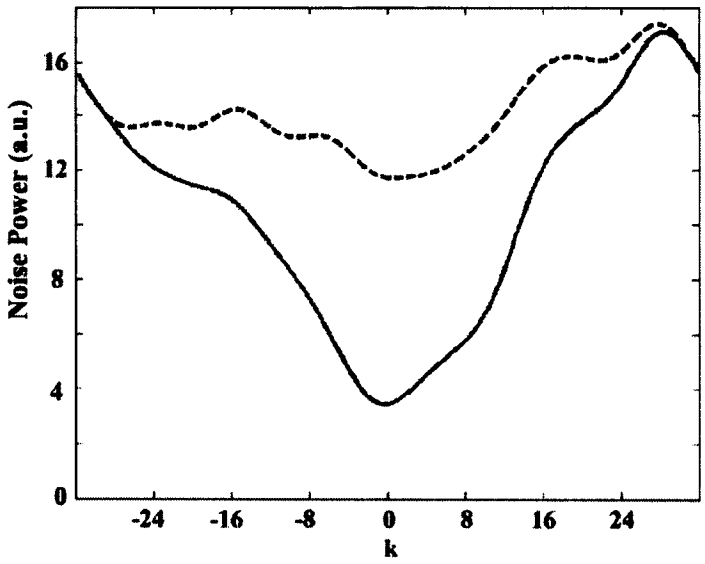

Figure 9.8. Bilateral k-space power spectral density measured using classical low-pass filter (--) and VBF(-). The area under the curve is 18% less for VBF.

The previous analysis can be applied also for 2D or 3D imaging. In SPRITE the maximum encoding bandwidth required increases with each added dimension.

Therefore, each dimension will contribute noise that can be removed with VBF, hence the gain in SNR should be equivalent to the 1D experiment for the same field of view in each dimension.

9.4 Conclusions

A new way to filter pure phase encode MRI data has been presented. By applying a variable bandwidth filter, the SNR for 1D images can be increased by about 20 % in comparison to a fixed bandwidth classical low-pass filter. This gain represents a reduction of up to 31 % in time of an experiment limited by signal averaging. The persistent sensitivity disadvantage of pure phase encode MRI compared to frequency encode methods means that even a 31 % improvement can be significant. Practical measurements also demonstrate conservation of the structural features and resolution in the VBF profile.

9.5 Experimental

The VBF was applied off-line for a 1D MRI image data set. An elastomeric sample of polyvinyl chloride, 2.2 cm in length, 2.2 cm width, with a T_2^* of 380 μs was the test sample during the data acquisition.

The Parks-McClellan algorithm [9] was applied to calculate the VBF coefficients with MATLAB. The filter has order 30 with linear phase response [9]. A sampling frequency of 1 MHz was employed for all the VBF filter widths to

maintain the same delay (15 μs) for all k-space points. The maximum absolute amplitude error [9] in the band-pass was 0.002 and 0.1 in the stop-band.

MRI data acquisition was performed on a MARAN-DRX 7 T MRI system (Oxford Instruments, UK) operating at a proton frequency of 299.65 MHz, with a 160 mm horizontal bore actively screened magnet. Magnetic field gradients of up to 40 G/cm were provided by a self-shielded gradient set SGRAD 156/100/S (Magnex Scientific, UK). A 6.2 cm diameter home built birdcage RF resonator was used for both radiofrequency transmission and reception. The RF pulse had a duration of 6.2 μs, corresponding to a flip angle of 10°. The 1000 W NMR plus RF power amplifier was provided by Communication Power (Brentwood, NY).

For comparison with VBF the MARAN-DRX console Ultrashape classical low-pass filter was employed. This digital filter has order 13 and a filter width of 500 kHz. Because the VBF has been applied offline, multiple points must be stored. Such data storage is clearly inefficient and ultimately undesirable.

The sample profile was obtained using the SPRITE sequence reproduced in Fig. 1 with an encoding time of 196 μs, a maximum gradient value of 11.6 G/cm and 64 k-space points. In each FID, 128 points with a dwell time of 1 μs were collected for post processing. To obtain the filtered profile, 28 VBF filter widths were applied on each half of k-space, resulting in 56 VBF filtered points over the whole k-space.

Acknowledgements

JCG thanks the Canadian International Development Agency (CIDA) for supporting part of this work. PMG wishes to acknowledge EPSRC of UK for support. BJB thanks NSERC of Canada and the Canada chairs program for a chair in MRI of materials (2007 - 2009). The UNB MRI Centre is supported by an NSERC Major Resources Support grant.

References

[1] S. Emid, J.H.N. Creyghton, High resolution NMR imaging in solids. Physica 128B (1985) 81-83.

[2] S. Gravina, D. G. Cory, Sensitivity and Resolution of Constant-Time Imaging, J. Magn. Reson. B 104 (1994), 53-61.

[3] B. J. Balcom, R. P. MacGregor, S.D. Beyea, D. P. Green, R. L. Armstrong, T. W. Bremner, Single-Point Ramped Imaging with T_1 Enhancement (SPRITE), J. Magn. Reson. A 123 (1996), 131–134.

[4] K. V. Romanenko, P.F. de J. Cano-Barrita, Bruce J. Balcom, ^{35}Cl profiling using centric scan SPRITE with variable flip angle excitation. J. Magn. Reson. 198 (2009) 24–30.

[5] B. J. Balcom, J. C. Barrita, C. Choi, S. D. Beyea, D. J.Goodyear, and T.W Bremner, Single-point magnetic resonance imaging (MRI) of cement based materials, Materials and Structures, 36 (2003), 166-182.

[6] L. Li, F. Marica, Q. Chen, B. MacMillan, B. J. Balcom, Quantitative Discrimination of Water and Hydrocarbons in Porous Media by Magnetization Prepared Centric-scan SPRITE, J. Magn. Reson. 186 (2007) 282-292.

[7] H. Hickey, B. MacMillan, B. Newling, M. Ramesh, P. V. Eijck, B. J Balcom, Magnetic resonance relaxation measurements to determine oil and water content in fried foods, Food Res. Int. 39 (2006), 612-618.

[8] J. G. Proakis, D. G. Manolakis. Digital signal processing. Prentice Hall, New Jersey, 2007, pp. 655-659.

[9] A.V. Oppenheim, R.W. Schafer, Discrete-Time Signal Processing, Prentice Hall, New Jersey, 1989, pp. 476-478.

[10] R. R. Ernst, Sensitivity enhancement in magnetic resonance. I. Analysis of the method of time averaging, Rev. Sci. Instr. 36 (1965), 1689–1695.

[11] Gustafsson, F, Determining the initial states in forward-backward filtering, IEEE Trans. Signal Process, 44 (1996), 988-992.

[12] H. W. Ott, Noise Reduction Techniques in Electronic Systems, John Wiley & Sons, USA, 1988, 228-243.

Vita

Candidate's full name: Juan Carlos García Naranjo

Pace of birth: Palma Soriano, Santiago de Cuba, Cuba

Date of birth: September 29, 1970

Universities attended:

Universidad Central "Marta Abreu" de Las Villas, Master of Science in Biomedical Engineering. 1999-2001.

Universidad de oriente, Bachelor of Science in Telecomunication engineering, 1988-1993.

Journal Publications:

1. G. LaPlante, J. C. García-Naranjo, B. J. Balcom, Real-time cure monitoring of an epoxy/polyamidoamine system with unilateral magnetic resonance, NDT&E International 44, 329 - 334, 2011.
2. J. C. García-Naranjo, I. V. Mastikhin, B. G. Colpitts , B. J. Balcom, A unilateral magnet with an extended constant magnetic field gradient. Journal of Magnetic Resonance 207, 337–344, 2010.
3. J. C. García-Naranjo, P. M. Glover, F. Marica, B. J. Balcom, Variable bandwidth filtering for magnetic resonance imaging with pure phase encoding, Journal of Magnetic Resonance, 202, 234–238, 2010.
4. P.F. de J. Cano-Barrita, A.E. Marble, B.J. Balcom, J.C. García, I.V. Masthikin, M.D.A. Thomas, T.W. Bremner, Embedded NMR sensors

to monitor evaporable water loss caused by hydration and drying in Portland cement mortar, Cement and Concrete Research 39, 324–328, 2009.

5. R .Blanco, D. Delisle, C. Díaz, J. C. García, N. López, A. Martínez Registrador de electromiogramas destinado a estudios de la marcha, Bioingeniería y Física Médica Cubana Vol. 9 N° 3, 25-28, 2008.

6. D. Delisle Rodríguez, R. Blanco Saad, N. López Río, J. C. García Naranjo, C. Díaz Novo, Módulo digital para electromiógrafo portátil, Universidad Ciencia y Tecnología Vol. 11, N° 45, 173-176, 2007.

7. J. Rosada, J.C. García, Receptor de señales definido por software utilizando dispositivos FPGA, Universidad Ciencia y Tecnología Vol. 10, N° 38, 81-84, 2006.

8. J. C. García Naranjo, Caracterización de un sistema de recepción de señales para tomógrafos Giroimag, Bioingeniería y Física Médica Cubana Vol. 4 N° 2, 11-18, 2003.

Conference papers:

1. J. C. García-Naranjo, I. V. Mastikhin, B. G. Colpitts , B. J. Balcom, A unilateral magnet with an extended constant magnetic field gradient. 10th Bologna Conference on Magnetic Resonance in Porous Media (MRPM 10). Germany, 2010

2. J. C. García-Naranjo, P. M. Glover, F. Marica, B. J. Balcom, Variable bandwidth filtering for magnetic resonance imaging with pure phase encoding. 10th International Conference on Magnetic Resonance Microscopy. ICMRM 10.USA, 2009.

3. J. C. García-Naranjo, I. V. Mastikhin, B. G. Colpitts , B. J. Balcom, Magnet Arrays for Unilateral Magnetic Resonance. 10th International Conference on Magnetic Resonance Microscopy. ICMRM 10.USA, 2009.

4. A. Pascau, O. Ferrer, A. Sóñora, J. C. García, Detección del sonido cardiaco fetal usando clusterización con el coeficiente de Pearson. Conferencia Internacional TELE'C 2006, Cuba, 2006.

5. A. Sóñora, J. C. García, A. Pascau, O. Ferrer, Implementación de un sistema portátil para el monitoreo fetal. Memorias. Conferencia Internacional TELE'C 2006, Cuba, 2006.

6. M. Cuadra, A. Corzo, A. Pascau, O. Ferrer, J. C. García, D. Hernández, Implementación de un sistema para el diagnóstico de afecciones vasculares. Su introducción en la práctica clínica. Memorias. Conferencia Internacional TELE'C 2000, Cuba, 2000.

7. A. Cruz, J. C. García, Caracterización de recintos apantallados para Tomógrafos de Resonancia Magnética. Memorias. Conferencia Internacional TELE'C 2000, Cuba, 2000.

8. M. Cuadra, A. Corzo, A. Pascau, O. Ferrer, J. C. García, D. Hernández, ANGIODIN PD 3000, Sistema microcontrolado para el diagnóstico de afecciones circulatorias periféricas. Memorias. Primer Congreso Latinoamericano de Ingeniería Biomédica, México, 1998.